Development of novel downshift phosphor for solar cells and elucidation of emission mechanism

(太陽電池用新規ダウンシフト蛍光体の創製および発光メカニズムの解明)

2023

Masato Iwaki

Doctoral Program in Advanced Materials Science and Technology

Graduate School of Science and Technology, Niigata University

8050 Ikarashi 2-nocho, Niigata 950-2181, Japan

Preface

The works of this doctoral thesis have been conducted under the supervision of Associate Professor Dr. Kenji Toda at Graduate School of Science and Technology, Niigata University, 8050 Ikarashi 2-nocho, Niigata 950-2181, Japan.

This dissertation focuses on the development of Eu^{2+}- or Ce^{3+}-activated downshift phosphors for crystalline silicon solar cells and the analysis of these emission mechanisms.

The author wishes that the finding and accomplishments of this work provide information for the further development of Eu^{2+}- or Ce^{3+}-activated phosphors.

Masato Iwaki

Masato Iwaki

Graduate School of Science and Technology, Niigata University
8050 Ikarashi 2-nocho, Niigata 950-2181, Japan

Feb, 2023

Contents

Chapter 1. General Introduction

Chapter 2. *Blue-Yellow Multicolor Phosphor,* Eu^{2+}*-activated* Li_3NaSiO_4*: Excellent Thermal Stability and Quenching Mechanism*

2-1 Introduction

2-2 Experimental section

2-3 Results and discussion

2-4 Conclusion

Chapter 3. *High Thermal Stable Blue-Emitting Alkali Silicate Phosphor,* Eu^{2+}*-activated* $Na_2Mg_2Si_6O_{15}$

3-1 Introduction

3-2 Experimental section

3-3 Results and discussion

3-4 Conclusion

Chapter 4. *Emission shift from green yellow to reddish orange in* Eu^{2+}*-activated* $Ca_6BaP_4O_{17}$ *by doping high amount of activator ion*

4-1 Introduction

4-2 Experimental section

4-3 Results and discussion

4-4 Conclusion

Chapter 5. *Determination of layer crystal structure* $Sr_2Ba_2(PO_4)_2O:Eu^{2+}$ *by Melt Quenching Technique*

5-1 Introduction

5-2 Experimental section

5-3 Results and discussion

5-4 Conclusion

Chapter 6. *Structure and Luminescence studies of* Ce^{3+}*-activated* $Ba_5La_3MgAl_3O_{15}$ *Green Emitting Phosphor*

6-1 Introduction

6-2 Experimental section

6-3 Results and discussion

6-4 Conclusion

Chapter 7. *Concluding remarks*

References

Acknowledgement

Chapter 1.

General Introduction

Phosphor materials have been widely used in lighting applications, especially phosphor converted white LEDs (pc-wLEDs).[1-10] The pc-WLEDs have many advantages in terms of lower energy consumption, mercury free, longer lifetime in comparison with traditional fluorescent lamps and incandescent bulbs. Before the development of pc-wLEDs, phosphors were primarily considered as another optical applications such as scintillators for X-ray and plasma displays for vacuum ultraviolet (VUV) or UV excitation.[11-26] However, since the pc-wLEDs consisted of yellow emitting $Y_3Al_5O_{12}:Ce^{3+}$ (YAG:Ce^{3+}) and blue emitting semiconductors (6H-SiC/GaN) was firstly reported by P. Schlotter *et al* in 1997, many phosphors for pc-WLEDs had been developed over the past two decades.[27]

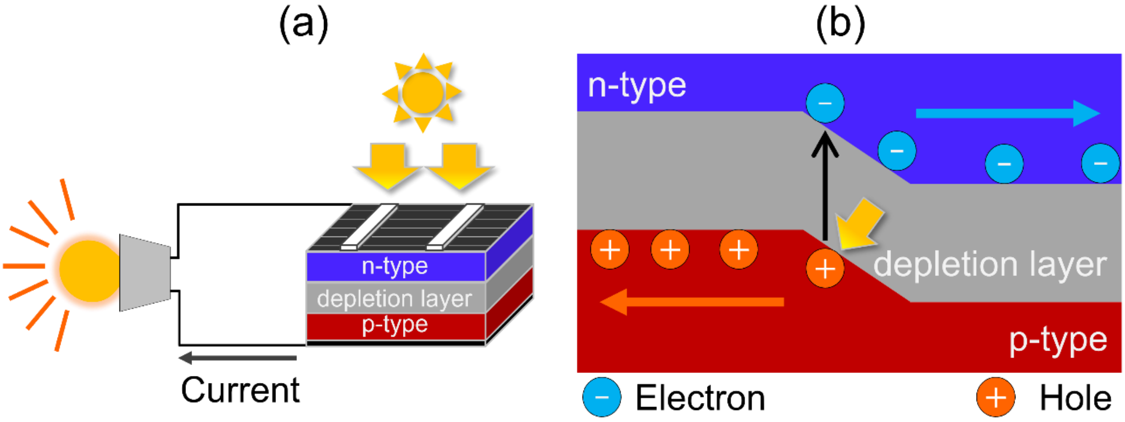

Fig. 1-1 Schematic diagrams of (a) c-Si solar cells and (b) p-n junction.

Recent years, phosphors have also been investigated as energy conversion materials in crystalline silicon (c-Si) solar cells.[28-34] The first c-Si solar cells were reported by Chapin *et al*. at Bell Telephone Laboratories in 1954.[35, 36] In solar cells generates the electric energy using photoelectric effect, which has been firstly found by Becquerel in 1839. The initial conversion efficiency reported by Chapin *et al*. was found to be 6%, however, modern c-Si solar cells have achieved a conversion efficiency of 26.7%.[37] The schematic diagram of the c-Si solar cell is shown in Fig. 1-1(a). The c-Si solar cell consists of two distinct layers, n- and p-types. In the depletion layer, which is formed by the p-n junction, neither electrons nor holes can move. The schematic diagram of the p-n junction is also illustrated in Fig. 1-1(b). Holes and electrons are formed when sunlight irradiates the c-Si solar cells. As increasing the amounts of electrons and holes, the slope is formed in the depletion layer because the charge equilibrium becomes imbalance. Moreover, the difference between Fermi levels in n and p-types dominates the electromotive force Since the solar energy has the largest potential among renewable energy such as geothermal, tide and water, alternative photovoltaic (PV) systems have been proposed such as tandem and perovskite types.[38-43]

Fig. 1-2 shows the sunlight spectrum (AM = 1.5) and the spectral response of c-Si. Sunlight spectrum has the maxim spectral irradiance around 550 nm, while the spectral response of c-Si has the peak top around 1000 nm. This spectral mismatch between the sunlight and spectral response of c-Si causes the lower actual conversion efficiency than the theoretical value (29%), which is also called the Shockley-Queisser limit.[44, 45]

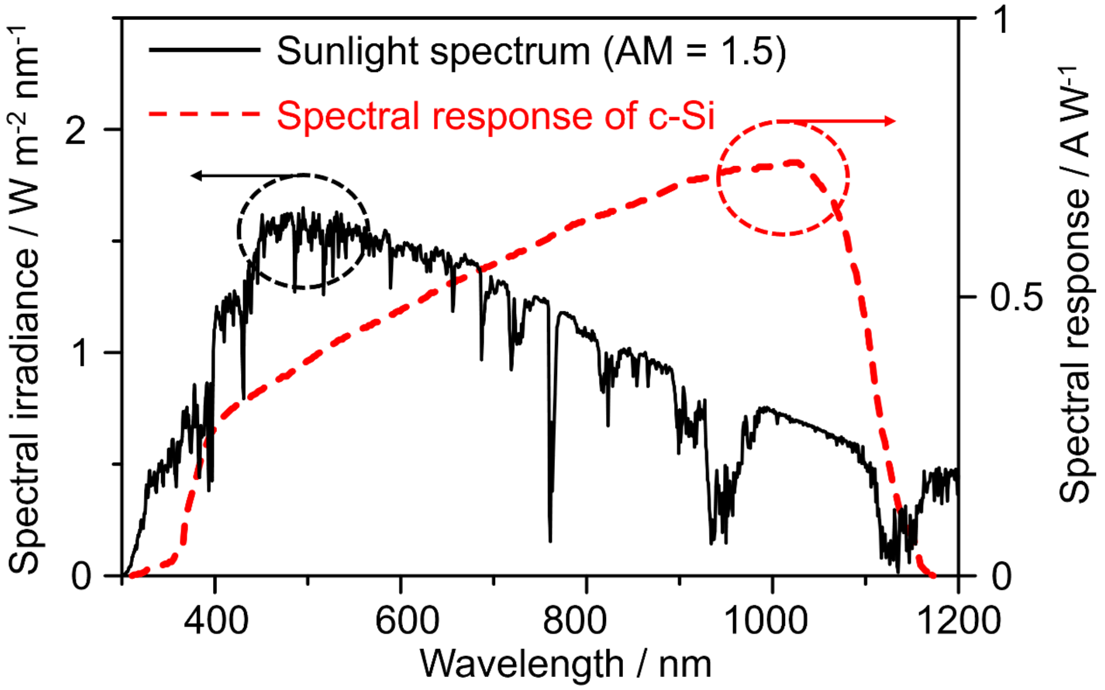

Fig. 1-2 Sunlight spectrum (AM = 1.5) (black solid line) and spectral response of c-Si (red dashed line).

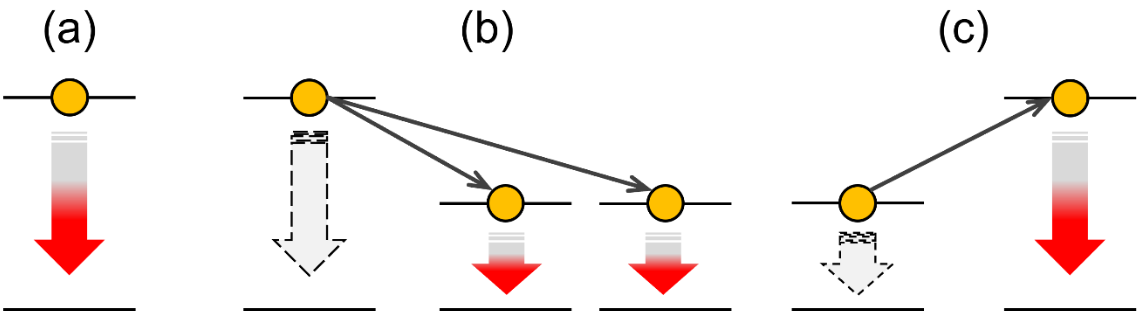

Fig. 1-3 Three different emission mechanism of phosphors: (a) downshift, (b) down-conversion and (c) up-conversion.

The improvement of conversion efficiency in current c-Si solar cells is expected to be achieved by phosphor materials. Phosphors can be classified into three different categories: (a) downshift, (b) down-conversion and (c) up-conversion, respectively (refer to Fig. 1-3).[46] In the case of downshift phosphors, a photon in the ground state is transferred to an excited state. After the relaxation process, the photon in the excited state returns to the ground state and an emission is observed. In contrast, the down-conversion involves the division of an excited photon into two photons. As a result, the quantum efficiency of the down conversion phosphors is possibly reached to 200%.[47] Up-conversion shows that the photon in the low excited level moves to the higher energy levels, resulting in visible emission under the infrared light excitation. Developed down - and up - conversion phosphors are summarized in Table 1-1(a) and (b). Down - and up - conversion phosphors commonly use Yb^{3+} ion, which is one of the rare earth elements. The Yb^{3+} ion not only shows the infrared emission around 1000 nm due to the 4f - 4f electron forbidden transition, but also acts as the energy donors in up - conversion phosphors. However, the quantum efficiency of current Yb^{3+}-activated down- and up-conversion phosphors are still low. Moreover, the optical properties of the Yb^{3+} ion are independent of the host material due to internal 4f -4f transitions, which limits the material design for spectral convertor in c-Si solar cells.

Table 1-1 Reported down-conversion phosphors.

Host	Donor	Acceptor	Ref.
Y_2O_3	Tb^{3+}	Yb^{3+}	48
$CaSc_2O_4$	Ce^{3+}	Yb^{3+}	49
$CaMoO_4$	Er^{3+}	Yb^{3+}	50
YOF	Pr^{3+}	Yb^{3+}	51
Lu_2O_3	Ho^{3+}	Yb^{3+}	52
$Y_3Al_5O_{12}$	Ce^{3+}	Yb^{3+}	47
Y_2O_3	Bi^{3+}	Yb^{3+}	53
$LuPO_4$	Tm^{3+}	Yb^{3+}	54
$Ca_9Y(PO_4)_7$	Eu^{2+}	Yb^{3+}	55
Ca_2MgWO_6	Cr^{3+}	Yb^{3+}	56

Table 1-2 Reported up-conversion phosphors.

Host	Donor	Acceptor	Ref.
β-$NaYF_4$	Yb^{3+}	Tb^{3+}	57
$La_2Mo_2O_9$	Yb^{3+}	Er^{3+}	33
$ZnTiO_3$	Yb^{3+}	Er^{3+}	58
$Ba_5Gd_8Zn_4O_{21}$	Yb^{3+}	Er^{3+}	59
$NaLuF_4$	Yb^{3+}	Ho^{3+}	60
$LiGa_5O_8$	Ni^{2+}	Tm^{3+}	61
$(Ba,Ca)_2ScAlO_5$	Yb^{3+}	Er^{3+}	62

From these viewpoints, the downshift phosphors are adopted as a spectral convertors for c-Si solar cells. Moreover, in this study, Eu^{2+} and Ce^{3+} ions are mainly used as activator ions to develop the downshift phosphor. The optical properties of these phosphors are dependent on the host material because the outer 5d orbitals are affected by ligands.[63] As a result, the quantum efficiencies of Eu2^{+-} or Ce^{3+}-activated phosphors are higher than those of phosphors doped the rare earth ion with 4f - 4f forbidden transition. Although these emission ions are often used as pc-WLEDs, the development of Eu^{2+}- or Ce^{3+}-activated downshift phosphors for c-Si solar cells may leads to the novel material design concept. Therefore, this study is aimed to develop novel Eu^{2+}- or Ce^{3+}-activated downshift phosphors for c-Si solar cells.

This thesis discusses the development of Eu^{2+}- or Ce^{3+}-activated downshift phosphor for c-Si solar cells and consists of the following six chapters.

In Chapter 2, the novel blue-yellow multicolor emitting phosphors, $Li_3NaSiO_4:Eu^{2+}$ (LNS:Eu^{2+}) are described. The emission mechanism of Eu^{2+} ion in LNS host is deeply discussed. Moreover, the thermal quenching behavior of LNS:Eu^{2+} is assisted by two different alkaline defects.

In Chapter 3, the blue-emitting $Na_2Mg_2Si_6O_{15}:Eu^{2+}$ with the high thermal stability are written. Eu^{2+} ions are located on two different alkaline sites and exhibit the excellent thermal stability compared with the reported Eu^{2+}-activated phosphors.

In Chapter 4, the emission color shift from yellow-green to reddish-orange of $Ca_6BaP_4O_{17}:Eu^{2+}$ is discussed. Moreover, the emission lifetime, thermal quenching behavior, the fabrication of prototype white LEDs is systematically conducted to validate its potential.

In Chapter 5, yellow-emitting $Sr_2Ba_2(PO_4)_2:Eu^{2+}$ synthesized by melt quenching method using an special furnace is described. This crystal structure and optical properties are deeply discussed.

In Chapter 6, near ultraviolet light excitable Ce^{3+}-activated green emitting

$Ba_5La_3MgAl_3O_{15}$ (BLMAO) are described. The crystal structure of BLMAO is isotype with $Ba_6La_2A_{l1.5}Fe_{2.5}O_{15}$ and the optical properties of Ce^{3+} ion in this crystal structure is discussed.

In Chapter 7, all results in this study and knowledges are totally summarized and discuss the potential of downshift phosphors for c-Si.

This dissertation has the contents following papers:

1. M. Iwaki, S. Kumagai, S. Konishi, A. Koizumi, T. Hasegawa, K. Uematsu, A. Itadani, K. Toda and M. Sato, *J. Alloy. Compd.*, 2019, **776**, 1016-1024.
2. M. Iwaki, K. Sugimoto, M. Watanabe, K. Uematsu, M. Sato and K. Toda, *J. Ceram. Process. Res.*, 2019, **20**, 205-210.
3. M. Iwaki, H. Takahashi, K. Uematsu, K. Toda and M. Sato, *J. Lumin.*, 2022, **246**.
4. M. Iwaki, K. Uematsu, M. Sato and K. Toda, *Inorg. Chem.*, 2023, **62**, 1250-1256.

In addition, the following are cited as related papers:

5. K. Toda, M. Iwaki, M. Katsu, S. Kamei, S. W. Kim, T. Hasegawa, M. Muto, R. Yamanasihi, T. Sakamoto, T. Ishigaki, K. Uemastu, M. Sato and D. H. Yoon, *J. Ceram. Process. Res.*, 2019, **20**, 276-279.
6. Y. Higuchi, M. Iwaki, A. Koizumi, R. Yamanashi, K. Uematsu, K. Toda and M. Sato, *Jpn. J. Appl. Phys.*, 2019, **58**, STFFD01.
7. T. Hasegawa, M. Iwaki, S. W. Kim, T. Ueda, K. Uematsu, K. Toda and M. Sato, *J. Alloy. Compd.*, 2019, **797**, 1181-1189.
8. T. Hasegawa, M. Iwaki, R. Tanaka, S.-W. Kim, S. Yin and K. Toda, *Inorg. Chem. Front.*, 2020, **7**, 4040-4051.
9. M. Sato, T. Ishigaki, M. Iwaki, K. Uematsu, M. Watanabe and K. Toda, *Inorg. Chem.*, 2021, **60**, 17810-17823.
10. M. Iwaki, R. Tanaka, K. Uematsu, M. Sato and K. Toda, *J. Lumin.*, 2023, **257**, 119714.

Chapter 2.

Blue-Yellow Multicolor Phosphor, Eu^{2+}-activated Li_3NaSiO_4: Excellent Thermal Stability and Quenching Mechanism

2-1 Introduction

In Chapter 2, we focus on phosphors in which Eu^{2+} is substituted for alkaline sites, and on the expected emergence of multi-color emissions through a site-engineering effect. A few studies on this topic have been reported, such as for $Na_3Sc_2(PO_4)_3$:Eu^{2+}, $NaScSi_2O_6$:Eu^{2+}, $NaMgPO_4$:Eu^{2+}, and $NaAlSiO_4$:Eu^{2+}.[64-69] With these phosphors, Eu^{2+} is substituted for a Na site to achieve a good performance in terms of the thermal stability and efficient fluorescent properties. Nevertheless, the emission mechanism in phosphors with Eu^{2+} substituted for the alkaline sites remains obscure. Furthermore, Wen *et al*. proposed that the emission wavelength of $(Sr,Ba)_2SiO_4$:Eu^{2+} is shifted when adding a Ba flux during the synthesis process. They concluded that Ba can be substituted for a Sr site, and thus, Eu^{2+} is likely to be replaced with another type of Sr site, which is responsible for a shift in the emission wavelength.[70]

From these two viewpoints, we focused on Li_3NaSiO_4 (LNS), as reported by Nowitzki *et al*., which has several types of alkali sites substitutable for Eu^{2+}.[71] $LiMAl_3N_4$ (M = Ca, Sr) and $MMgSi_3N_4$ (M = Ca, Sr) have the same crystal structure as that of LNS, indicating that LNS has the probability to be a good host lattice of Eu^{2+}-doped phosphors.[72-75] In this study, we prepared LNS:Eu^{2+} powder through a conventional solid-state reaction with and without a flux. Moreover, single LNS crystals were synthesized using a flux method. We conducted several types of measurements to elucidate the characteristics of the phosphors, measuring their photoluminescence properties, emission decay curves, thermal quenching properties, and thermoluminescence curves. These experimental consequences indicate that LNS:Eu^{2+} synthesized with a flux is capable of emitting multiple colors consisting of yellow and blue lights through Eu^{2+} doping only.

2-2 Experimental

Reagents. Li_2CO_3 (Kanto Chemical, Co., Inc., 99%), Na_2CO_3 (Kanto Chemical, Co., Inc., 99.8%), SiO_2 (Kanto Chemical, Co., Inc., 99%), and Eu_2O_3 (Shin-etsu Chemical Co., Inc., 99.99%) were used as raw materials for the cationic components of the phosphors. Sodium salts, such as Na_2CO_3, Li_2CO_3, NH_4Cl (Wako Co., Inc., 99.5%), and NaCl (High Purity Chemicals Co., Inc., 99.9%), were employed as fluxes.

Synthesis of powder sample. Herein, Eu^{2+}-doped LNS phosphor powders were synthesized using a conventional solid-state reaction method. The raw oxide and carbonate materials (Li_2CO_3, Na_2CO_3, SiO_2, and Eu_2O_3) were mixed at a ratio of Li:Na:Si:Eu = 3:1-2x:1:x (x = 0.005–0.04) using an agate mortar with acetone. After drying, the mixtures were pre-heated at 1,123 K for 6 h in air to remove CO_2 and H_2O and obtain white precursor powders. Na_2CO_3 was then added at 40 wt% as a flux to the precursor powder, followed by mixing in acetone until the powders dried. Next, these mixtures were heated at 1223 K for 6 h in a reducing atmosphere (95 vol.% Ar / 5 vol.% H_2) for reduction from Eu^{3+} to Eu^{2+}.

Characterization. Powder X-ray diffraction (XRD) patterns were obtained using an X-ray diffractometer (MX-Labo, Mac Science Co., Ltd.) with monochromatic CuKα radiation (λ= 1.54056 Å) under 25 mA and 40 kV. Rietveld refinement was carried out using RIETAN-FP software.[76] Photoluminescence (PL), photoluminescence excitation (PLE) spectra, and the quantum yield (QY) were measured at room temperature using a spectrofluorometer (FP-6500/FP-6600, Jasco, Inc.) with a 150 W Xenon lamp. The decay curves of Eu^{2+} in the LNS were measured using a Quantaurus-Tau (Hamamatsu Photonics, Inc.). The chromaticity diagram was analyzed using a PMA-12 multi-channel spectroscope (Hamamatsu Photonics, Inc.). The thermoluminescence (TL) curves were measured at a heating rate of 1 K/s using the same apparatus used for the chromaticity diagram. The heating apparatus was made in our laboratory. The reflection and absorption spectra of the samples were evaluated using a diffuse-reflectance spectrum (DRS) (V-50, Jasco Co.) based on $BaSO_4$ white powder as a reference.

2-3 Results and Discussion

2-3-1 Rietveld refinement

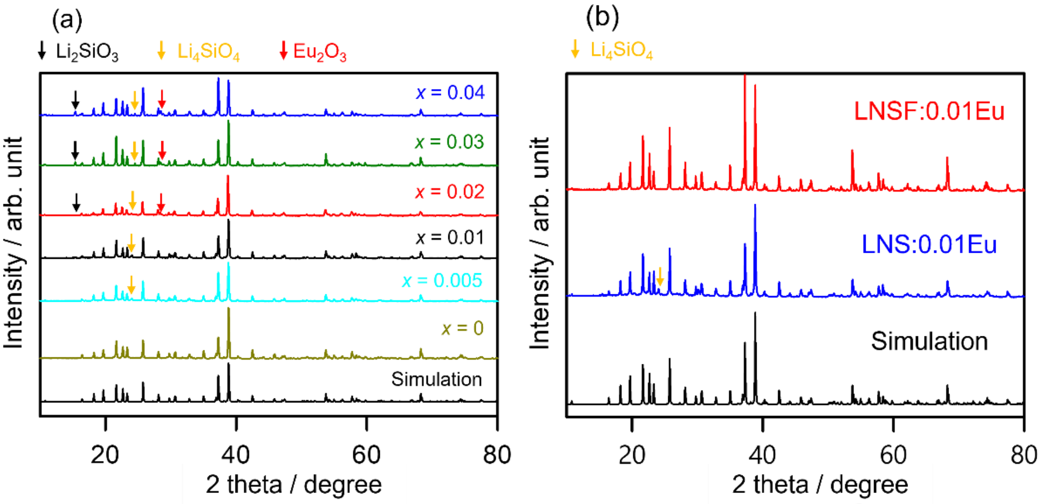

Fig. 2-1(a) XRD patterns of $Li_3Na_{1-2x}Eu_xSiO_4$ (x = 0, 0.005, 0.01, 0.02, 0.03, 0.04) and (b) $Li_3Na_{0.98}Eu_{0.01}SiO_4$ (x = 0.01) with and without Na_2CO_3 flux.

XRD patterns of $Li_3Na_{1-2x}Eu_xSiO_4$ (x = 0, 0.005, 0.01, 0.02, 0.03, 0.04) are shown in Fig. 2-1(a). Although a few impurity phases, including Li_4SiO_4, appear at beyond x = 0.02, LNS predominantly remained the main phase in all our samples. Li_4SiO_4 may be produced due to the volatilization of the Na component during the pre-heating or calcination process. In addition, the Eu_2O_3 peak at approximately 2 theta = 30° becomes much clearer at above x = 0.03, implying that solubility limits of Eu^{2+} in LNS exist between x = 0.01 and x = 0.02. The XRD patterns of LNS:0.01Eu^{2+} synthesized with and without Na_2CO_3 flux are shown in Fig. 2-1(b). a diffraction peak of Li_4SiO_4 was slightly observed as an impurity in the sample without flux. Nevertheless, LNS:0.01Eu^{2+} with a Na_2CO_3 flux (LNSF:0.01Eu^{2+}, where ‘F’ indicates the flux) is obtained as a single phase because the Na_2CO_3 flux promotes a chemical reaction.

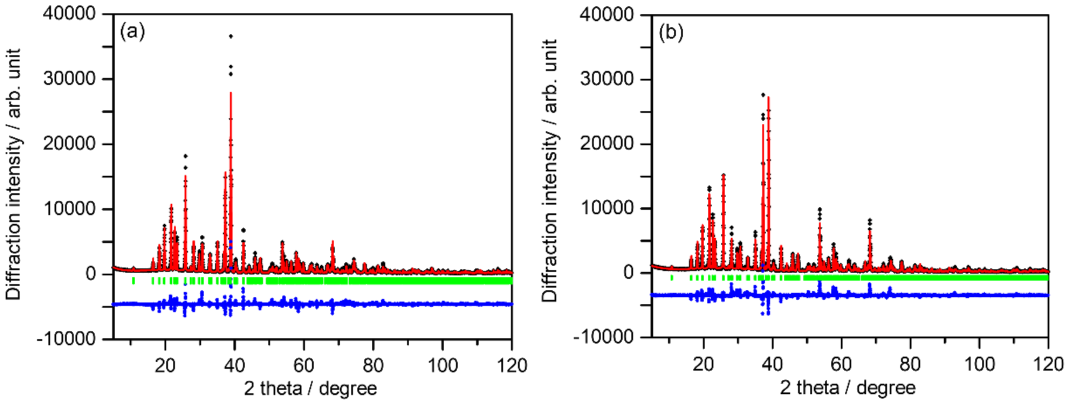

Fig. 2-2 Observed (black + symbol), calculated (red solid line) and difference (blue solid line) patterns obtained from Rietveld refinement on X-ray powder diffraction data of (a) LNS:$0.01Eu^{2+}$ and (b) LNSF:$0.01Eu^{2+}$.

Table 2-1 Parameters refined through Rietveld analysis for each LNS powder.

	LNS:$0.01Eu^{2+}$	LNSF:$0.01Eu^{2+}$
System	Tetragonal	
S.G.	$I4_1/a$ (#88)	
a (Å)	10.7869 (2)	10.7878 (3)
c (Å)	12.6387 (3)	12.6361 (4)
V (Å^3)	1470.60 (5)	1470.55 (8)
Z	16	16
R_{wp} (%)	13.579	12.846
R_p (%)	10.131	9.882
R_e (%)	3.680	3.583
S	3.690	3.585

Fig. 2-2 shows the fitting patterns obtained from the Rietveld refinements for the LNS, namely, LNS:$0.01Eu^{2+}$ and LNSF:$0.01Eu^{2+}$ in (a) and (b), respectively. The refined crystallographic parameters from the Rietveld refinements are summarized in Tables 2-1 for LNS:0.01Eu^{2+} and LNSF:0.01Eu^{2+}. In the Rietveld analysis, the isotropic thermal atomic displacement parameters, B_{eq}, for certain ions such as at the Eu1, O2, O3, O4, Li1, and Li2 sites were constrained to having the same value because the B_{eq} values in these sites were not refined as positive values. This may be attributed to an insufficient correction in the preferable orientation because a preferable crystalline growth is promoted through a flux, and the raw materials of Na_2CO_3 and Li_2CO_3 behave as a self-flux. As a result, the R_{wp} factors for all samples obtained from the Rietveld refinement were slightly greater than 10%.

2-3-2 Crystal Structure

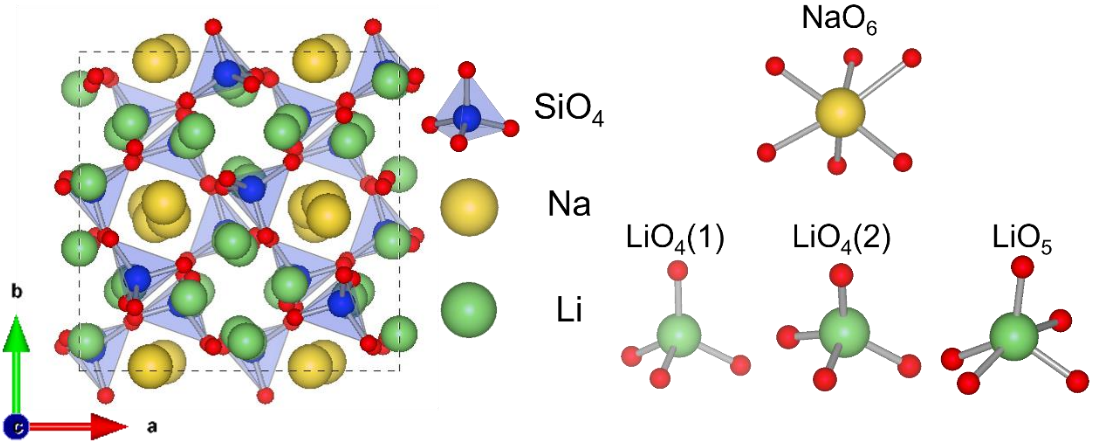

Fig. 2-3 Crystal structure of LNS and four different crystallographic alkali sites illustrated by the VESTA program.

The LNS crystal structure illustrated by the VESTA program is shown in Fig. 2-3.[77] The lattice parameters were a = 10.782(3) Å, c = 12. 6342(17) Å, and V = 1468.7(6) Å^3 for a tetragonal system with a space group $I4_1/a$ (No.88). This structure contains one NaO_6 trigonal prism, two LiO_4 tetrahedra, one LiO_5 pyramid, and one SiO_4 tetrahedron, as also shown in Fig. 2-3. Here, Eu^{2+} tends to substitute for Na sites because the ionic radius of Na^+ (1. 02 Å, with a 6-fold coordination) is similar to that of Eu^{2+} (1.17 Å, with a 6-fold coordination).[78] It seems to be difficult for Eu^{2+} to replace the Li^+ sites because the size of the Li^+ (0.59 Å, with 4-fold coordination) is smaller than that of Na^+ (0.99 Å, with 4-fold coordination).[78] The ionic radius of Li^+ for 5-fold coordination has yet to be reported, whereas the ionic radius of Li^+ for 6-fold coordination was reported to be 0.79 Å, and thus, the 5-fold coordination value may be estimated to be between 0.59 and 0.79 Å.

2-3-3 PL and PLE

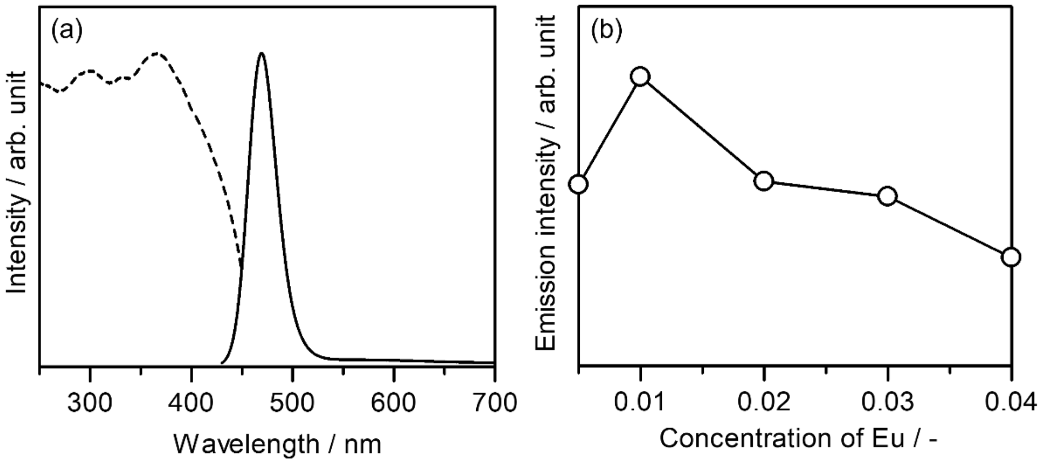

Fig. 2-4(a) PL and PLE spectra of LNS:0.01Eu^{2+} and (b) the dependence of the emission peak intensities on the Eu^{2+} concentration in the LNS:xEu^{2+} phosphors.

PL and PLE spectra of LNS:0.01Eu^{2+} are shown in Fig. 2-4(a). LNS:0.01Eu^{2+} shows a broad emission at approximately 470 nm, and an excitation peak at approximately 360 nm. Eu^{2+}-doped LNS can emit a blue emission under a NUV light. In the previous section, the impurity phase Li_4SiO_4 appeared in LNS:xEu^{2+} (x = 0.005–0.004). However, Eu^{3+} ions are unable to reduce Eu^{2+} in Li_4SiO_4 synthesized in a reduction atmosphere. Hence, the influence of the impurity phase Li_4SiO_4 can be ignored. The concentration dependence of the excitation and emission intensities is illustrated in in Fig. 2-4(b). LNS:0.01Eu^{2+} was found to have the highest emission intensity among all of the samples, and is likely an optimal dopant concentration. However, even when all Eu^{2+} ions are doped, they cannot replace the Na sites completely, as can be seen in Fig. 2-1, where the impurity phase coming from the Eu component occurs at beyond x = 0.02.

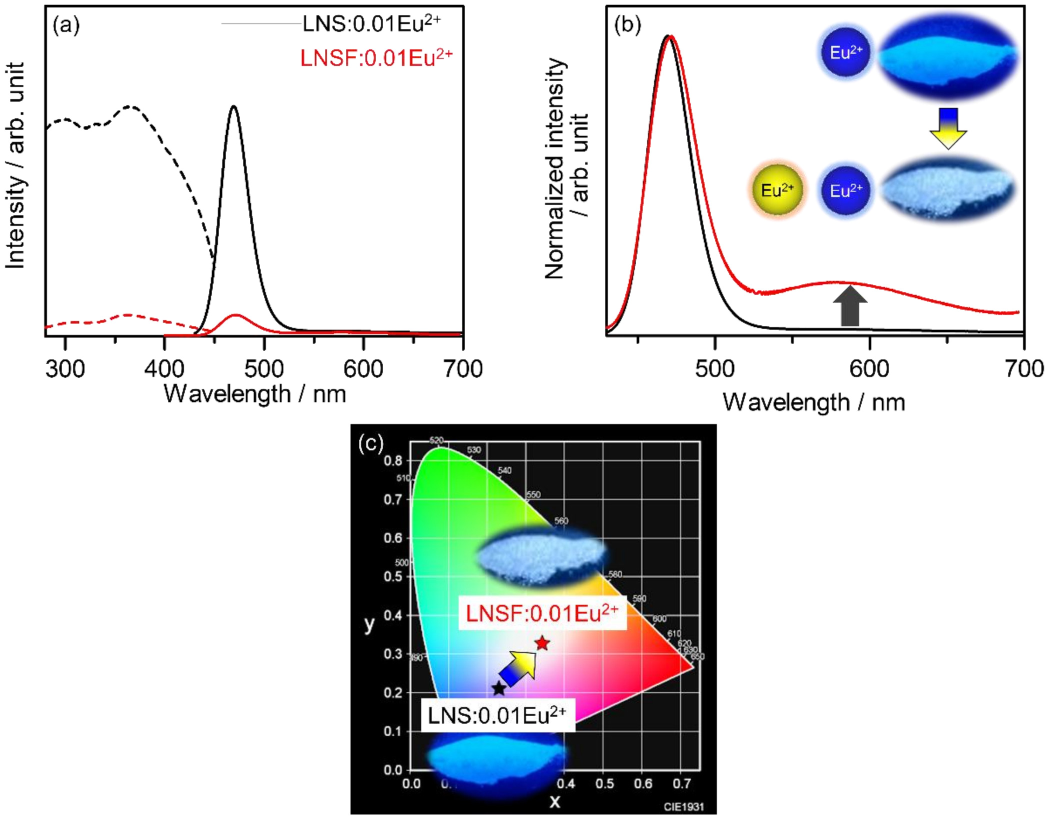

Fig. 2-5(a) Emission and excitation spectra of LNS:0.01Eu^{2+} and LNSF:0.01Eu^{2+}, (b) normalized emission spectra of LNS:0.01Eu^{2+} and LNSF:0.01Eu^{2+} (the photographs show the emission of each phosphor under black light (λ_{ex} = 365 nm)) and (c) Chromaticity diagram of blue-emitting LNS: 0.01Eu^{2+} (black) and white-emitting LNSF: 0.01Eu^{2+} (red).

In contrast, in the PL and PLE spectra of LNSF:0.01Eu^{2+} and LNS:0.01Eu^{2+}, as shown in Fig. 2-5(a), the emission and excitation intensities of LNSF:0.01Eu^{2+} become weaker than those of LNS:0.01Eu^{2+}, which indicates that Eu^{2+} is emitted from the LNS host lattice through the addition of Na_2CO_3 as a flux, as well as by the increase in the Na component in the starting material, leading to a small amount of effective Eu^{2+} doping in LNSF:$0.01Eu^{2+}$. However, the luminescent colors are remarkably different from each other, as can be seen in the emission photographs of LNS:$0.01Eu^{2+}$ and LNSF:$0.01Eu^{2+}$ under NUV light (λ_{ex} = 365 nm) shown the photographs in Fig. 2-5(b). The normalized emission spectra of the two phosphors are shown in Fig. 2-5(b), and a chromaticity diagram is illustrated in Fig. 2-5(c). The LNSF:$0.01Eu^{2+}$ phosphor has two emission peaks at approximately 470 and 580 nm, whereas LNS:$0.01Eu^{2+}$ has only one emission peak at around 470 nm. This indicates that Eu^{2+} in LNSF:$0.01Eu^{2+}$ certainly substitutes some other sites that can contribute to the long-wavelength emission assisted by the Na_2CO_3 flux. Furthermore, the chromaticity diagram in Fig. 2-5(c) shows that the emission wavelength of LNS:$0.01Eu^{2+}$ is located within the blue wavelength region, whereas the emission region of LNSF:$0.01Eu^{2+}$ is positioned within the white emission region. The (X,Y) coordination in the chromaticity diagram is summarized on Table 2-2. This means that the emission color of the phosphor can be controlled through the addition of the Na_2CO_3 flux.

Table 2-2 (X,Y) coordination of LNS:$0.01Eu^{2+}$ and LNSF$0.01Eu^{2+}$.

	X	Y
LNS:$0.01Eu^{2+}$	0.2300	0.2110
LNSF:$0.01Eu^{2+}$	0.3420	0.3280

The substitution of Eu^{2+} into the alkaline sites is carried out between different charges. It is well known that Eu^{2+}-activated phosphor materials substituted in alkaline sites generate a single alkaline vacancy, thereby maintaining the charge balance.[65] Therefore, the charge balance is neutral in Eu^{2+}-activated Li_3NaSiO_4. It should be emphasized that the present phosphor makes it possible to emit a multi-color light through Eu^{2+} doping only. The quantum yields for the two phosphors are listed in Table 2-3. At present, we have not optimized the synthesis method yet, and therefore, the quantum yields can be further improved.

Table 2-3 Quantum efficiency for each phosphor.

Phosphors	Absorption rate [%]	External quantum efficiency [%]	Internal quantum efficiency [%]
LNS: $0.01Eu^{2+}$	78.20	40.97	52.39
LNSF: $0.01Eu^{2+}$	39.18	6.79	17.33

The blue-emission intensity of LNSF:$0.01Eu^{2+}$ is smaller in comparison with that of LNS:$0.01Eu^{2+}$, whereas the yellow-emitting intensity at approximately 580 nm increases in comparison with that of LNS:$0.01Eu^{2+}$. As a result, LNSF:$0.01Eu^{2+}$ has two emission regions, blue and yellow, which are complementary to white, leading to a white emission, as shown in Fig. 2-5(a). The fact that a white color emission is realized in LNSF:$0.01Eu^{2+}$ indicates that Eu^{2+} occupies not only the Na site (a single unique type of crystallographically) but also other sites. The LNS contains five cation sites, namely, one Na site, three Li sites, and one Si site. According to Henderson *et al.*, the crystal field strength of a cation site, Dq, can be expressed based on the average bond length for the surrounding sites, R, as in equation (1) below:[79]

$$Dq \propto \frac{1}{R^5} \quad (1)$$

This relation means that smaller-sized emission sites increase the crystal field strength, leading to a longer emission wavelength. Based on the equation above, a yellow emission should originate from a site smaller than the Na^+ site. Zuckerman proposed that the split strengths of the d orbital energy levels in a square pyramidal site are usually lower than those of tetrahedral and octahedral sites.[80] In addition, Blasse *et al*. supposed that the d orbital energy levels in a trigonal prism site are higher than those of an octahedral site.[81] Considering these issues, the LiO_5 site is quite reasonable as a substitution site of Eu^{2+}. Moreover, we calculated the value of the bond valence sum (BVS) so as to presume the valence of the substitutional sites for Eu^{2+}, NaO_6, and LiO_5, respectively. The BVS values for each site in LNS:0.01Eu^{2+} and LNSF:0.01Eu^{2+} are shown in Table 2-4. In white-emitting LNSF:0.01Eu^{2+}, the BVS values in NaO_6 in LNSF:0.01Eu^{2+} decrease. Nevertheless, the BVS value in LiO_5 is larger than that in LNS:0.01Eu^{2+}. This indicates that the Na_2CO_3 flux assists the substitution of Eu^{2+} into the LiO_5 sites.

Table 2-4 Bond valence sum values for NaO_6 and LiO_5 sites in LNS:0.01Eu^{2+} and LNSF:0.01Eu^{2+}

Phosphors	NaO_6	LiO_5
LNS:0.01Eu^{2+}	0.8646	1.0034
LNSF:0.01Eu^{2+}	0.8237	1.0958

2-3-4 Fluorescence lifetime

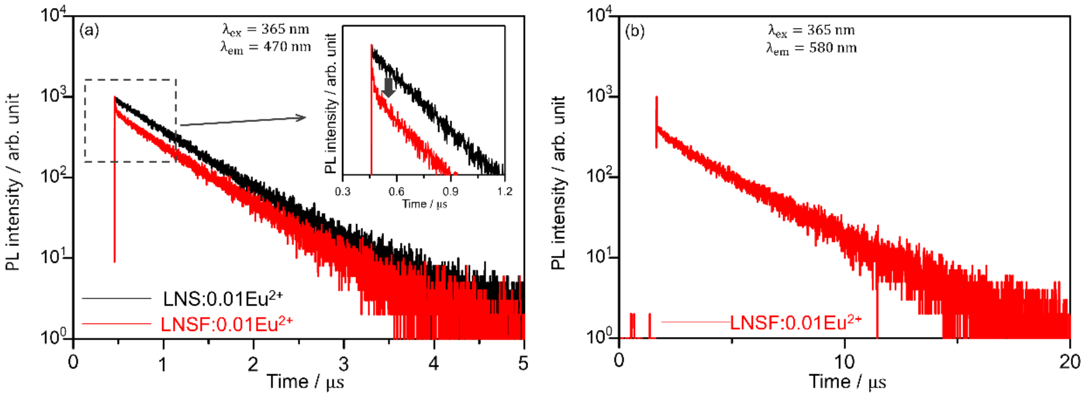

Fig. 2-6(a) Photoluminescence decay curves of LNS:0.01Eu^{2+} and LNSF:0.01Eu^{2+} (monitored at 470 nm and excited at 365 nm). The inset shows the increasing behavior of the decay curves. (b) Photoluminescence decay curves of LNSF:0.01Eu^{2+} (excited at 365 nm and monitored at 580 nm).

The decay curves of an emission at 470 nm for LNS:0.01Eu^{2+} and LNSF:0.01Eu^{2+} are shown in Fig. 2-6(a), and enlarged views of the decay curves for the phosphors are illustrated in Fig. 2-6(b). A single exponential curve is observed in LNS:0.01Eu^{2+}, whereas LNSF:0.01Eu^{2+} seems to include a multiple exponential curve, implying the occurrence of an energy transfer. This also implies that the Eu^{2+} ions in LNS:0.01Eu^{2+} replace only the NaO$_6$ site, whereas those in LNSF:0.01Eu^{2+} substitute the NaO$_6$ site and one of the LiO$_5$ sites. In the case of LNS:0.01Eu^{2+}, the lifetime τ is estimated through equation (2):[82]

$$\tau = \frac{\int_0^\infty tI(t)t}{\int_0^\infty I(t)dt} \quad (2)$$

where τ is the average lifetime. From equation (2), the lifetime is found to be 0.647 μs for LNS:0.01Eu^{2+} and 0.619 μs for LNSF:0.01Eu^{2+}. The average lifetime of LNS:0.01Eu^{2+} is slightly longer than that of LNSF:0.01Eu^{2+}, which indicates that the Eu^{2+}-Eu^{2+} distance in LNSF:0.01Eu^{2+} is shorter than that in LNS: 0.01Eu^{2+}; this difference is likely from the Na_2CO_3 flux, which not only promotes a chemical reaction but also assists Eu^{2+} in substituting the LiO_5 site. As a result, the blue emission lifetime of LNSF:0.01Eu^{2+} decreases owing to the energy transfer among the Eu^{2+} emission centers. Furthermore, the difference in lifetime between LNS:0.01Eu^{2+} and LNSF:0.01Eu^{2+} indicates that, in the case of LNSF:0.01Eu^{2+}, the energy of Eu^{2+} substituting the NaO_6 site is transferred to Eu^{2+} substituting the LiO_5 site. Xu *et al*. suggested that the lifetime of an acceptor is increased through the energy transfer from the donors. [83, 84] To confirm this, we measured the decay curves of the emission at 580 nm for LNSF:0.01Eu^{2+} (Fig. 2-6(b)). However, the decay curve for LNS:0.01Eu^{2+} could not be measured because the yellow emission of this sample is too weak to be detected, which is reasonable based on the fact that the decay curve of LNS:0.01Eu^{2+} is composed of a single exponential curve. In contrast, the lifetime of LNSF:0.01Eu^{2+} within the region of a yellow emission was found to be 2.80 μs through equation (2). This calculated lifetime is much longer than that of the blue emission. This result indicates that Eu^{2+} replacing LiO_5 acts as an acceptor ion and can receive energy from the donor Eu^{2+} ions substituting for the NaO_6 site. As previously mentioned, the two Eu^{2+} environments, namely, the sites substituting for the NaO_6 and LiO_5 sites, are completely different.

2-3-5 Thermal properties of photoluminescence

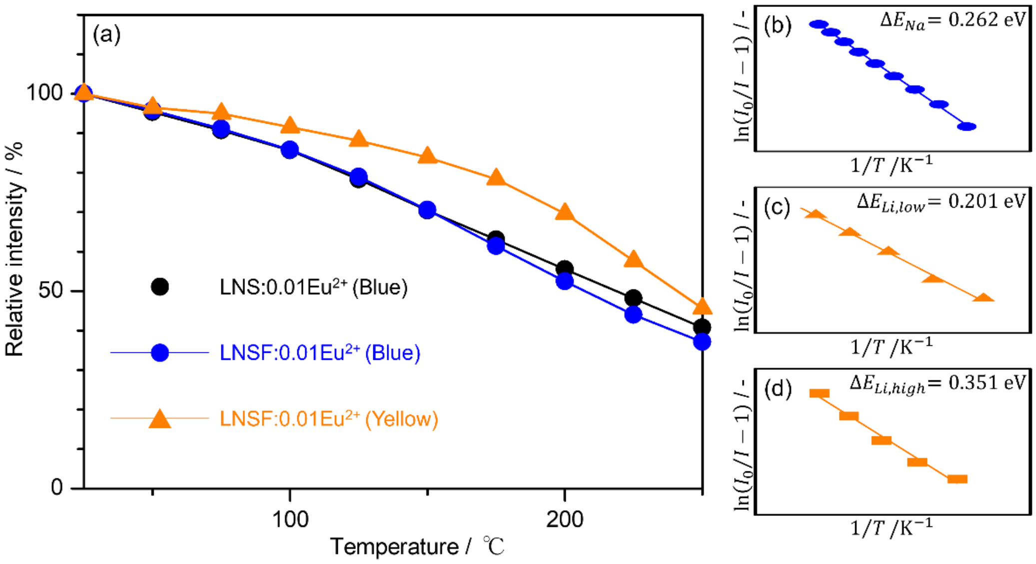

Fig. 2-7 (a) Temperature dependence of relative intensities for LNS: $0.01Eu^{2+}$ and LNSF: $0.01Eu^{2+}$ and linear fitting of the relationship of ln[(I_0/I_T)-1] vs. 1/ T for (b) blue and (c) yellow emissions at low temperature, and (d) yellow emission at high temperature (all data were obtained from LNSF:$0.01Eu^{2+}$).

The temperature dependence of the emission intensities for LNS:$0.01Eu^{2+}$ is shown in Fig. 2-7. As the temperature increases from room temperature, the emission intensities decrease. At 423 K, the emission intensity of the phosphor decreases to 70.9% of that at room temperature. Compared with other Eu^{2+}-activated silicate phosphors (*e.g.*, Ca_2SiO_4:Eu^{2+} or Sr_2SiO_4:Eu^{2+}), it can be noted that LNS:$0.01Eu^{2+}$ has good thermal stability.[85-89] The thermal stability data used to elucidate the activation energy for thermal quenching for LNSF:$0.01Eu^{2+}$ are illustrated in Fig. 2-7(a). The slope for the yellow emission intensity is gentler than that of the blue emission intensity. The yellow emission intensity is maintained at

83.9% even at 423 K. Based on these data, the activation energy ($\varDelta E$) is calculated through equation (3):[90, 91]

$$\ln\left(\frac{I_0}{I_T}-1\right)=\ln c-\frac{\varDelta E}{kT} \qquad (3)$$

where I_0 is the emission intensity at room temperature, I_T is the emission intensity at temperature T, $\varDelta E$ is the activation energy of thermal quenching, and k is the Boltzmann constant (= 8.62×10^{-5} eV). The plots of ln [(I_0/I_T)-1] versus 1 / (kT) for LNS:0.01Eu^{2+} and LNSF:0.01Eu^{2+} are illustrated in Fig. 2-7(b)-(d). The value of $\varDelta E_{\mathrm{Na}}$ corresponding to the activation energy for the Na site is 0.262 eV. In contrast, an interesting behavior was observed in LNSF:0.01Eu^{2+}, in which the $\varDelta E_{\mathrm{Na}}$ value in the blue emission is almost equal to that of LNS:0.01Eu^{2+}. However, the temperature dependence for the yellow emission could not be fitted by equation (3) using a single exponential component. Thus, we tried to fit the data using two components. As the results indicate, the activation energy $\varDelta E_{\mathrm{Li}}$ is 0.201 eV for the low-temperature region and 0.351 eV for the high-temperature region. The Eu^{2+} emission centers substituting for the Li site can maintain a high-emission intensity even at high temperatures, as compared with the case of the Eu^{2+} emission centers substituting for the Na site.

2-3-6 Thermoluminescence (TL)

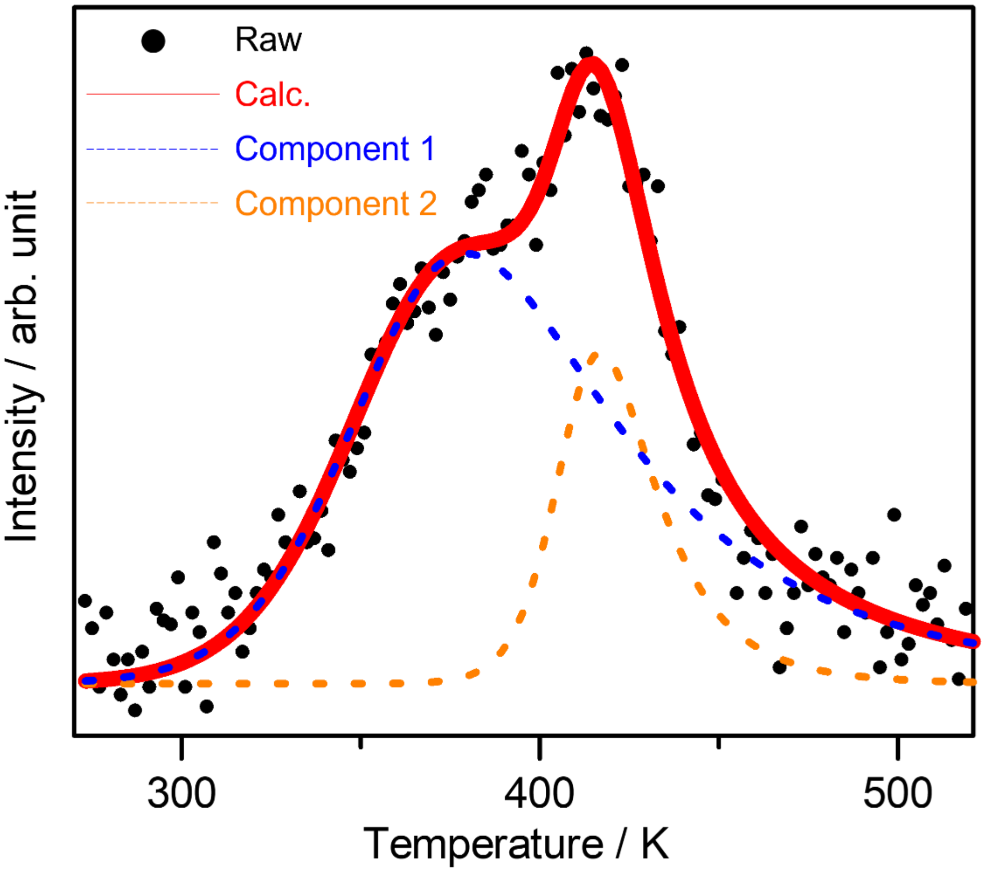

Fig. 2-8 Fitting of TL curves (red, measured data; black solid line, simulation data; blue dashed line, first component; green dashed line, second component) monitored at λ_{em} = 470 nm

Fig. 2-8 shows the TL curves for LNSF:0.01Eu^{2+} at λ_{em} = 470 nm excited at 254 nm. LNS:0.01Eu^{2+} did not show a curve although the emission intensity of LNS:0.01Eu^{2+} is higher than that of LNSF:0.01Eu^{2+} at room temperature. This fact indicates that LNS:0.01Eu^{2+} does not have traps contributing to the high-temperature emission. TL behavior is consistently observed for LNSF:0.01Eu^{2+}

at around 400 K within the blue and yellow wavelength regions. The trap depth was estimated from the curve fitting using equation (3):[92-94]

$$I(T) = I_m b^{\frac{b}{b-1}} \exp\left\{\frac{E}{kT} \times \frac{T-T_m}{T_m}\right\} \times \left[(b-1)\varDelta^2 \varDelta_m^{-2}(1-\varDelta) exp\left\{\frac{E}{kT} \times \frac{T-T_m}{T_m}\right\} + Z_m\right]^{-\frac{b}{b-1}}$$

(3)

$$\varDelta = \frac{2kT}{E},\ \varDelta_m = \frac{2kT_m}{E}, Z_m = 1 + (b-1)\varDelta_m$$

where I_m is the maximum emission intensity, T_m is the temperature at the maximum intensity, b is the kinetics order parameter, E is the trap depth, and m is the number of TL peaks. Based on equation (3), the shallow trap depth (E_1) is found to be 0.54 eV, and the deep trap depth ((E_2) is 1.95 eV. It is reasonable to consider that the two traps originate from the difference in charge between Eu^{2+} and Li^+ or Na^+. The defects responsible for TL can be explained using the Kröger-Vink equation, as in equations (4) and (5):

$$\mathrm{Eu} \rightarrow \mathrm{Eu}_{\mathrm{Na}}^{\cdot} + V_{\mathrm{Na}}' \quad (4)$$

$$\mathrm{Eu} \rightarrow \mathrm{Eu}_{\mathrm{Li}}^{\cdot} + V_{\mathrm{Li}}' \quad (5)$$

where V_{Na}' and V_{Li}' are formed when Eu^{2+} is substituted for the NaO_6 and LiO_5 sites, respectively. Sahu *et al.* suggested that a Li^+ vacancy makes the trap deeper in comparison with a Na^+ vacancy, and that the activation energies required to release trapped electrons, namely, shallow trap E_1 and deep trap E_2, correspond to the energy levels of V_{Na}' and V_{Li}', respectively.[95, 96] Furthermore, Wang *et al*. proposed that, in $Na_3Sc_2(PO_4)_3$:Eu^{2+}, the V_{Na}' defects produced by Eu^{2+} substituting for Na sites trap the electrons, followed by their release to the 5d emitting levels of Eu^{2+}. Consequently, the emission intensity of NSP:Eu^{2+} increases as the temperature rises.[65] The same situation may be applicable to the present phosphor, that is, V_{Na}' and V_{Li}' in LNSF:0.01Eu^{2+} are capable of enhancing the emission intensity at high temperatures for a yellow emission. Based on these considerations, a possible thermal quenching mechanism for LNSF:0.01Eu^{2+} is proposed, as shown in Fig. 2-9. The band gap for the LNS host is 5.33 eV, as estimated from the DRS spectra. First, electrons are excited under 360 nm NUV light and move to the conduction band. Second, the electrons are trapped in shallow or deep traps. As the temperature increases, the traps release electrons, followed by their recapture by the 5d emitting levels of Eu^{2+} at both Li^+ and Na^+ sites. Then, Eu^{2+} emits two emission wavelengths. At this stage, some of the electrons in the conduction band are trapped at two types of defects. These electrons are released at high temperatures, contributing to the Eu^{2+} emission, providing thermal stability of the yellow emission to the phosphor.

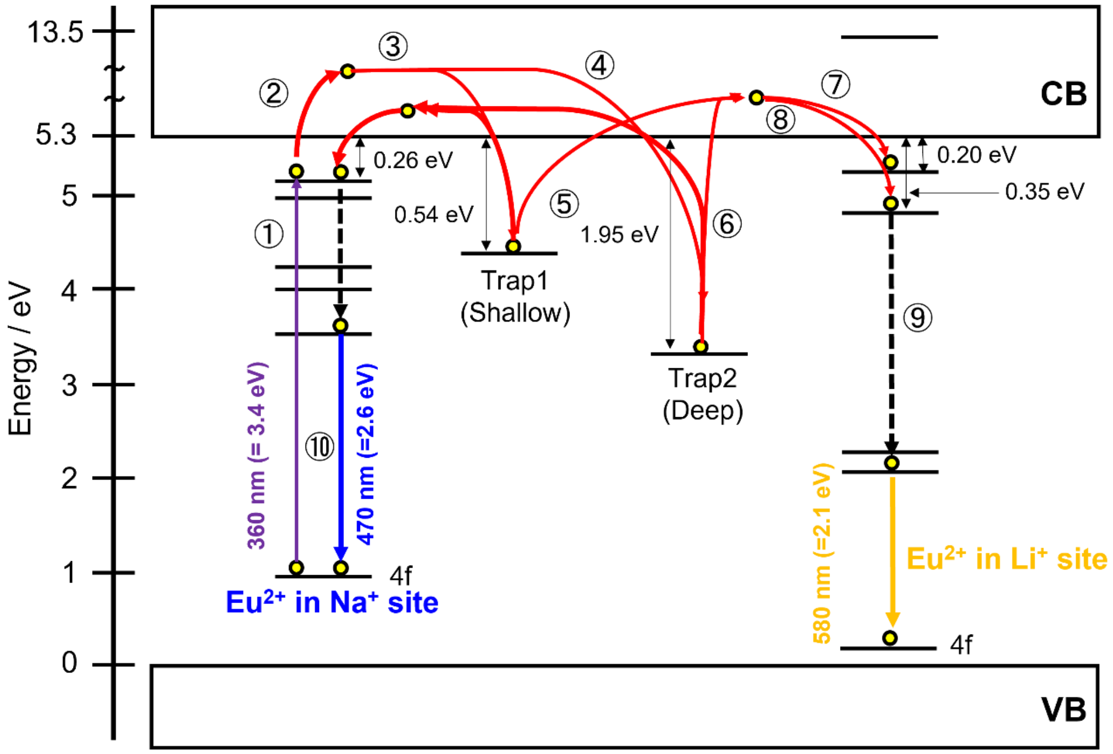

Fig. 2-9 Thermoluminescence mechanism for LNSF:$0.01Eu^{2+}$.

2-4 Conclusion

A novel Eu^{2+}-doped LNS phosphor with a multi-color white emission assisted through the combination of blue and yellow emissions was synthesized using a conventional solid-state reaction with a Na_2CO_3 flux. From the luminescence lifetime measurements, it can be concluded that the Eu^{2+} emission centers are located at not only the NaO_6 sites but also at the LiO_5 sites. The thermal stabilities of LNS:0.01Eu^{2+} and LNSF:0.01Eu^{2+} phosphors were found to be much better in comparison with the reported silicate phosphors. The origin of the high thermal stability of the phosphors is derived from the substituting Eu^{2+} ions at both alkali sites producing electron-trapping defects that can be responsible for Eu^{2+} emissions at high temperatures.

Chapter 3.

High Thermal Stable Blue-Emitting Alkali Silicate Phosphor, Eu^{2+}-activated $Na_2Mg_2Si_6O_{15}$

3-1 Introduction

Eu^{2+} and Ce^{3+} ions are frequently used due to an its attractive luminescent properties, 4f - 5d transition which can accomplish high emission efficiency. Moreover, they can change the luminescent properties depending on the crystal structure of the host lattice.[97] For example, $BaMgAl_{10}O_{17}$:Eu^{2+}, Ba_2SiO_4:Eu^{2+} and $CaAlSiN_3$:Eu^{2+}, although they consist of the same emission ion, the emission color shows blue, green and red, respectively due to the 4f - 5d allowed transition.[85, 98, 99] In this Chapter, we focus on blue-emitting phosphor materials. In blue-emitting phosphors doped emission ions, Tm^{3+} and Eu^{2+} are often included.[88, 100, 101] However, the emission efficiency of Tm^{3+}-activated phosphors is inferior to that of Eu^{2+}-doped blue emitting phosphors owing to the 4f - 4f forbidden transition of Tm^{3+}. In the previous work, it is well known that Eu^{2+}-activated $BaMgAl_{10}O_{17}$ (BAM:Eu^{2+}) has the great emission efficiency.[102] On the other hand, the thermal stability of BAM:Eu^{2+} at high temperature is poor. In addition, the synthesis of BAM:Eu^{2+} is difficult due to the high temperature heating (1600℃) for several hours.[103, 104] Thus, novel blue emitting phosphors which can be synthesized easily have been developed. In this paper, we concentrate on the Eu^{2+}-activated phosphors substituted into alkaline sites. Most of Eu^{2+}-activated phosphors can appear the luminescent properties by Eu^{2+} substituting into alkaline earth sites, Ca^{2+}, Sr^{2+} and Ba^{2+} because the ionic radius and the charge state of alkaline earth elements are similar to Eu^{2+}. Nevertheless, Eu^{2+}-activated phosphors substituted alkaline sites such as Na^+ and K^+ have been reported recently (Ex. $NaMgPO_4:Eu^{2+}$, $NaScSi_2O_6:Eu^{2+}$, $Na_3Sc_2(PO_4)_3:Eu^{2+}$ and $NaAlSiO_4:Eu^{2+}$).[64-67, 69, 105] In these papers, Eu^{2+} ion is occupied for Na^+ sites because the ionic radius of Eu^{2+} and Na^+ are resemble. Even if the reports of Eu^{2+}-activated alkaline phosphors have a few, the luminescent properties are marvelous in terms of the thermal stability and efficient fluorescent attribute. In particular, Eu^{2+}-activated alkali lithosilicate phosphors such as $Li_3NaSiO_4:Eu^{2+}$, $KLi_3SiO_4:Eu^{2+}$, $NaK_7[Li_3SiO_4]_8:Eu^{2+}$, $RbNa_3Li(Li_3SiO_4)_4:Eu^{2+}$ and $RbLi(Li_3SiO_4)_2:Eu^{2+}$ have been reported in this year.[106-110] Eu^{2+}-alkaline lithosilicate phosphors have special characteristics, such as the narrow band emission and high thermal stability. Hence, Eu^{2+}-activated alkali phosphors have been attentions rapidly due to their glamorous luminescent properties. In this study, we select the alkali silicate $Na_2Mg_2Si_6O_{15}$ as a phosphor host crystal. The crystal structure of $Na_2Mg_2Si_6O_{15}$ shows Tuhualite.[111] However, Eu^{2+}-doped Tuhualite phosphor has not been reported yet. Hence, the luminescent characteristics of Eu^{2+} ions in Tuhualite structure are indeterminate.

In Chapter 3, We prepared Eu^{2+}-doped $Na_2Mg_2Si_6O_{15}$ powder by the solid-state reaction. Moreover, we conducted the measurement of photoluminescence and thermal quenching properties. As a result, Eu^{2+}-activated $Na_2Mg_2Si_6O_{15}$ shows the broad blue emission and higher thermal stability than that of Eu^{2+}-doped phosphors

3-2 Material procedure

3-2-1 Experimental

Eu^{2+}-activated $Na_2Mg_2Si_6O_{16}$ phosphors were synthesized by the conventional solid-state reaction. Na_2CO_3 (Kanto Chemical Co., Inc., 99.0%), MgO (Kanto Chemical Co., Inc., 99.99%), SiO_2 (Kanto Chemical Co., Inc., 99.9%) and Eu_2O_3 (Shin-etsu Chemical Co., Inc., 99.99%) were mixed at stoichiometry ratio using an agate mortar with acetone. Then, the mixtures were calcined at 1273 K for 6 h in air in order to CO_2 and H_2O. Next, these mixtures were heated at 1273 K for 6 h in a reducing atmosphere (95 Vol. % Ar, 5 vol. % H_2) for reduction from Eu^{3+} to Eu^{2+} using a tube furnace.

3-2-2 Characterization

Powder X-ray diffraction (XRD) patterns were obtained using an X-ray diffractometer (MX-Labo, Mac Science Co., Ltd.) with monochromatic Cu$K\alpha$ radiation (λ= 1.54056 Å) under 25 mA and 40 kV. Photoluminescence (PL), photoluminescence excitation (PLE) spectra, and thermal stability were measured at room temperature using a spectrofluorometer (FP-6500/FP-6600, Jasco, Inc.) with a 150 W Xenon lamp.

3-3. Results and Discussion

3-3-1 XRD and Crystal structure

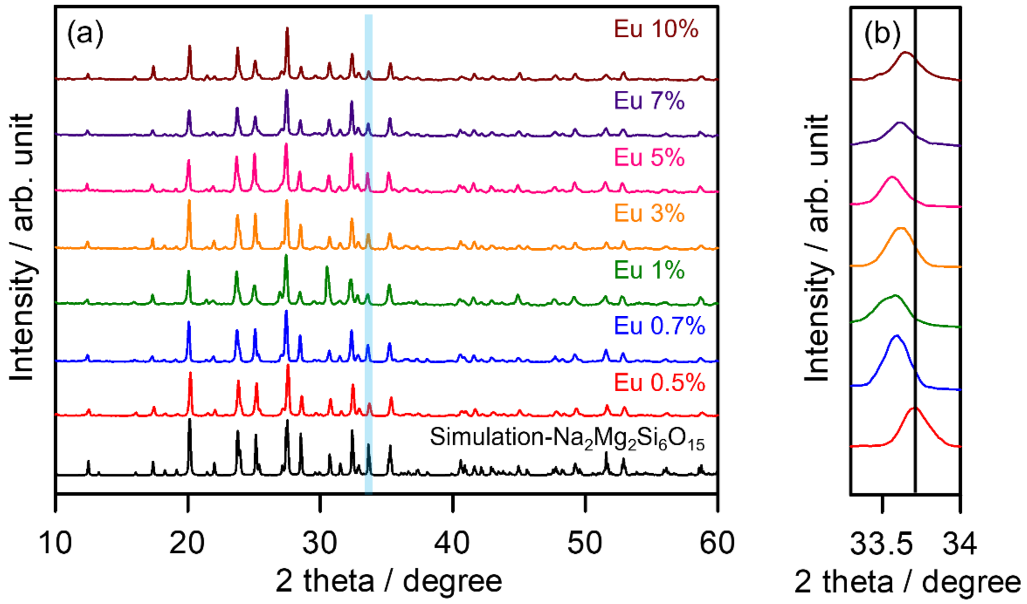

Fig. 3-1(a) XRD patterns of $Na_{2(1-x)}MgSi_6O_{16}$:2*x*Eu^{2+} (*x* = 0.005, 0.007, 0.01, 0.03, 0.05, 0.07, 0.1) and (b) enlarged view (33° - 34°) of the XRD patterns of the $Na_{2(1-x)}Mg_2Si_6O_{15}$:2*x*$Eu^{2+}$ (*x* = 0.005, 0.007, 0.01, 0.03, 0.05, 0.07, 0.1).

Fig. 3-1(a) shows the XRD patterns of $Na_{2(1-x)}MgSi_6O_{16}$:2*x*Eu^{2+} (*x* = 0.005, 0.007, 0.01, 0.03, 0.05, 0.07, 0.1). Consequently, the XRD patterns of all samples show the orthorhombic $Na_2Mg_2Si_6O_{15}$ simulation pattern perfectly without impurity phases. Moreover, the enlarged view (33°-34°) of the XRD patterns of the $Na_{2(1-x)}Mg_2Si_6O_{15}$:2*x*$Eu^{2+}$ (*x* = 0.005, 0.007, 0.01, 0.03, 0.05, 0.07, 0.1) are shown in Fig. 3-1(b). The diffraction peaks of the majority of samples show a little shift to lower diffraction angles with increasing the concentration of the Eu^{2+}, which indicates that the Eu^{2+} succeeds in occupying the substitutional sites in

$Na_2Mg_2Si_6O_{15}$. Next, we discuss the crystal structure of orthorhombic $Na_2Mg_2Si_6O_{15}$ in order to identify the substitutional sites of Eu^{2+}.

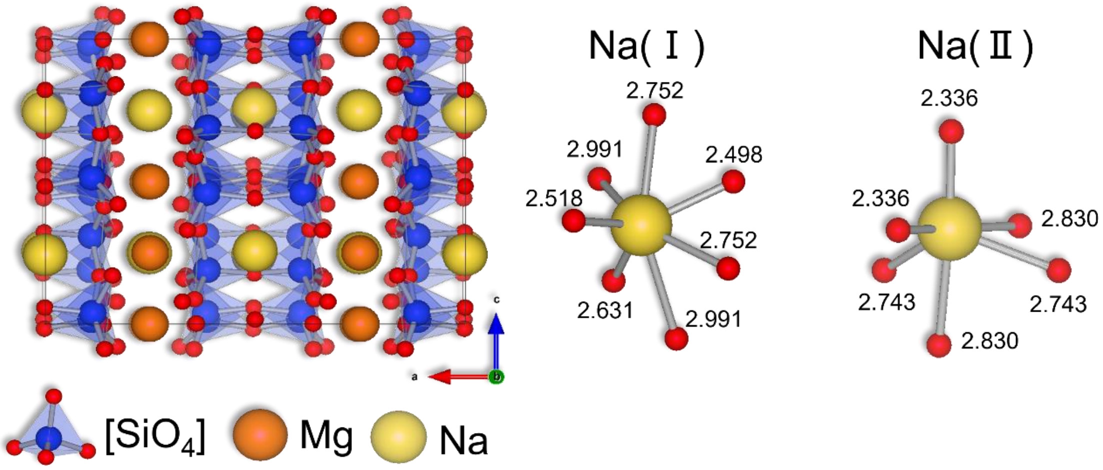

Fig. 3-2 Crystal structure of $Na_2Mg_2Si_6O_{15}$ and two different crystallographic sodium sites illustrated by VESTA program

Fig. 3-2 shows the crystal structure of $Na_2Mg_2Si_6O_{15}$ illustrated by using VESTA program.[77] The lattice parameters are a = 14.65 Å, b = 17.59 Å and c = 12.05 Å for an orthorhombic system with a space group *Cmca* (No. 64). This crystal structure includes two Na sites, NaO_6 and NaO_7 polyhedron as shown in Fig. 3-2. According to Shannon, the ionic radius of Eu^{2+} shows 1.17 Å (with a 6-fold coordination) and 1.20 Å (with a 7-fold coordination). Moreover, it reports that the ionic radius of Na^+ is 1.02 Å (with a 6-fold coordination) and 1.12 Å (with a 7-fold coordination), respectively.[78] Peng et al. and Pires et al. proposed that the acceptable percentage difference between the doped and substituted ions must not exceed ±30%.[112, 113] The acceptable percentage difference is calculated as following equation (1):

$$D_r = \frac{[R_m(CN) - R_d(CN)]}{R_m(CN)} \times 100 \quad (1)$$

where D_r is the ionic radius percentage difference, $R_m(CN)$ means the radius of the host cation (CN means the coordination number) and $R_d(CN)$ is the ionic radius of doped ion, respectively. Based on the equation (1), Table 3-1 shows the result of D_r values in $Na_2Mg_2Si_6O_{15}$ structure when Eu^{2+} ion is doping. The ionic radius of Eu^{2+} with a 4-fold coordination data have not been reported, hence we carry out the calculation about MgO_6, and NaO_6 and NaO_7. Table 3-1 indicates that Eu^{2+} ion occupies two Na^+ sites, especially NaO_7 sites. Although the charge of Mg^{2+} is the same as Eu^{2+}, it seems to be difficult for Eu^{2+} ion to substitute for MgO_6 sites because its D_r value exceeds ±30%.

Table 3-1 Calculate date of D_r in $Na_2Mg_2Si_6O_{15}$.

Ions	Ionic radius [Å]	D_r [%]
Eu^{2+} (6–fold coordination)	1.17	-
Eu^{2+} (7–fold coordination)	1.20	-
Na^+ (6–fold coordination)	1.02	-14.706
Na^+ (7–fold coordination)	1.12	-7.143
Mg^{2+} (6–fold coordination)	0.72	-62.5

3-3-2 PL and PLE

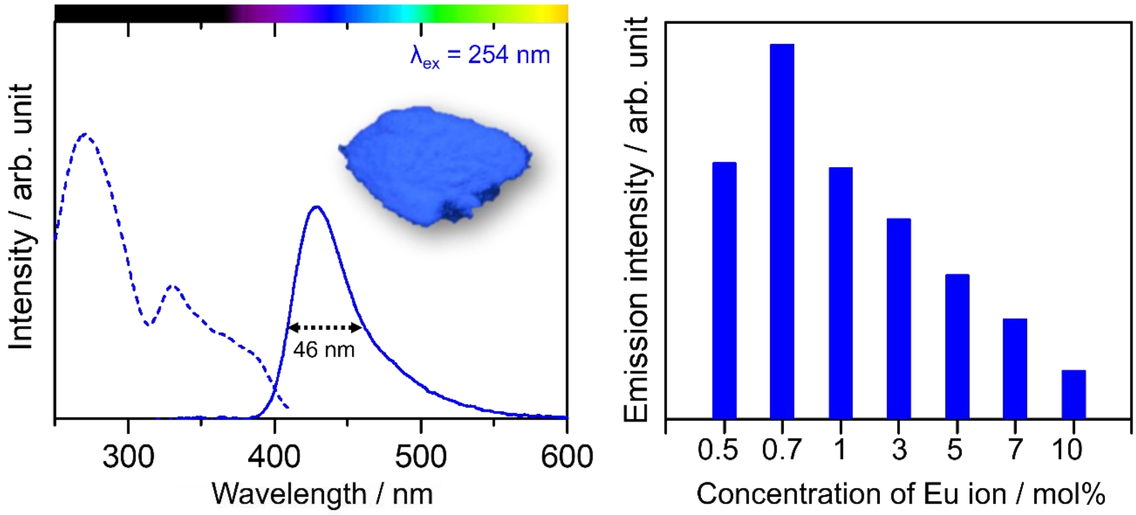

Fig. 3-3(a) PL and PLE spectra of $Na_{1.986}Mg_2Si_6O_{15}$:$0.14Eu^{2+}$ (Insert photograph of blue-emitting sample under 254 nm excitation) and (b) the dependence of the emission peak (λ_{em} = 430 nm) intensities on the concentration of Eu^{2+} in the $Na_2Mg_2Si_6O_{15}$.

Fig. 3-3(a) shows the emission and excitation spectra of $Na_{1.986}Mg_2Si_6O_{15}$:$0.014Eu^{2+}$. All Eu^{2+}-activated $Na_2Mg_2Si_6O_{15}$ phosphors show a broad emission band from 400 nm to 550 nm due to 4f - 5d allowed transition of Eu^{2+}. From the previous section, Eu^{2+}-doped $Na_2Mg_2Si_6O_{15}$ can emit the blue emission at approximately 430 nm by Eu^{2+} occupying two Na sites. The charge imbalance should occur because the substitution of Eu^{2+} into Na^+ sites is proceeded between different charge ions. However, previous reports suggests that Eu^{2+}-doped phosphor materials substituted in Na^+ sites generate a single vacancy explained the Kröger-Vink, as following equation (2):

$$\mathrm{Eu} \rightarrow \mathrm{Eu}_{\mathrm{Na}}^{\cdot} + V_{\mathrm{Na}}' \quad (2)$$

where V_{Na}' is formed when Eu^{2+} is substituted for the Na sites. Hence, the charge balance in Eu^{2+}-activated $Na_2Mg_2Si_6O_{15}$ is neutral.[109] Moreover, the dependence of the emission intensity on the concentration Eu^{2+} ion is shown in Fig. 3 (b). It indicates that the optimal concentration of Eu^{2+} in $Na_2Mg_2Si_6O_{15}$ is 0.7 mol% because the emission intensity of $Na_2Mg_2Si_6O_{15}:Eu^{2+}$ decreases gradually owing to the energy transfer among Eu^{2+} ions as the concentration of the emission ion increases from 0.7 mol%. Furthermore, the determination of the mechanism of the energy transfer among emission ions is suggested by Blasse, as in equation (3):[91, 114, 115]

$$R_c = 2\left[\frac{3V}{4\pi x_c Z}\right]^{1/3} (3)$$

where R_c is the critical distance, V means the cell volume, x_c is the total concentration of doping ions and Z refers to the number of formula units per unit cell, respectively. In the case of $Na_2Mg_2Si_6O_{15}$ structure, V = 254.27 Å^3, x_c = 0.007, Z = 8, thus the critical distance R_c estimates 4.43 nm, which is extremely longer than that of the nearest distance between NaO_6 and NaO_7 sites (4.73 Å). It indicates that the energy transfer among Eu^{2+} ions in $Na_2Mg_2Si_6O_{15}$ occurs actively. Thus, the optimal concentration of Eu^{2+} in $Na_2Mg_2Si_6O_{15}$ structure is reasonable based on the calculation from the equation (3). Furthermore, the emission band of $Na_2Mg_2Si_6O_{15}:Eu^{2+}$ is asymmetric shape because Eu^{2+} occupies two substitutional sites, NaO_6 and NaO_7. Thus, we carried out the peak deconvolution of the emission spectrum. As a result, we succeeded in separating the emission band as two components (Fig. 3-4).

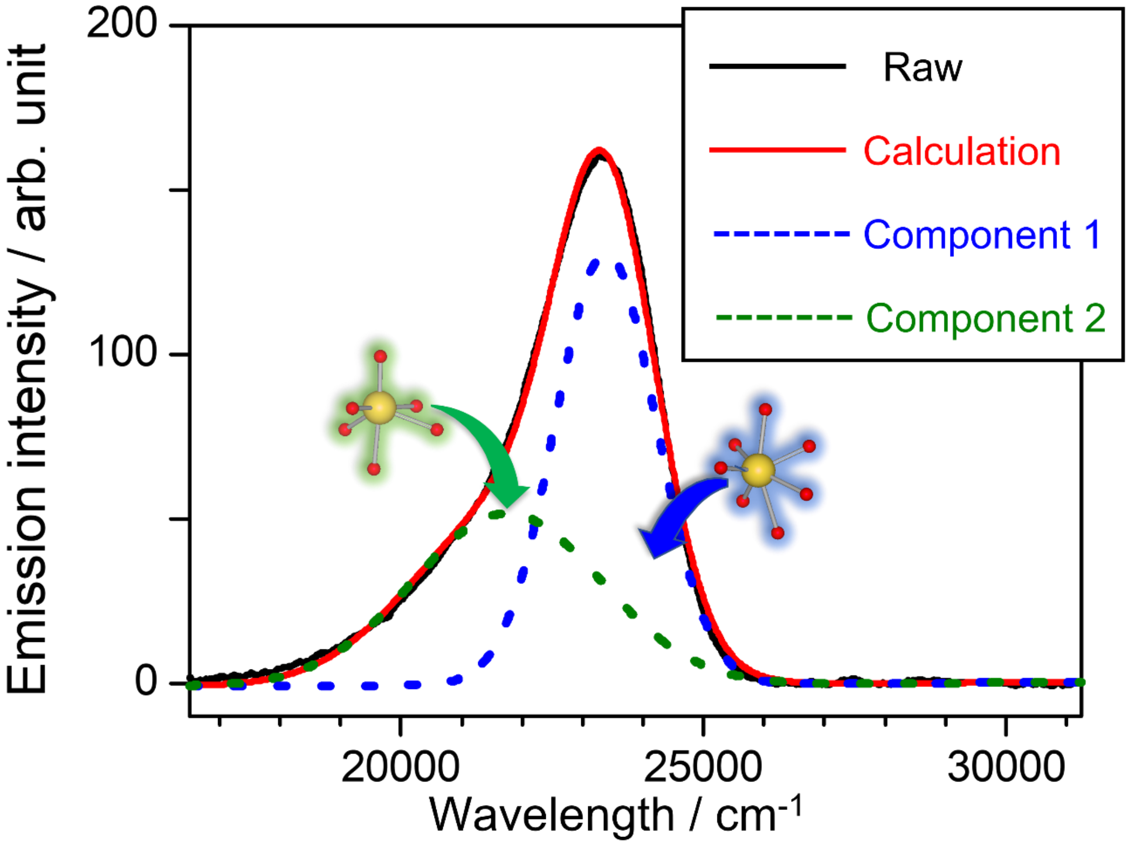

Fig. 3-4 The deconvolution of emission spectrum for $Na_{1.986}Mg_2Si_6O_{15}$:$0.014Eu^{2+}$.

According to Henderson *et al.*, the relationship between the crystal field strength of cation sites and the average bond length for the surrounding sites is expressed by the equation (4):

$$Dq \propto \frac{1}{R^5} \quad (1)$$

where Dq means the crystal field strength and R is the average bond distance of sites.[79] Based on this equation (4), the crystal field strength of NaO_6 is stronger than that of NaO_7 because the average bond length of NaO_6 (2.63 Å) is smaller than that of NaO_7 (2.73 Å) (Fig.3-2(b)).

3-3-3 Thermal Stability

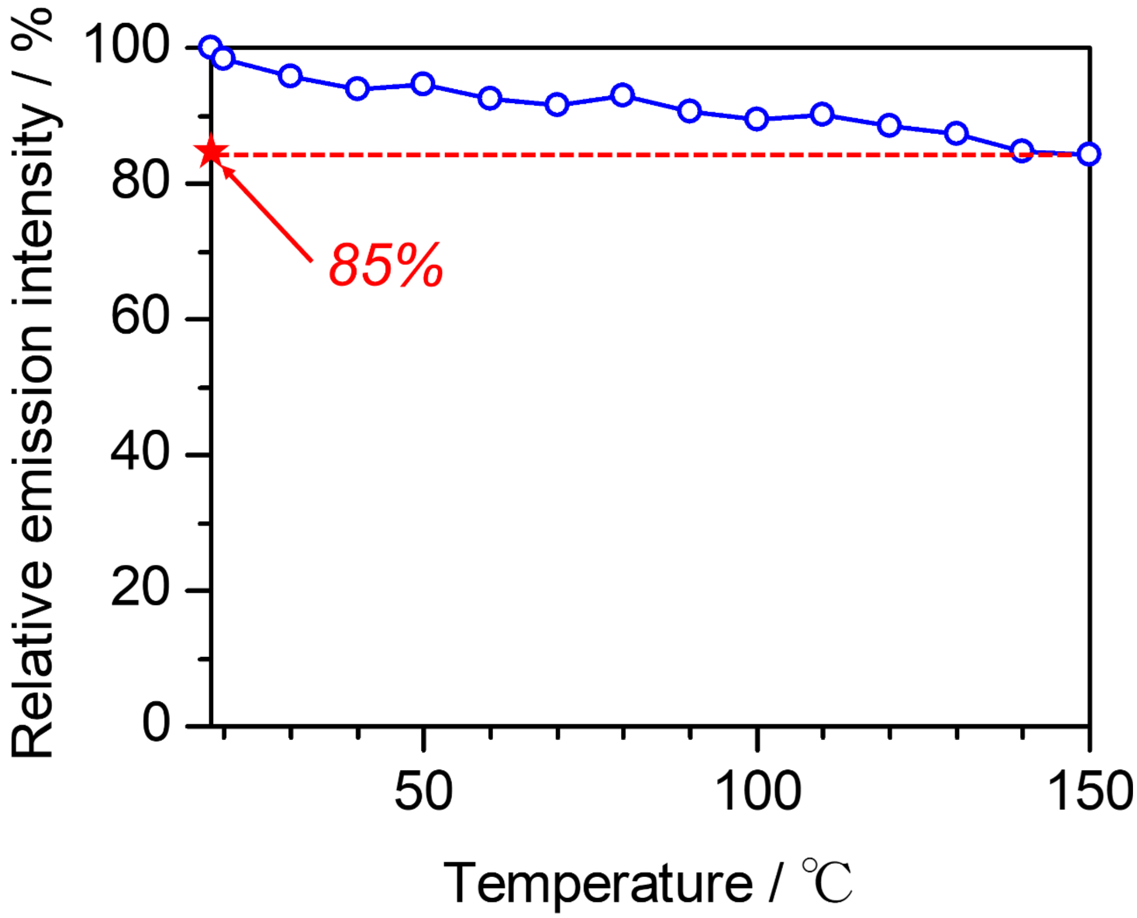

Fig. 3-5 Temperature dependence of relative emission intensity for $Na_{1.986}Mg_2Si_6O_{15}$:0.014Eu^{2+}.

It is quite important for phosphor materials to measure the thermal stability at high temperature because the temperature in most of luminescent devices rises when they are driven.[116] Therefore, the temperature dependence of relative intensities for $Na_{1.986}Mg_2Si_6O_{15}$:0.014Eu^{2+} is shown in Fig. 3-5 in order to evaluate the influence of the emission intensity in Eu^{2+}-activated $Na_2Mg_2Si_6O_{15}$. The higher the room temperature increases from room temperature, the more the emission intensity of Eu^{2+}-activated $Na_2Mg_2Si_6O_{15}$ decreases due to the thermal quenching.

However, compared with other Eu^{2+}-activated phosphors, such as $(Ba,Ca)_2SiO_4$:Eu^{2+}, $NaAlSiO_4$:Eu^{2+} (Nepheline) and Li_3NaSiO_4:Eu^{2+} , the emission intensity of $Na_{1.986}Mg_2Si_6O_{15}$:0.014Eu^{2+} at 150℃ keeps about 85%.[68, 109, 117] It indicates that the thermal stability of $Na_{1.986}Mg_2Si_6O_{15}$:0.014Eu^{2+} is considerably higher than that of other Eu^{2+}-activated silicate phosphors. Therefore, $Na_2Mg_2Si_6O_{15}$:Eu^{2+} phosphor can be useful under the high temperature environment such as driving luminescent devices. According to our previous study, we revealed that the vacancies that generate when emission ions dope into alkaline sites act as an electron trap and assist the thermal stability at high temperature by release the electron from the trap levels to the emission level of Eu^{2+}.[109] In addition, Kim *et al*. and Wang et al. proposed that the emission intensities of $Na_3Sc_2(PO_4)_3$:Eu^{2+} exceed 100% above 100℃ because the sodium vacancy (V'_{Na}) locates between the valence band and conduction band, which means this vacancy behaves as the trap level.[64, 118] Moreover, although the relationship between the thermal stability and the substitution of Eu^{2+} into alkaline sites have not been revealed completely, the thermal stability of Eu^{2+}-activated alkaline phosphors is quite marvelous, such as Li_3NaSiO_4:Eu^{2+}, $NaMgPO_4$:Eu^{2+} (olivine), $NaAlSiO_4$:Eu^{2+} (Nepheline), $KMg_4(PO_4)_3$:Eu^{2+} and $RbNa_3(Li_3SiO_4)_4$:Eu^{2+}.[67, 107, 109, 119] Thus, we must continue to study the mechanism of the thermal stability in phosphors substituted into alkaline sites.

3-4 Conclusion

Novel blue-emitting alkaline silicate phosphors, Eu^{2+}-activated $Na_2Mg_2Si_6O_{15}$ have been obtained by the conventional solid-state reaction for the first time. Eu^{2+} - activated $Na_2Mg_2Si_6O_{15}$ phosphors exhibits the broad emission from 400 nm to 550 nm due to the 4f -5d allowed transition. Moreover, it indicates that Eu^{2+} ions occupy the NaO_6 and NaO_7 sites based on the calculation. The thermal stability of $Na_2Mg_2Si_6O_{15}:Eu^{2+}$ is extremely stronger than that of Eu^{2+}-activated phosphors. Thus, it indicates that novel $Na_2Mg_2Si_6O_{15}:Eu^{2+}$ phosphors have excellent luminescent properties for the luminescent properties.

Chapter 4.

Emission shift from green yellow to reddish orange in Eu^{2+}-activated $Ca_6BaP_4O_{17}$ by doping high amount of activator ion

4-1 Introduction

Eu^{2+} or Ce^{3+} rare earth ion is often used as activator ions for highly efficient downshift phosphors due to their characteristic luminescent properties. These emission ions display the 5d - 4f allowed electron transition with a higher emission efficiency than rare earth ions with the 4f - 4f forbidden transition (Eu^{3+}, Tb^{3+}, Dy^{3+} and Tm^{3+}, and others). Moreover, the optical properties of Eu^{2+}- and Ce^{3+} emission ions are strongly dependent on host materials because the 5d orbitals are more sensitive to the coordination environment than 4f orbitals, which are shielded by outer 5s and 5p orbitals.[120] Therefore, it is extremely important for synthesizing novel Eu^{2+}- and Ce^{3+}- doped luminescent materials to select appropriate host materials.

Typical red-emission phosphors are often Eu^{2+}-activated nitride phosphors, such as $CaAlSiN_3:Eu^{2+}$, $SrLiAl_3N_4:Eu^{2+}$, and $Sr_2Si_5N_8:Eu^{2+}$.[75, 121, 122] It is well known that these Eu^{2+}-doped red-emitting nitride materials exhibit high luminescence efficiency and excellent thermal stability. However, the synthesis of nitride materials usually requires a special furnace to control high temperatures (over 2000 ℃) and high pressures, hence nitride phosphor materials are unsuitable for commercial application owing to their high mass-production costs. Therefore, novel oxide phosphors that can exhibit red emissions under blue light excitation are desirable because they are easily treated and obtainable via the conventional solid-state reaction at a lower temperature than that of nitride synthesis.[123]

Currently, doping high concentrations of Eu^{2+} or Ce^{3+} ions with the 4f - 5d allowed transition into oxide host materials is one of the most effective methods for producing red-emitting oxide phosphors.[124, 125] For instance, the drastic emission redshift from the green to the yellow of Eu^{2+}-activated $(Sr,Ba)_2SiO_4$ orthosilicate phosphors occurs by incorporating high concentrations of Eu^{2+} ions.[70, 126] Furthermore, $Sr_6Y_2Al_4O_{15}$ doped with 10 mol% Ce^{3+} showed an abnormal broad-red emission under blue light irradiation because the cerium ions replaced the Y^{3+} octahedral sites and formed strong crystal field sites, while the blue emission owing to Ce^{3+} ions in Sr^{2+} sites was also present.[127] Thus, the introduction of high concentrations of activators with the 4f - 5d allowed transition is a useful technique for developing oxide phosphors that are red-emitting under blue light irradiation.

In Chapter 4, we focus on Eu^{2+}-activated $Ca_6BaP_4O_{17}$ phosphors, which can exhibit a green-yellow emission when excited by blue or ultraviolet light. Researchers have already thoroughly investigated the unique optical properties of these phosphors such as thermal quenching behavior and the persistence.[128-131] However, the emission-color tuning of Eu^{2+}-activated $Ca_6BaP_4O_{17}$ phosphors by adjusting the amount of activator ions has not been previously researched. The crystal structure of the $Ca_6BaP_4O_{17}$ host consists of three different crystallographic sites, CaO_7, CaO_8, and BaO_{12}. Hence, it is expected that the drastic emission redshift in the Eu^{2+}-activated $Ca_6BaP_4O_{17}$ phosphor occurs due to the presence of three substitution locations for the Eu^{2+} ion.

In this section, $Ca_6BaP_4O_{17}:Eu^{2+}$ phosphors were synthesized by the conventional solid state reaction method. The crystal structure, lattice parameters, and site occupancies in Eu^{2+}-activated $Ca_6BaP_4O_{17}$ were identified by Rietveld refinement analysis from X-ray powder diffraction (XRD). Moreover, their emission and excitation spectra, International Commission on Illumination (CIE) chromaticity coordinates, the quantum yield, the lifetimes of the Eu^{2+} ion, the thermal quenching properties, and the fabrication of prototype wLEDs were all systematically investigated.

4-2 Material procedure

4-2-1 Materials synthesis

Eu^{2+}-activated $Ca_6BaP_4O_{17}$ phosphors were synthesized by the conventional solid-state reaction. $CaCO_3$ (Kanto Chemical Co., Inc., 99.99%), $BaCO_3$ (Kanto Chemical Co., Inc., 99.99%), $(NH_4)_2HPO_4$ (Kanto Chemical Co., Inc., 99.0%), Eu_2O_3 (Shin-etsu Chemical Co., Inc., 99.99%) were weighted in the stoichiometric ratio of Ca : Ba : P : Eu = $6(1-x) : 1 : 4 : 6x$ ($0 \leq x \leq 0.20$). Then, sorted raw materials were mixed in acetone with an agate mortar. After drying, the mixtures were pelleted and heated at 1250℃ for 6 h in a reducing atmosphere (95 vol.% Ar / 5 vol.% H_2) for the reduction from Eu^{3+} to Eu^{2+}. Finally, the sintered phosphate materials were ground and characterized.

4-2-2 Fabrication of prototype wLEDs

The synthesized $Ca_{6(1-x)}Eu_{6x}BaP_4O_{17}$ (x = 0.01, 0.05, 0.10 and 0.20) phosphor was dispersed in a transparent silicon resin. Then, the mixture was put on a flat-mount-type blue LED chip (GM5BC03210Z, SHARP Co.).

4-2-3 Characterization

XRD patterns were obtained using an X-ray diffractometer (D2 PHASER; Bruker) with monochromatic Cu*Kα* radiation (λ = 1.54056 Å) under 10 mA and 30 kV. Rietveld refinement was carried out using RIETAN-FP software. [76] The reflection and absorption spectra of samples were evaluated by a diffuse reflectance spectrum (DRS) (V-700DS; Jasco Corp.) based on $BaSO_4$ white powder as a reference. Photoluminescence (PL) and photoluminescence excitation (PLE) spectra were measured at using a spectrofluorometer (FP-6500 / FP-6600; Jasco Inc.) with a 150 W Xenon lamp at room temperature. The decay curves of Eu^{2+} in $Ca_6BaP_4O_{17}$ were measured by Quantaurus-Tau (Hamamatsu Photonics Inc.). The absolute quantum efficiency (QE) was measured in an integrating sphere (ISF-834; Jasco Corp.) using a photoluminescence spectrometer (FP-8500; Jasco Corp.), where a standard halogen lamp (ESC-842; Jasco Corp.) was used for calibration of this measurement system. The chromaticity diagrams of Eu^{2+}-activated $Ca_6BaP_4O_{17}$ phosphors were analyzed with a PMA-12 multi-channel spectroscope (C7473-36N, Hamamatsu Photonics Inc.). The electroluminescence (EL) spectra of the prototype wLEDs was measured by a DC power supply with a current of 30 mA and a voltage of 2.0 V, and was detected using a PMA-12 multi-channel spectroscope (C7473-36N, Hamamatsu Photonics Inc.).

4-3 Results and discussion

4-3-1 XRD measurement and Rietveld refinement

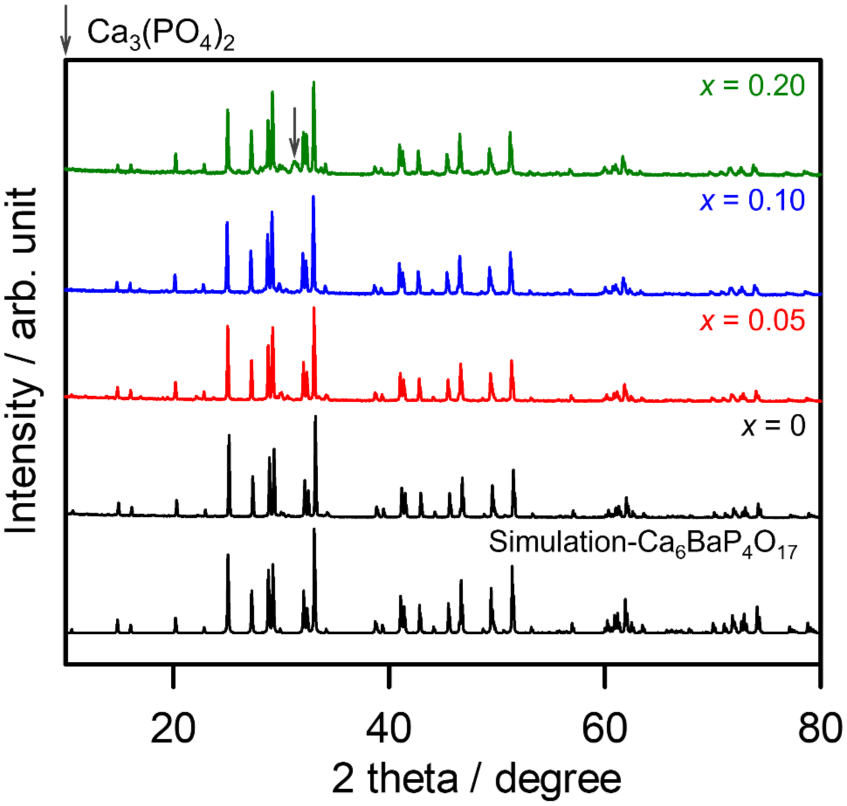

Fig. 4-1 XRD patterns of $Ca_{6(1-x)}Eu_{6x}BaP_4O_{17}$ (x = 0, 0.05, 0.10, 0.20).

The XRD patterns of $Ca_{6(1-x)}Eu_{6x}BaP_4O_{17}$ (x = 0, 0.05, 0.10, 0.20) are shown in Fig. 4-1. The simulation pattern of $Ca_6BaP_4O_{17}$ was calculated from the crystal information file reported by Komuro *et al.*[132] The diffraction peaks of the synthesized materials in this work are mainly in good agreement with the calculated patterns of $Ca_6BaP_4O_{17}$, while an undesirable diffraction peak owing to $Ca_3(PO_4)_2$ appeared around 2 theta = 30 degrees as an impurity phase in x = 0.20. To determine the phase purity in the host and Eu^{2+}-doped $Ca_6BaP_4O_{17}$ samples, Rietveld analysis was implemented for Eu^{2+}-non doped and doped

$Ca_6BaP_4O_{17}$ samples.

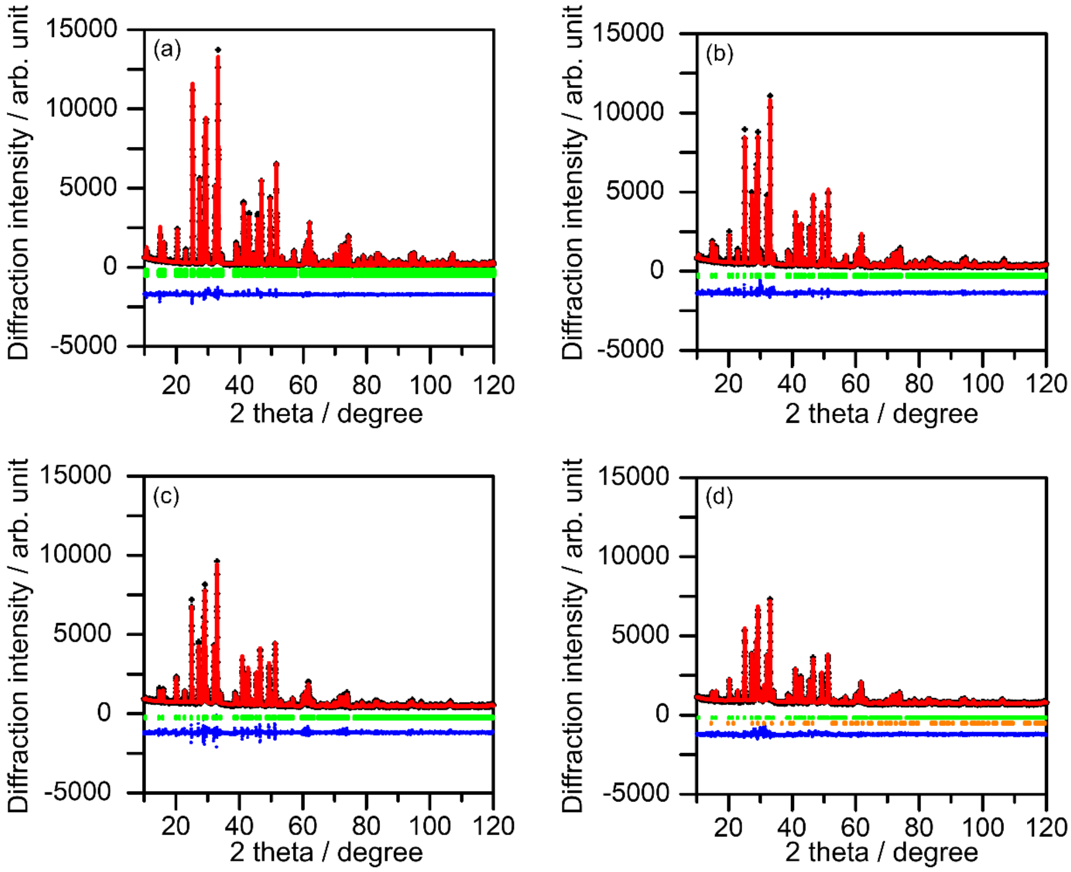

Fig. 4-2 Raw (black circle symbol), calculated (red solid line), Bragg position (green solid line) and difference (blue solid line) patterns obtained from Rietveld refinement on X-ray powder diffraction data of (a) $x = 0$, (b) $x = 0.05$ (c) $x = 0.10$ and (d) $x = 0.20$. Only the $Ca_{4.80}Eu_{1.20}BaP_4O_{17}$ sample was refined by multiphase analysis (first phase: $Ca_6BaP_4O_{17}$ (Bragg position: green), second phase: $Ca_3(PO_4)_2$ (Bragg position: orange)).

Fig. 4-2(a)-(d) shows the fitting patterns obtained from the Rietveld refinements for the $Ca_{6(1-x)}Eu_{6x}BaP_4O_{17}$ (x = 0, 0.05, 0.10, 0.20). The refined crystallographic parameters from the Rietveld refinements are summarized in Table 4-1. In the

Rietveld refinement, the isotropic thermal atomic displacement parameters B_{eq} for all anions were constrained to be the same value as the reported crystallographic data because these parameters could not be refined to be positive (Table 2). As a result, the R-factor values of the host material were finally converged to R_{wp} = 8.973 %, R_p = 6.174 %, R_e = 5.106 % and S = 1.7574, respectively. S is the index for goodness-of-fit calculated by R_{wp}/R_e. Consequently, it indicated that the single phase $Ca_6BaP_4O_{17}$ host was successfully obtained without impurities.

Table 4-1 Lattice parameters and R values refined by the Rietveld analysis for $Ca_{6(1-x)}Eu_{6x}BaP_4O_{17}$ (x = 0, 0.05, 0.10, 0.20).

	x = 0	x = 0.05	x = 0.10	x = 0.20
System	Monoclinic			
S.G.	$C2/m$ (#12)			
a (Å)	12.303(1)	12.322(2)	12.308(2)	12.373(4)
b (Å)	7.1044(2)	7.1095(3)	7.1132(1)	7.1396(6)
c (Å)	11.7160(8)	11.730(1)	11.7197(8)	11.773(3)
β (°)	134.444(4)	134.465(7)	134.448(3)	134.49(1)
V (Å^3)	731.09(10)	733.3(2)	732.50(8)	741.9(3)
R_{wp} (%)	8.973	8.345	7.575	5.954
R_p (%)	6.174	5.705	5.753	4.070
R_e (%)	5.106	4.250	3.787	3.295
S	1.757	1.963	2.001	1.807

For the x = 0.20 sample, the lattice and crystallographic parameters were refined using multiphase analysis (first phase : $Ca_6BaP_4O_{17}$, second phase : $Ca_3(PO_4)_2$). As a result, a 12.7 mol% impurity phase, $Ca_3(PO_4)_2$, remained in the x = 0.20 sample. Furthermore, although it is well known that the $Ca_3(PO_4)_2$:Eu^{2+} phosphor exhibits a strong blue emission (λ_{em} = 416 nm) when excited by ultraviolet light

(λ_{ex} = 300 nm), the blue emission was not observed in the x = 0.20 sample under ultraviolet light irradiation. All optical measurements, photoluminescence, lifetime measurement, thermal quenching behavior are conducted under near ultraviolet (λ_{ex} = 405 nm) or blue light irradiation (λ_{ex} = 450 nm) for Eu^{2+}-activated $Ca_6BaP_4O_{17}$.Hence, the impurity phase $Ca_3(PO_4)_2$ in the x = 0.20 sample is negligible for the discussion of its luminescent properties.[133]

4-3-2 Crystal Structure

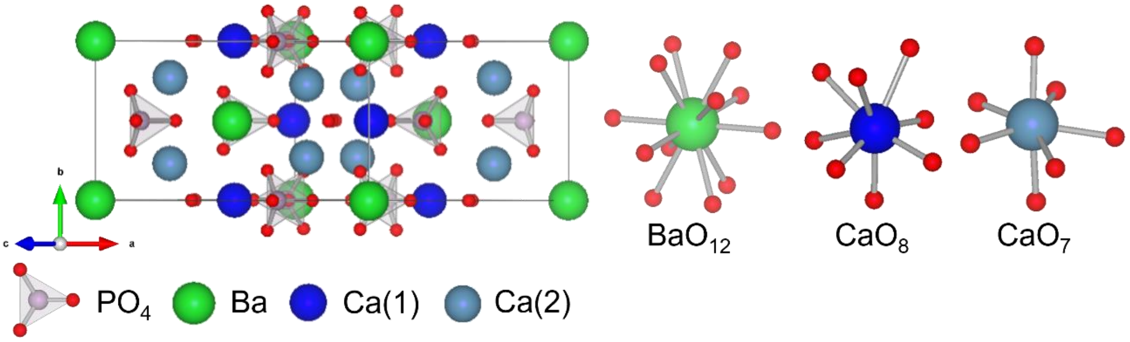

Fig. 4-3 Crystal structure of $Ca_6BaP_4O_{17}$ and substitutional sites for Eu^{2+} in the host crystal illustrated by VESTA program.

The crystal structure of $Ca_6BaP_4O_{17}$ refined by Rietveld analysis illustrated by the VESTA program is shown in Fig. 4-3.[77] $Ca_6BaP_4O_{17}$ formed a monoclinic crystal structure with the space group *C*2/*m* (No. 12). The refined lattice parameters were a = 12. 303(1) Å, b = 7.1044(2) Å, c = 11.7160(8) Å, β = 134.444(4)° and V = 731.09(10) Å^3, respectively. This structure contains one BaO_{12}, one CaO_7, one CaO_8, two PO_4 tetrahedrons and one isolated oxygen atom. Eu^{2+} generally substitutes for alkali sites in the host lattice because the ionic radius of the Eu^{2+} ion is similar to those of alkali earth metal ions Ca^{2+}, Sr^{2+} and Ba^{2+}. To determine the site preference of the activator ion in the $Ca_6BaP_4O_{17}$ host, the dependence of the cell volumes on the amount of Eu^{2+} ion in the $Ca_6BaP_4O_{17}$ host was investigated (See Table 4-1). The cell volumes of $Ca_{6(1-x)}Eu_{6x}BaP_4O_{17}$ expanded linearly with an increase in activator ions, implying that the Eu^{2+} ions (1.20 Å : the 7-fold coordination, 1.25 Å : the 8-fold coordination) preferentially occupy the smaller calcium sites, CaO_7 (1.06 Å : the 7-fold coordination) and CaO_8 (1.12 Å : the 8-fold coordination) than the barium site

(1.61 Å : the 7-fold coordination). In addition, the site occupancies of the Eu^{2+} ion in two calcium sites are also listed in Table 4-3. In the $Ca_{5.70}Eu_{0.30}BaP_4O_{17}$ sample (x = 0.05), the site occupancies of the Eu^{2+} ion exhibits approximately equal numbers in two calcium sites. However, as large amounts of the Eu^{2+} ion were incorporated into the $Ca_6BaP_4O_{17}$ lattice, more Eu^{2+} ions occupied the CaO_8 site than the CaO_7 site. Finally, in the $Ca_{4.80}Eu_{1.20}BaP_4O_{17}$ (x = 0.20) sample, the site occupancy of the Eu^{2+} ion in the CaO_7 site increases to 0.11(1), while that in the CaO_8 site is equal to that in the $Ca_{5.40}Eu_{0.60}BaP_4O_{17}$ sample (x = 0.10). In contrast, the amount of Eu^{2+} ion in the CaO_8 site steadily increases. This indicates that the Eu^{2+} ions are incorporated into the CaO_7 sites by doping a large amount of activator ions.

Table 4-3 Site occupancies of the Eu^{2+} ion in two calcium sites on $Ca_{6(1-x)}Eu_{6x}BaP_4O_{17}$ (x = 0.05, 0.10, 0.20).

Sample	CaO_8 (4i site)	CaO_7 (8j site)
x = 0.05	0.08(1)	0.070(7)
x = 0.10	0.20(2)	0.056(7)
x = 0.20	0.21(2)	0.11(1)

4-3-3 Diffuse reflectance spectra of $Ca_{6(1-x)}Eu_{6x}BaP_4O_{17}$ (x = 0, 0.05) and band gap calculation

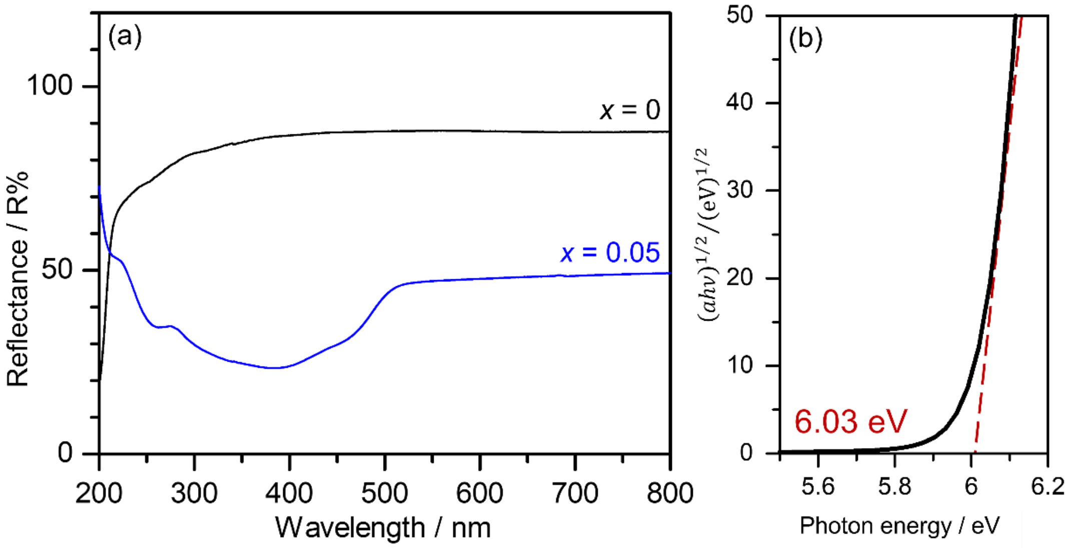

Fig. 4-4 (a) The diffuse reflectance spectra of $Ca_{6(1-x)}Eu_{6x}BaP_4O_{17}$ (x = 0 and 0.05) and (b) Kubelka-Munk spectrum for the band gap energy calculation of the $Ca_6BaP_4O_{17}$ host.

Fig. 4-4(a) shows the reflectance spectra of non-doped and $Ca_{5.70}Eu_{0.30}BaP_4O_{17}$ (x = 0.05) materials. In the non-doped $Ca_6BaP_4O_{17}$, the reflectance is higher than 80% around the visible region and drastically decreases from 400 nm, so that the body color of the host material is white. On the other hand, in the $Ca_{5.70}Eu_{0.30}BaP_4O_{17}$ sample (x = 0.05), the blue light absorption between 400 nm and 500 nm owing to the 4f - 5d absorption of the Eu^{2+} ion is clearly observed. Therefore, the Eu^{2+}-doped $Ca_6BaP_4O_{17}$ powders have a yellow body color. Moreover, to calculate the value of the band gap for the $Ca_6BaP_4O_{17}$ host, the Kubelka-Munk equation (K/S) was adopted in this study and the equation is following equation (1):[134-136]

$$(ah\nu)^{1/2} = \frac{K}{S} = \frac{(1-R)^2}{2R} \quad (1)$$

where K is the absorption coefficient, S represents the scattering coefficient and R is the reflectivity, respectively. As a result, the band gap energy of the synthesized $Ca_6BaP_4O_{17}$ was estimated to be 6.03 eV. (Fig. 4-4(b)) Compared with previous reports, according to Komuro et al., the band gap was calculated from the K-S function and the result was 6.2 eV.[132] Hence, the estimated band gap value of the $Ca_6BaP_4O_{17}$ host in this study is almost same as that in the previous study. Furthermore, compared with the band gap energies in other Eu^{2+}-doped phosphate phosphors such as $Ca_2Sr(PO_4)_2$ (5.3 eV), $Sr_4(PO_4)_2O$ (5.5 eV), and $KSrPO_4$ (5.1 eV), the band gap value of the $Ca_6BaP_4O_{17}$ host is slightly larger.[137-139]

4-3-4 PL and PLE

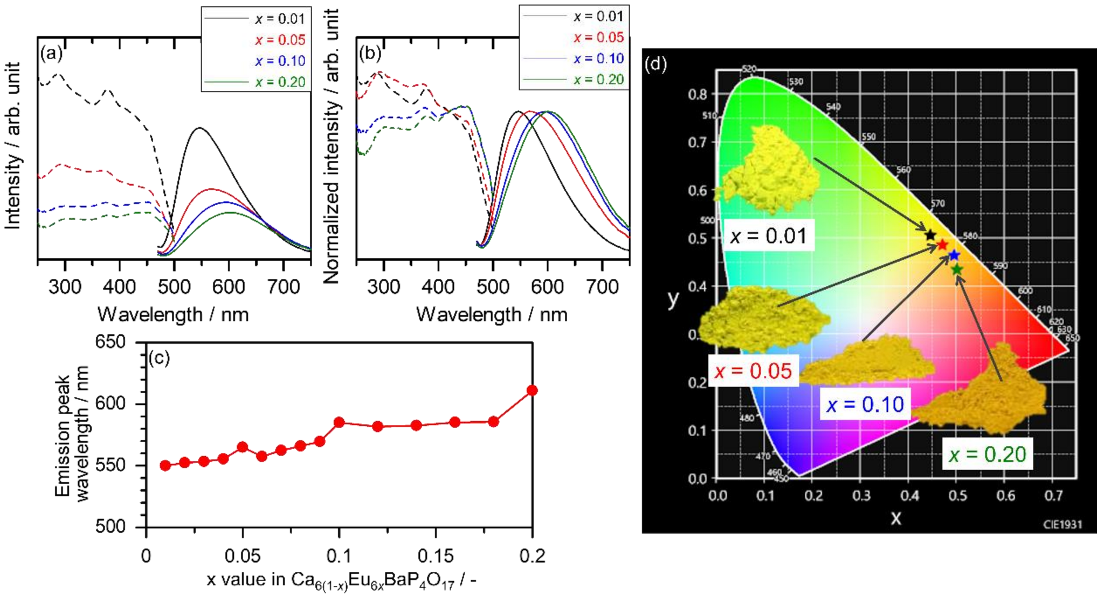

Fig. 4-5(a) Emission and excitation spectra of $Ca_{6(1-x)}Eu_{6x}BaP_4O_{17}$ (x = 0.01, 0.05, 0.10, 0.20) and (b) Normalized emission and excitation spectra of $Ca_{6(1-x)}Eu_{6x}BaP_4O_{17}$ (x = 0.01, 0.05, 0.10, 0.20). (c) The dependence of emission peak top on the Eu^{2+} concentration in the $Ca_6BaP_4O_{17}$ phosphors and (d) the chromaticty diagram of $Ca_{6(1-x)}Eu_{6x}BaP_4O_{17}$ (x = 0.01, 0.05, 0.10, 0.20).

PL and PLE spectra of $Ca_{6(1-x)}Eu_{6x}BaP_4O_{17}$ (x = 0.01, 0.05, 0.10, 0.20) are shown in Fig. 4-5(a). Emission bands of all samples were monitored at λ_{ex} = 450 nm. Normalized PL and PLE spectra of $Ca_{6(1-x)}Eu_{6x}BaP_4O_{17}$ (x = 0.01, 0.05, 0.10, 0.20) are also exhibited in Fig. 4-5(b). All Eu^{2+}-doped phosphors showed the asymmetric emission bands from the green to the red region under blue light irradiation owing to the 5d - 4f allowed transition of the Eu^{2+} ion, implying that the Eu^{2+}-activated $Ca_6BaP_4O_{17}$ is suitable for the blue LED chip to generate pseudo white light. The emission and excitation spectra of $Ca_{5.94}Eu_{0.06}BaP_4O_{17}$ (x = 0.01) are similar to those in the previous report by Komuro et al.[132] However, PL and

PLE intensities drastically decrease as increasing the amount of Eu^{2+} ion. On the other hand, as the concentration of the Eu^{2+} ion increased, the excitation intensity in the blue region around 450 nm becomes slightly stronger than that in the ultraviolet region. Finally, the emission peak top of $Ca_{6(1-x)}Eu_{6x}BaP_4O_{17}$ is shifted to the longer wavelength from the green-yellow around 550 nm to the reddish orange at approximately 610 nm when the doping amount of the Eu^{2+} ion was varied from $x = 0.01$ to $x = 0.20$ (Fig. 4-5(c)). The photographs under ultraviolet light irradiation (λ_{ex} = 365 nm) and the chromaticity diagram of $Ca_{6(1-x)}Eu_{6x}BaP_4O_{17}$ (x = 0.01, 0.05, 0.10, 0.20) are shown in Fig. 4-5(d). The (X,Y) values of $Ca_{6(1-x)}Eu_{6x}BaP_4O_{17}$ are found to be (0.4460, 0.5058) (x = 0.01), (0.4710, 0.4855) (x = 0.05), (0.4955, 0.4638) (x = 0.10) and (0.5012, 0.4344) (x = 0.20), respectively. As the amount of the activator ion increases, Eu^{2+}-doped samples were gradually colored from pale to deep yellow. Moreover, the emission color shift from the green-yellow to the reddish-orange in Eu^{2+}-activated $Ca_6BaP_4O_{17}$ was also observed. Moreover, According to Henderson *et al.*, the crystal field strength of cation sites can be expressed by average bond length, as in the following equation (2):[79]

$$Dq \propto \frac{1}{R^5} \quad (2)$$

where Dq is crystal field strength and R means the average bond length of cation sites. This relationship indicates that the crystal field strength of a smaller site becomes stronger than that of a larger site. As a result, strong crystal field strength leads to a longer emission wavelength. In the case of $Ca_6BaP_4O_{17}$, the host lattice consists of three alkali earth sites to which emission center can substitute, CaO_7, CaO_8 and BaO_{12} respectively. As mentioned in the crystal structure section, the Eu^{2+} ions prefer to substitute for CaO_7 and CaO_8 sites rather than BaO_{12} sites, hence the focus is only on the two calcium sites. The average bond length of CaO_7 is 2.421 Å, while that of CaO_8 is 2.510 Å. Based on equation (1), CaO_7 has a stronger crystal field strength than that of the CaO_8 site. Moreover, Van Uitert proposed the theoretical formula for estimating the emission wavelength, equation (3):[140]

$$E = Q\left[1 - \left(\frac{V}{4}\right)^{1/V} 10^{-(n\,ea\,r)/80}\right] \quad (3)$$

where E is the emission energy, Q is the energy of free ions for Eu^{2+} (34,000 cm^{-1}), V is the valence of emission ions, n is the coordination number around emission ions, ea means electron affinity, and r is the ionic radius of substitution sites for emission ions. Based on equation (2), the estimated emission energies of Eu^{2+} in CaO_8 and CaO_7 are 17510.3 cm^{-1} (571.1 nm) and 16406.0 cm^{-1} (609.5 nm), respectively. These calculated emission energies are in agreement with the prediction from the crystal field strength. In addition, peak deconvolution of the asymmetric emission band in $Ca_{5.94}Eu_{0.06}BaP_4O_{17}$ (x = 0.01) was conducted (Fig. 4-6). The emission deconvolution is performed on an energy scale.[141] The calculated values from the peak deconvolution for the emission spectrum are listed in Table 4-4. As a result, the emission band was successfully fit by two components with λ_1= 18,797 cm^{-1} (532 nm) and λ_2 = 17,123 cm^{-1} (584 nm), corresponding to the Eu^{2+} ion located in CaO_7 and CaO_8, respectively. This means that the asymmetric emission spectra in the Eu^{2+}-doped $Ca_6BaP_4O_{17}$ are combined with the emission spectra of the Eu^{2+} ions located on two calcium sites.

Table 4-4 Result of the emission peak deconvolution of $Ca_{5.94}Eu_{0.06}BaP_4O_{17}$.

	Emission peak position (cm^{-1})	Emission peak position (nm)
Component 1	18,797	532
Component 2	17,123	584

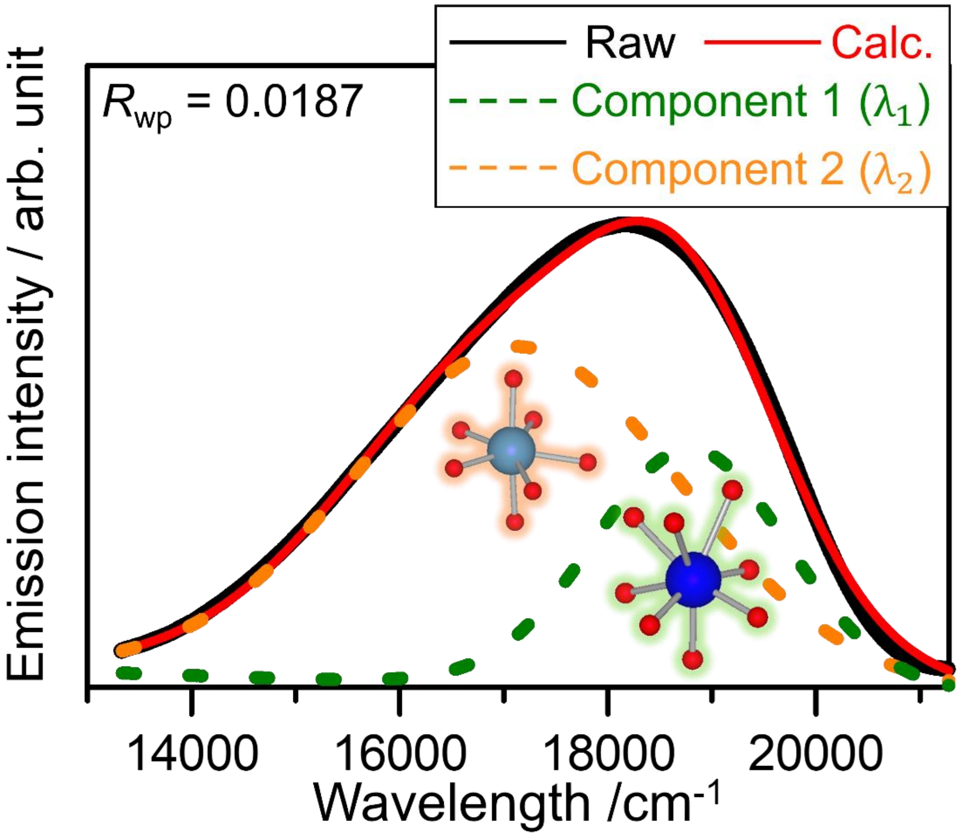

Fig. 4-6 Peak deconvolution of emission wavelength of $Ca_{5.94}Eu_{0.06}BaP_4O_{17}$ (x = 0.01).

4-3-5 Lifetime measurement

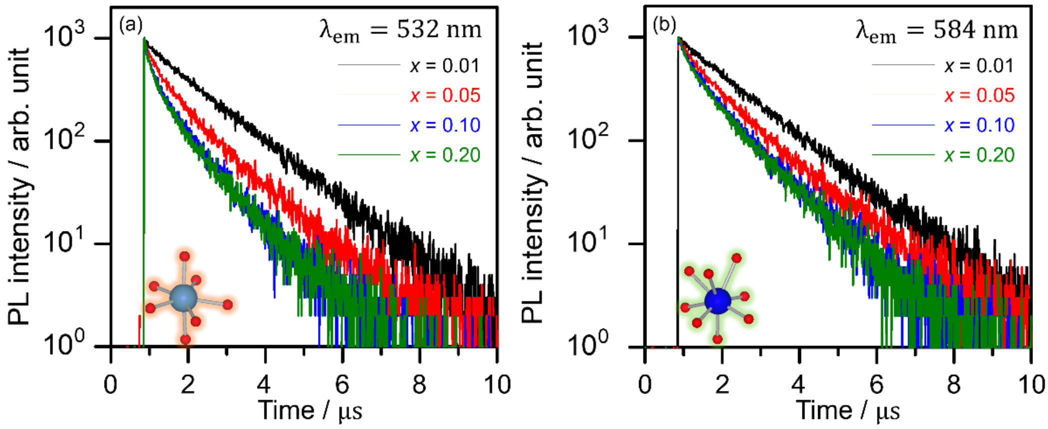

Fig. 4-7 Photoluminescence decay curves for $Ca_{6(1-x)}Eu_{6x}BaP_4O_{17}$ (x = 0.01, 0.05, 0.10, 0.20) monitored at (a) 532 nm, (b) 584 nm excited at 405 nm.

Fig. 4-7 shows the measurement of the lifetimes for Eu^{2+} at each emission wavelength (λ_1 = 532 nm, λ_2 = 584 nm) under λ_{ex} = 405 nm for $Ca_{6(1-x)}Eu_{6x}BaP_4O_{17}$ (x = 0.01, 0.05, 0.10, 0.20). The photoluminescence decay curve for each emission wavelength shows a linear shape on x = 0.01. As the concentration of the activator ion increases, the shape of the decay curves changes from linear to non-linear. Furthermore, we calculated the lifetime of the Eu^{2+} ion for $Ca_6BaP_4O_{17}$:Eu^{2+} with the following the integral equation (4):[82, 91, 142]

$$\tau = \frac{\int_0^\infty tI(t)t}{\int_0^\infty I(t)dt} \quad (4)$$

where τ is the average lifetime. Table 4-5 shows the variation of the lifetime of Eu^{2+} at each emission wavelength for $Ca_{6(1-x)}Eu_{6x}BaP_4O_{17}$ (x = 0.01, 0.05, 0.10, 0.20). All calculated lifetime values of the Eu^{2+} ion slightly decreased as the concentration of emission ion increased. In the $x = 0.20$ sample, the decay time at $\lambda_1 = 532$ nm is almost the same as that in the $x = 0.10$ sample, in contrast that at $\lambda_2 = 584$ nm, because it reveals that the incorporated Eu^{2+} ions in the CaO_8 site exhibit no difference between $x = 0.10$ and $x = 0.20$ samples in the Rietveld refinement. However, the overall lifetimes in the long emission region are higher than those in the short wavelength region. According to C. Liu *et al.*, the decay rates of the activators in the high emission energy region are faster than those in the low emission energy region owing to the energy transfer.[143] In the case of the Eu^{2+}-activated $Ca_6BaP_4O_{17}$, it seems that the Eu^{2+} ions occupied on the CaO_8 site give the energy to other Eu^{2+} ions.

Table 4-5 Calculated average lifetimes in $Ca_{6(1-x)}Eu_{6x}BaP_4O_{17}$ (x = 0, 0.01, 0.05, 0.10, 0.20) using the equation (5).

Sample	τ (532 nm) [μs]	τ (584 nm) [μs]
$x = 0.01$	1.463	1.487
$x = 0.05$	1.121	1.271
$x = 0.10$	0.868	1.053
$x = 0.20$	0.873	1.032

4-3-6 Thermal quenching behavior

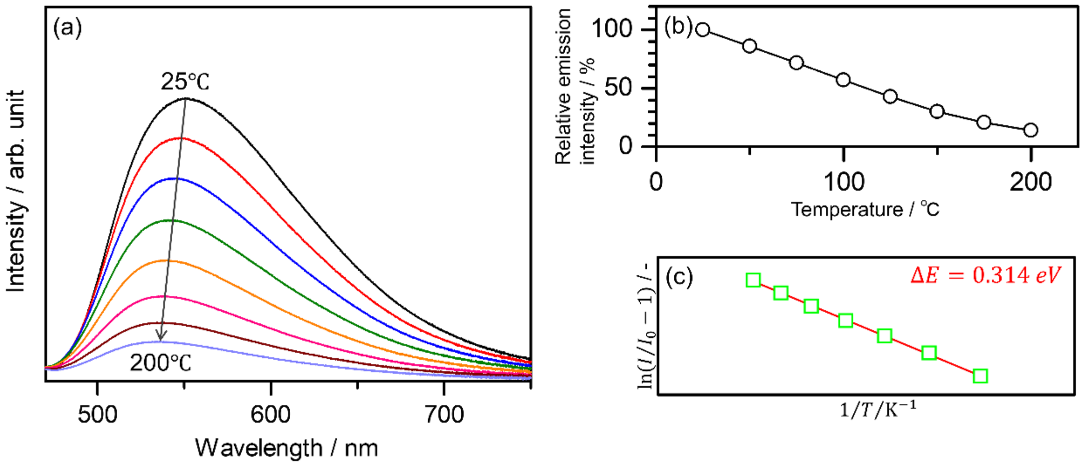

Fig. 4-8. (a) The emission spectrum of for $Ca_{5.94}Eu_{0.06}BaP_4O_{17}$ at each temperature (25℃ - 200℃), (b) the relative emission intensity depending on the temperature in $Ca_{5.94}Eu_{0.06}BaP_4O_{17}$ (x = 0.01) and (c) the linear fitting of the relationship of ln[(I_0/I_T)-1] vs. 1/ T.

Thermal durability at high temperatures is also important for Eu^{2+}-activated phosphors to be used wLEDs, because the junction temperature reaches approximately 150℃ in LED devices.[144] Fig. 4-8 implies the thermal dependence of $Ca_{5.94}Eu_{0.06}P_4O_{17}$ (x = 0.01). This green-yellow emitting phosphor shows a decreasing emission peak intensity and a blue shift as the temperature increases from room temperature (RT) to 200℃. As a result, from Fig. 4-8(b), the emission intensity of $Ca_{5.94}Eu_{0.06}BaP_4O_{17}$ keeps 14% at 200℃, indicating that the thermal quenching behavior of $Ca_{5.94}Eu_{0.06}BaP_4O_{17}$ is similar to that first proposed by Komuro et al. The thermal quenching in $Ca_{5.94}Eu_{0.06}BaP_4O_{17}$ occurs quickly than in Eu^{2+}-activated phosphate phosphors (e.g. $NaMgPO_4:Eu^{2+}$, $Sr_8MgLn(PO_4)_7:Eu^{2+}$ (Ln = Y^{3+}, La^{3+}) and $Na_3Sc_2(PO_4)_3:Eu^{2+}$).[64, 145, 146] Moreover, the asymmetric emission band of $Ca_{5.94}Eu_{0.06}BaP_4O_{17}$ occurs in a blue-shift from yellow to green color region as the temperature increases from RT. (Fig. 4-8(a)). The thermal stability of phosphor materials has typically been discussed in terms of an activation energy $\varDelta E$ (eV), and calculated by the following equation (5):[147-149]

$$\ln\left(\frac{I_0}{I_T}-1\right)=\ln c-\frac{\varDelta E}{kT} \qquad (5)$$

where I_0 and I_T are the initial emission intensities of the phosphor at RT and the temperature T, c is a constant, $\varDelta E$ is the activation energy of thermal quenching, and *k* is the Boltzman constant (8.62×10^{-5} eV). The plots of ln [(I_0/I_T)-1] versus 1/(kT) for $Ca_{5.94}Eu_{0.06}BaP_4O_{17}$ are illustrated in the insert of Fig. 4-8(c). The value of $\varDelta E$ in $Ca_{5.94}Eu_{0.06}BaP_4O_{17}$ is 0.314 eV, as calculated by the equation (3). In the previous report, J. Ueda *et al*. proposed that the activation energy of YAG:Ce^{3+} is 0.77 eV.[150] Thus, the thermal stability of $Ca_{5.94}Eu_{0.06}BaP_4O_{17}$ is lower than that of YAG:Ce^{3+}.

4-3-7 Fabrication of prototype wLEDs

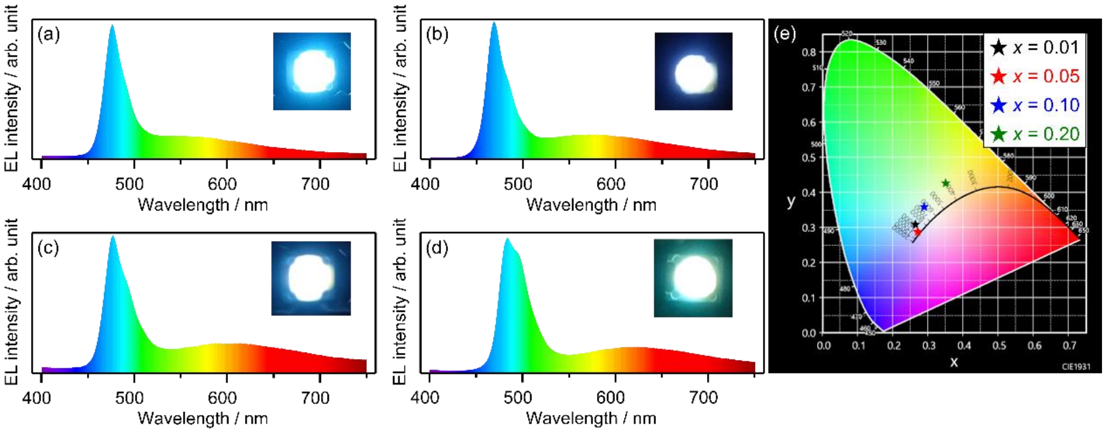

Fig. 4-9 Electroluminescence (EL) spectrum of the fabricated prototype based on the blue LED (InGaN) and (a) $x = 0.01$, (b) $x = 0.05$, (c) $x = 0.10$, (d) $x = 0.20$ and (e) the chromaticity diagram of the fabricated wLEDs.

Table 4-6 (X, Y) coordination of prototype wLEDs based on blue LED and $\mathrm{Ca}_{6(1-x)}\mathrm{Eu}_{6x}\mathrm{BaP}_4\mathrm{O}_{17}$ (x = 0.01, 0.05, 0.10, 0.20).

	X	Y
$x = 0.01$	0.2640	0.3080
$x = 0.05$	0.2700	0.2870
$x = 0.10$	0.2890	0.3580
$x = 0.20$	0.3500	0.4260

The electroluminescent spectrum of the fabricated prototype wLEDs based on the blue LED and $\mathrm{Ca}_{6(1-x)}\mathrm{Eu}_{6x}\mathrm{BaP}_4\mathrm{O}_{17}$ ($x = 0.01, 0.05, 0.10, 0.20$) under 30 mA current is shown in Fig. 4-9(a)-(d). The sharp blue emission due to the blue LED chip and the broad reddish-orange emission spectrum approximately centered at 600 nm owing to the Eu^{2+}-activated $\mathrm{Ca}_6\mathrm{BaP}_4\mathrm{O}_{17}$ phosphor are clearly observed.

Therefore, pseudo-white light is successfully obtained by combining the blue LED and the Eu^{2+}-activated $Ca_6BaP_4O_{17}$:Eu^{2+} phosphor (inset photograph of Fig. 4-9(a)-(d))) is the CIE chromaticity diagram of the fabricated prototype wLEDs. The coordination (*X*, *Y*) values of the prototype wLEDs module are listed on Table 4-6. The (*X*,*Y*) values are found to be (0.2640, 0.3080) (x = 0.01), (0.2700, 0.2870) (x = 0.05), (0.2890, 0.3580) (x = 0.10) and (0.3500, 0.4260) (x = 0.20), respectively. As a result, all prototype wLEDs show the pseudo-white emission. This is because wLEDs fabrication using Eu^{2+}-activated $Ca_6BaP_4O_{17}$ has not been optimized yet in terms of amount of phosphor powder. Consequently, adjusting the doping amount of Eu^{2+}-activated $Ca_6BaP_4O_{17}$ is a promising method for developing luminescent materials for optical devices, especially phosphor-converted LEDs.

4-4 Conclusion

Color-tunable phosphate phosphors, $Ca_{6(1-x)}Eu_{6x}BaP_4O_{17}$ (x = 0, 0.01, 0.05, 0.10, 0.20) were synthesized by the conventional solid-state reaction as a main phase. As the amount of Eu^{2+} increased, the emission color of $Ca_6BaP_4O_{17}$:Eu^{2+} showed a red-shift from green-yellow to red emission with a peak top of emission band at 611 nm. Rietveld refinement showed that the lattice volume of the $Ca_6BaP_4O_{17}$ host is expanded corresponding to the concentration of the emission ion because Eu^{2+} predominantly occupied two Ca sites, CaO_7 and CaO_8. This caused the red-shift of the emission bands in $Ca_6BaP_4O_{17}$:Eu^{2+} to occur. Moreover, the Eu^{2+} decay time implies that the energy migrated among Eu^{2+} ions. The emission intensity exhibited by the Eu^{2+}-$Ca_6BaP_4O_{17}$ phosphor was 14% at 200℃. The fabricated prototype wLEDs exhibit the warm white light emission. Incorporation of a high amount of the emission ion with the 4f - 5d allowed transition is a promising method for developing red-emitting oxide phosphors.

Chapter 5.

Determination of layer crystal structure $Sr_2Ba_2(PO_4)_2O:Eu^{2+}$ by Melt Quenching Technique

5-1 Introduction

Most of Eu^{2+}- or Ce^{3+}-activated phosphors are obtained by the conventional solid-state reaction under the reductive atmosphere. However, this synthetic method is difficult for the metastable crystal structure, which is stabilized in a specific temperature region, because samples become the stable crystal structure during the cooling process. To obtain the metastable crystal structures, the melt quenching method using the arc-imaging furnace is a useful technique. **Fig. 5-1**(a) shows the schematic diagram of the melt quenching furnace in our laboratory.

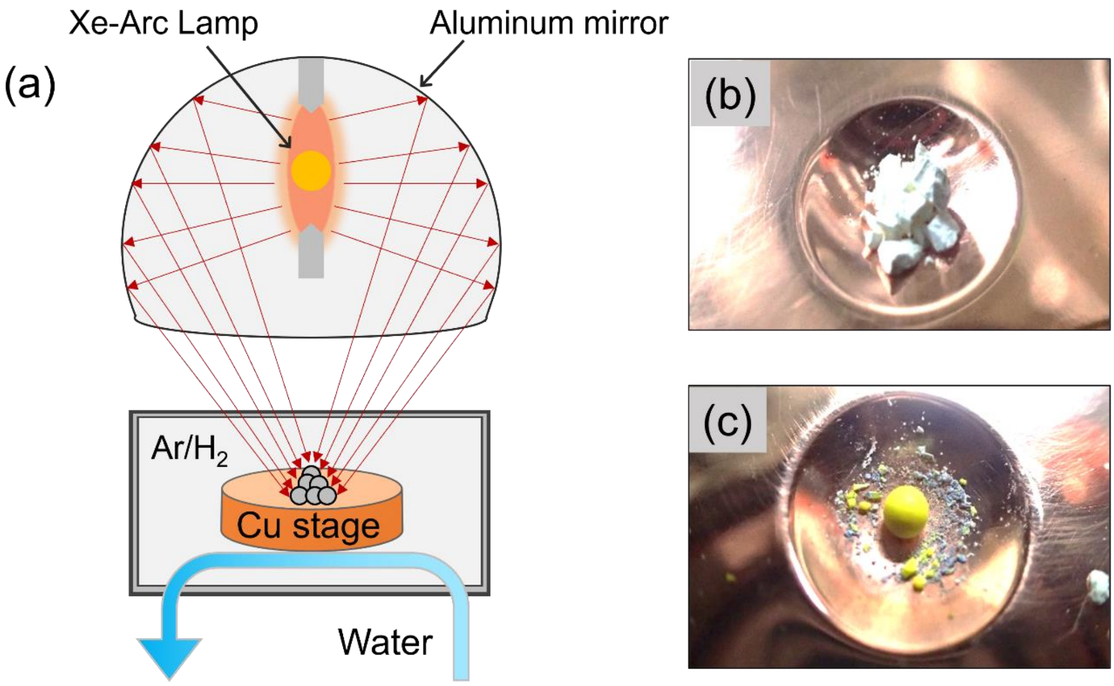

Fig. 5-1 (a) Schematic diagram of melt quenching furnace and photographs of (b) before and (c) after calcined YAG:Ce^{3+} sample.

The Xe-Arc lamp emits high energy light, which is reflected by an ellipsoidal aluminum mirror. The reflected light is simultaneously condensed on a Cu sample stage. The samples can be rapidly calcined at over 2000℃ and cooled by removing the cu stage from the focus with cooling rate at approximately $100℃/s$. In addition, the reductive gas can be injected into the sample chamber, therefore the atmosphere control is easily treated. Fig. 5-1(b) and (c) show the photographs of before and after calcined the YAG:Ce^{3+} sample by melt quenching furnace. Heated sample forms spontaneously the ball shape. The previous works related to the arc imaging furnace in our laboratory are listed on Table 5-1. Over the past a decade, functional inorganic ceramics have been developed by the melt quenching technique.

Table 5-1 Previous works of the inorganic compounds synthesized by Melt quenching technique

Samples	Ref.
$NaMgPO_4$:Eu^{2+} (Olivine)	67, 146
$SrAl_2O_4$:Eu^{2+}, Dy^{3+}	151
$BaCa_2Y_6O_{12}$:Ce^{3+}	152
$Ba_9Sc_2Si_6O_{24}$:Eu^{2+}	153
$M_3MgSi_2O_8$:Eu^{2+} (M = Ca, Sr, Ba)	154
$CaLaGaO_4$:Eu^{3+}	155
$Ba_3Sc_4O_9$:Ho^{3+}	156
Y_2O_3:Eu^{3+}	157
$MLaAlO_4$:Eu^{3+} (M = Ca, Sr, Ba)	157
$Sr_4ScAl_3O_{10}$:Eu^{2+}	158
La_2WO_6:Eu^{3+}	159

In Chapter 5, we focus on the development of metastable phosphate luminescent materials. Many Eu^{2+}-activated phosphates have been investigated as phosphors for optical devices such as PDPs and LEDs. Recent years, $M_4(PO_4)_2O$:Eu^{2+} (M = Ca, Sr) have been developed and showed the near infrared emission under the blue light excitation, indicating that the $M_4(PO_4)_2$:Eu^{2+} phosphors can convert into the wavelength which is suitable for c-Si solar cells. [139, 160] However, The solid solution system among $(Ca,Ba,Sr)_4(PO_4)_2O$:Eu^{2+} has not been hitherto investigated, thus the novel crystal phase in the $(Ca,Ba,Sr)_4(PO_4)_2O$:Eu^{2+} solid solution system can be expectably obtained. As a result of the combinatorial synthesis using the melt quenching furnace, yellow emitting $Sr_2Ba_2(PO_4)_2$:Eu^{2+} phosphor was successfully obtained. Moreover, its single crystals are also collected in the sample and analyzed. The crystal structure of $Sr_2Ba_2(PO_4)_2$:Eu^{2+} contains layered blocks with Sr and Ba. The refined crystal structure and luminescent properties are greatly different from reported $M_4(PO_4)_2O$:Eu^{2+}.

5-2 Material Procedure

5-2-1 Material Synthesis

$SrCO_3$, $BaCO_3$, $NH_4H_2PO_4$ and Eu_2O_3 were weighed in a stoichiometric ratio at Ba : Sr : P : Eu = 2 : 2(1-x) : 2 : 2x ($0 \leq x \leq 0.60$). Afterwards, they were mixed in an acetone solution using an agate mortar to obtain homogeneous mixtures. Then, they were placed on an alumina boat and preheated at 400℃ for 2 h under ambient air to remove NH_3 and H_2O. The calcined samples were calcined to form fine powders and replaced on the copper sample stage. The copper sample stage was mounted on a horizontal water-cooled stand in a chamber filles with reduction gas (5 vol. % H_2, 95 vol. % Ar). After that, the samples were melted by theradiation of the 6 kW Xe arc lamp for about 10 s. The molten phosphor balls were obtained by removing the stage from the focus of the mirror. The balls were crushed into the fine ceramic powder to conduct the further characterization.

5-2-2 Characterization

The single crystals were collected using a polarizing microscope with the high power near ultraviolet LEDs at 365 nm. Single crystal is placed on a glass capillary. The single crystal analysis was conducted by single X-ray diffraction (XtaLAB mini, Rigaku). Data collection and cell refinement were output by the *Crystal Clear-SM Auto 2.0 rl* (Rigaku, 2010). After the measurement, structural analysis was performed by *WinGX* software.[161] An initial structure model of the polymorph was obtained by a direct method using *SIR2008*.[162] The structural parameters of the single crystals were refined using the *SHELXL2014* program. [163] Powder X-ray Diffraction (XRD) data were collected by an X-ray diffractometer

(Miniflex; Rigaku Co., Ltd.) with a monochromatic Cu$K\alpha$ (λ = 1.54056 Å) under 10 mA and 30 kV. Photoluminescence (PL) and photoluminescence excitation (PLE) spectra, thermal quenching PL, internal and external quantum efficiency were measured by a spectrofluorometer. (FP-6500/FP-6600; Jasco, Inc.) with a 150 W Xenon lamp.

5-3 Result and discussion

5-3-1 Crystal structure determination

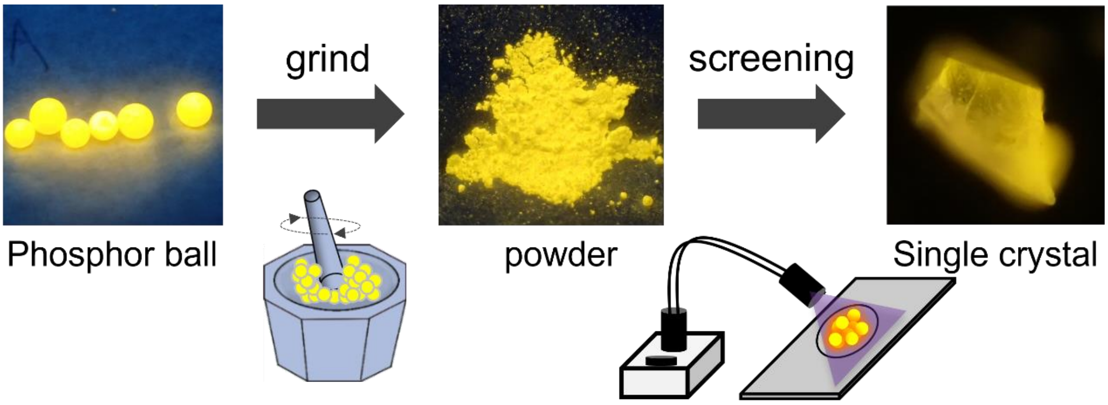

Fig. 5-2 Scheme of single crystal screening in this study. All photographs are took under 365 nm excitation.

The melt quenched samples form the ball shape and show the strong yellow emission under 365 nm excitation (Fig. 5-2; right). Then, after crushing the phosphor balls, fine powders are also obtained. (Fig. 5-2; middle). Then, the single crystals are screened from the powder samples. Single crystals show also yellow emission and crystal color is colorless. Afterwards, the single crystals are mounted on glass capillary and analyzed. The refined crystallographic data and structure refinement results of the single crystal obtained by the melt quenching method are shown in Table 5-2. The chemical formula of single crystal is refined as $Sr_{1.88}Eu_{0.12}Ba_2P_2O_9$. The obtained $Sr_{1.88}Eu_{0.12}Ba_2P_2O_9$ (SBPO:0.12Eu^{2+}) forms the orthorhombic crystal structure with *Cmce* (No. 64). The lattice parameters are found to be a = 18.408(4) Å, b = 7.0971(16) Å, c = 7.1420(16) Å and V = 933.1(4) Å^3, respectively. The $R[F^2 > 2\sigma(F^2)]$ and $wR(F^2)$ values are finally converged to 0.0338 and 0.0631.

Table 5-2 Crystallographic Data and Parameters for the structural determination of obtained single crystal by the melt quenching technique.

formula	$Sr_{1.88}Eu_{0.12}Ba_2P_2O_9$ (SBPO:0.12Eu^{2+})
formula mass (g/mol)	663.56
Crystal color, Habit	colorless, prism
crystal system	orthorhombic
space group	*Cmce* (No. 64)
cell parameters (Å)	*a* = 18.408(4), *b* = 7.0971(16), *c* = 7.1420(16)
volume ($Å^3$)	933.1(4)
density (g/cm^3)	4.723
Z (-)	4
crystal size (mm^3)	0.079 x 0.074 x 0.070
temperature (℃)	20
diffractometer	Rigaku XtaLab mini
Absorption correction	Multi-scan (*REQAB:* Rigaku, 1998)
radiation type	MoK_α (0.71075 Å) Graphite monochromated
μ (mm^{-1})	20.16
$2\theta_{\mathrm{max}}$ (degree)	54.9
measured reflections	4173
independent reflections	554
observed reflections	409
R_{int}	0.0750
$R[F^2 > 2\sigma(F^2)]$, $wR(F^2)$	0.0338, 0.0631
$\Delta\rho_{\mathrm{max}}, \Delta\rho_{min}$ ($e/Å^3$)	0.82, -0.83
Goodness of fit	1.178

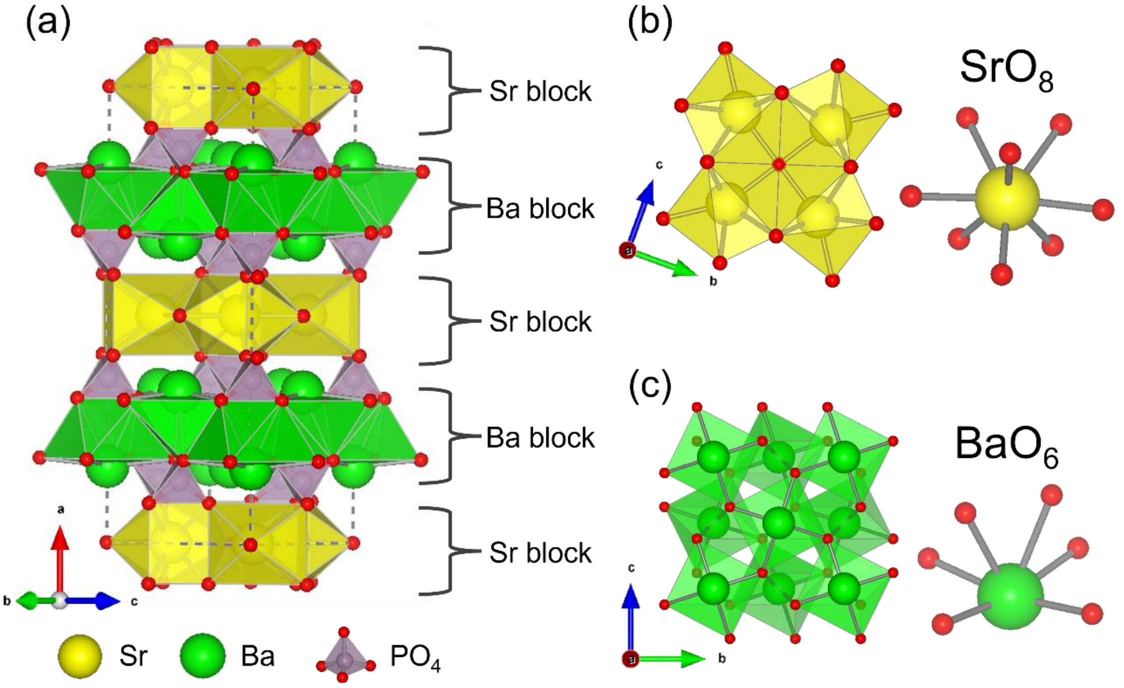

Fig. 5-3(a) Refined crystal structure of SBPO:0.12Eu^{2+}, (without Sr split site for clarity) (b) Sr and (a) Ba blocks. All images are illustrated by the VESTA program.

Table 5-3 Atomic coordination and isotropic atomic displacement parameters of SBPO:0.12Eu^{2+}.

atom	occ	x	y	z	*U*
Ba1	1	0.16752(3)	1.5	0.5	0.0243
Sr1	0.8893	0	1.30377(13)	0.80213(13)	0.0213
Eu1	0.0591	0	1.30377(13)	0.80213(13)	0.0213
Sr2	0.0516	0	1.206(4)	0.697(4)	0.046
P1	1	0.13807(14)	1.5	1	0.0209
O1	1	0	1.5	0.5	0.071
O2	1	0.1841(4)	1.3748(9)	0.8802(9)	0.0703
O3	1	0.0882(3)	1.3797(11)	1.1217(12)	0.0786

Fig. 5-3(a) describes the refined crystal structure of SBPO:0.12Eu^{2+} without Sr split site for clarity illustrated by the VESTA program.[77] The atomic coordinates and equivalent isotropic displacement parameters of SBPO:0.12Eu^{2+} are also listed on Table 5-3. The SBPO:0.12Eu^{2+} forms the layered like crystal structure, which consists of Sr and Ba blocks. Fig. 5-3(a) and (b) illustrate each alkali block and polyhedral. The Sr block is composed of eight-fold coordination of Sr, SrO_8, while the Ba block is BaO_6. Moreover, the refined crystal structure of SBPO:0.12Eu^{2+} consists of one Sr split site. This Sr split site also forms SrO_8 and the polyhedral block. The Sr split site is located on the slightly deviated position maybe because the stacking fault occurs during the melt quenching synthesis. From the single crystal analysis of SBPO:0.12Eu^{2+}, the Eu^{2+} ion is occupied on only SrO_8 site.

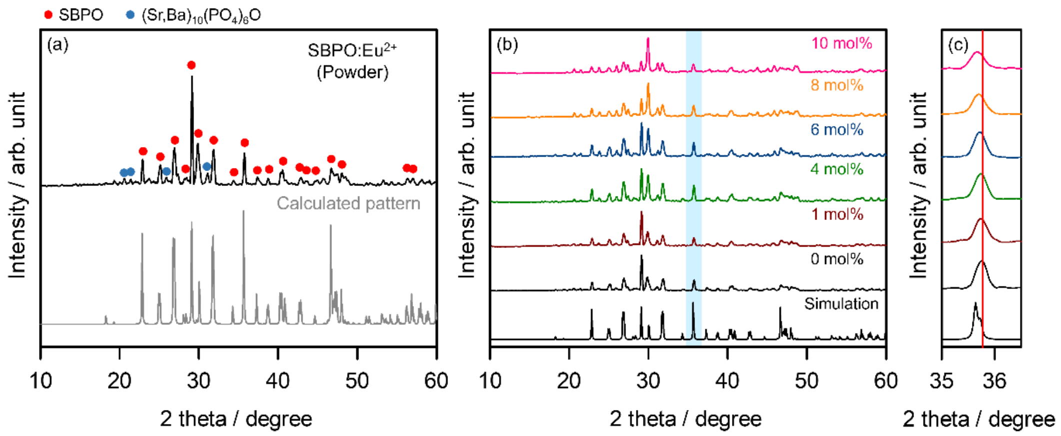

Fig. 5-4(a) powder XRD pattern of SBPO:Eu^{2+} and (b) all samples. (c) Enlarged view of the powder XRD pattern around 36°.

Fig. 5-4(a) shows the powder XRD pattern of SBPO:Eu^{2+} and calculated simulation pattern. Although the diffraction intensity ratio is different from the calculation pattern, the diffraction position of SBPO:0.12Eu^{2+} powder sample is in good agreement with the simulation, including the apatite as an impurity phase. Fig. 5-4(b) also shows the powder XRD patterns of SBPO:xEu^{2+} ($0 \leq x \leq 0.60$). The diffraction pattern of SBPO is appeared in all samples, while $(Sr,Ba)_{10}(PO_4)_6O$ is also obtained. Moreover, the enlarged view of the powder XRD pattern around 36° is exhibited to determine the peak shift by doping Eu^{2+} ion. As increasing the amount of Eu^{2+} ion, the diffraction peak around 36° is moved to lower-angle position.

5-3-2 Photoluminescence properties

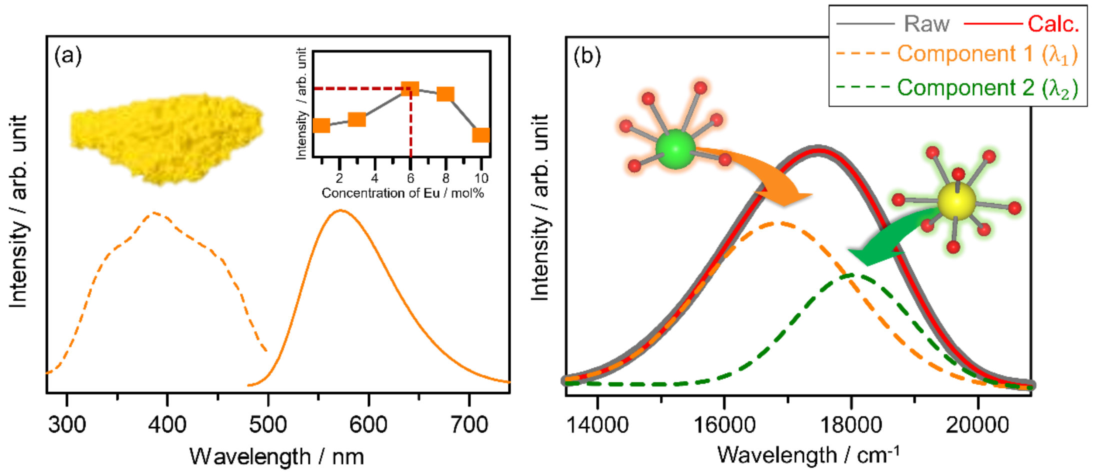

Fig. 5-5(a) Excitation and emission spectra of SBPO:0.12Eu2+. Insert photograph shows emitting SBPO:0.12Eu2+ under 365 nm excitation and figure is the concentration dependence of excitation and emission intensities. (b) Emission peak deconvolution of SBPO:0.12Eu^{2+}.

Fig. 5-5(a) shows the excitation and emission spectra of SBPO:0.12Eu^{2+}. An insert photograph of Fig. 5-5(a) shows emitting SBPO:0.12Eu^{2+} under 365 nm excitation. The asymmetric emission band at approximately 580 nm peak top under the near ultraviolet light excitation around 390 nm. SBPO:Eu^{2+} yellow phosphor is appliable for near ultraviolet LEDs. As above mentioned, all samples includes the oxyapatite crystal structure, $(Sr,Ba)_{10}P_6O_{25}$. We carried out the synthesis of $Sr_5Ba_5(PO_4)_6O$:Eu^{2+} by the same experimental condition. However, the blue emission is only observed under the near ultraviolet light excitation. Moreover, as increasing the amount of Eu^{2+} ion in the synthesis of SBPO:Eu^{2+}, the blue emission is not obtained in all samples. From these viewpoints, the apatite phase can be ignored in the further discussion. Insert figure of Fig. 5-5(a) is the concentration dependence of the excitation and emission intensities of SBPO:Eu^{2+}. Until 6 mol%, both excitation and emission intensities of SBPO:Eu^{2+} are enhanced. Meanwhile, they drastically decrease beyond 6 mol%, thus the optimal concentration of Eu^{2+} ion in SBPO determines 6 mol% in this work. The asymmetric emission band of SBPO:0.12Eu^{2+} can be deconvoluted into two emission components and is shown in Fig. 5-5(b). The emission band of SBPO:0.12Eu^{2+} consists of component 1 (16849 cm^{-1}; 594 nm) and 2 (18035 cm^{-1}; 554 nm), respectively. SBPO crystal structure has two substitutional sites for Eu^{2+} ion, SrO_8 and BaO_6. The empirical model suggested by P. Dorenbos and L. G. V. Unitert is adopted to identify the substitutional site of Eu^{2+} ion. The crystal field splitting (D_q) can be explained following the equation (1):[164]

$$\varepsilon_{cfs} = \beta_{poly}^{Q} R_{av}^{-2} \quad (1)$$

where β_{poly}^{Q} shows a constant depending on the shape and coordination number. β_{poly}^{Q} is estimated to be 1.35×10^9 pm^2 cm^{-1} (octahedra; six-fold coordination), 1.20×10^9 pm^2 cm^{-1} (cubal; eight-fold coordination) and 5.67×10^8 pm^2 cm^{-1} (cubo; twelve-fold coordination), respectively. This equation indicates that the crystal field splitting of the octahedral site is the strongest of sites with high coordination number. In the case of SBPO, the coordination number of Sr is eight, which is higher than that of Ba, thus the crystal field splitting of BaO_6 is stronger than that of SrO_8. On the other hand, the emission energy estimation can be found by the Uitert empirical model following the equation (2):[140]

$$E = Q\left[1 - \left(\frac{V}{4}\right)^{1/V} 10^{-(n\, ea\, r)/80}\right] \quad (2)$$

where E is the emission energy, Q is the energy of free ions for Eu^{2+} (34,000 cm^{-1}), V is the valence of emission ions, n is the coordination number around emission ions, ea means electron affinity, and r is the ionic radius of substitution sites for emission ions. The emission energy of SrO_8 and BaO_6 are found to be 18269 cm^{-1} (547 nm) and 16902 cm^{-1} (592 nm), respectively. Based on the results, the asymmetric emission band of SBPO:Eu^{2+} has two components of Eu^{2+} ions located on two different crystallographic sites, SrO_8 and BaO_6.

5-3-3 Thermal quenching properties

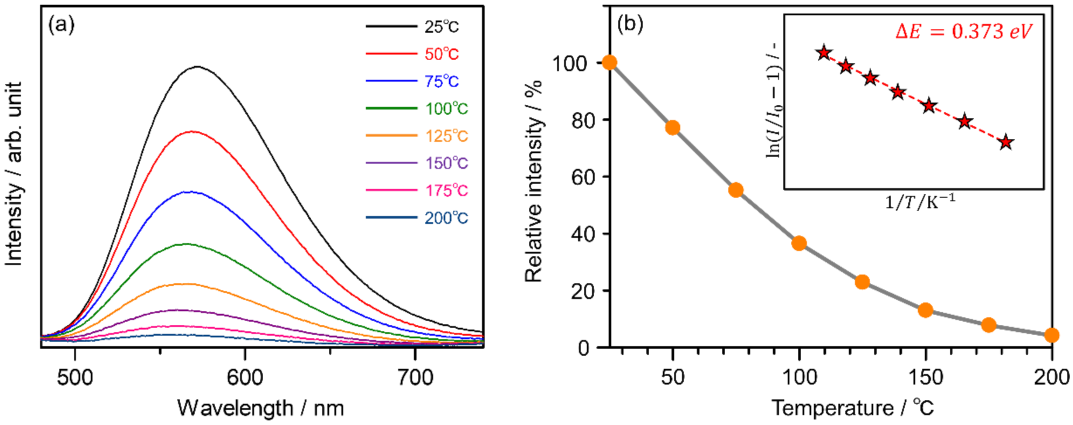

Fig. 5-6(a) Emission spectra of SBPO:0.12Eu^{2+} at each temperature excited at 387 nm and (b) temperature dependence of relative intensity for SBPO:0.12Eu^{2+}. Insert figure shows the Arrhenius plot.

The temperature dependence of the emission intensities for SBPO:0.12Eu^{2+} is described in Fig. 5-6. As the temperature rises from 25℃ to 200℃, the emission blue shift is observed. The emission peak position of 574 nm at 25℃ is shifted to 558 nm at 200℃. Moreover, the relative emission intensity at 200℃ maintains 4% compared with that of 25℃ (Fig. 5-6(b)). On the other hand, the thermal activation energy ($\varDelta E$) is also calculated using the equation (3):[149, 165-167]

$$\ln\left(\frac{I_0}{I_T}-1\right)=\ln c-\frac{\varDelta E}{kT}\qquad(3)$$

where I_0 is the emission intensity at room temperature, I_T is the emission intensity at temperature T, $\varDelta E$ is the activation energy of thermal quenching, and k is the Boltzmann constant (8.62×10^{-5} eV). The plots of ln [(I_0/I_T)-1] versus

$1 / (kT)$ for SBPO:0.12Eu^{2+} is illustrated in insert figure of Figs. 5-6(b) As a result, the activation energy of SBPO:0.12Eu^{2+} is found to be 0.373 eV.

5-4 Conclusion

Eu^{2+}-activated yellow emitting $Sr_2Ba_2(PO_4)_2O$ (SBPO) phosphors is successfully obtained by melt quenching method. From the single crystal analysis, the layer crystal structure with Sr and Ba blocks is formed in SBPO. Powder XRD pattern of SBPO:Eu^{2+} includes the apatite phase as the impurity phase. Eu^{2+}-activated SBPO shows the yellow emission at approximately 580 nm under the near ultraviolet light excitation around 380 nm. The emission peak deconvolution, emission energy estimation using empirical models indicate that the emission band of SBPO:Eu^{2+} is due to the substitution of Eu^{2+} ion for SrO_8 and BaO_6. The thermal quenching properties of SBPO:Eu^{2+} is poor, which the relative emission intensity keeps 4% at 200℃ in comparison with that at 25℃. The melt quenching technique is allowed to develop the novel soluble system that has not been synthesized.

Chapter 6.

Structure and Luminescence studies of Ce^{3+}-activated $Ba_5La_3MgAl_3O_{15}$ Green Emitting Phosphor

6-1 Introduction

A garnet crystal structure with $A_3B_2C_3O_{12}$ chemical formula is widely researched for phosphor host material of Ce^{3+} ion.[168, 169] In garnet crystal structure, *A* forms a square antiprism with eight oxygen atoms, *B* shows an octahedral field and *C* shows a tetrahedra. Ce^{3+} ion normally substitutes for *A* site and shows the bright emission from cyan to orange regions under the blue light excitation. Over the past a decade, many Ce^{3+}-activated novel garnet phosphors have been developed and researched for next-generation lighting system such as laser diodes.[170-180] However, in most Ce^{3+}-activated garnet phosphors, their absorption efficiency in near ultraviolet light around 400 nm, which is approximate emission peak of near ultraviolet LEDs, is poor, while the longer wavelength excitation near blue region is highly effective. Moreover, since optical properties of Ce^{3+} ion are strongly depending on the host material due to the 5d - 4f transition, exploration of Ce^{3+}-activated phosphors with garnet crystal structure limits to develop highly near ultraviolet light excitable phosphors. Therefore, novel crystal structures are desired for Ce^{3+} instead of garnet structure to obtain near ultraviolet light excitable phosphors.

In this work, Ce^{3+}-activated $Ba_5LaMgAl_3O_{15}$ (BLMAO) with $Ba_6La_2Al_{1.5}Fe_{2.5}O_{15}$ crystal structure is successfully obtained. The crystal structure of $Ba_6La_2Al_{1.5}Fe_{2.5}O_{15}$ was firstly reported by I. Rütter *et al.*[181] Moreover, Similar crystal structures such as $Ba_6La_2Fe_4O_{15}$ and $Ba_6La_2Ga_4O_{15}$ show magnetic properties of the spin tetramer.[182] Although many kinds of materials with $Ba_6La_2Al_{1.5}Fe_{2.5}O_{15}$ crystal structure had been synthesized during 1990s, Ce^{3+}-activated phosphors with $Ba_6La_2Al_{1.5}Fe_{2.5}O_{15}$ crystal structure has not been hitherto developed probably because almost crystal structures consist of transition metals such as Fe^{3+} and Co^{3+} that act as killer ions for Eu^{2+} and Ce^{3+}.[183-185] Therefore, Mg^{2+} is replaced to transition metal in $Ba_6La_2Al_{1.5}Fe_{2.5}O_{15}$ to develop the novel phosphor host for Ce^{3+}. Moreover, the chemical formula is optimized to compensate the charge imbalance between Fe^{3+} and Mg^{2+}. Consequently, $Ba_5La_3MgAl_3O_{15}$ with the isolated Mg^{2+} octahedra instead of transition metal can be obtained. Ce^{3+}-doped BLMAO shows the broad green emission peaked around 508 nm under 412 nm excitation with 4,202 cm^{-1} stokes shift, which is attributed to the 5d - 4f transition of Ce^{3+}. From results in emission peak deconvolution of BLMAO:Ce^{3+} and empirical Dorenbos model, Ce^{3+} preferably occupies on two different crystallographic sites, BaO_6 and $(Ba/La)O_8$. Here, the Rietveld refinement, photoluminescence, quantum efficiencies, emission decay curves and thermal quenching behavior are researched to evaluate the potential of BLMAO:Ce^{3+} for pc-wLEDs.

6-2 EXPERIMENTAL SECTION

6-2-1 Material synthesis

The green-emitting phosphors of $Ba_5La_{3(1-x)}MgAl_3O_{15}$:3xCe^{3+} (BLMAO:3$x$Ce^{3+}; x = 0, 0.005, 0.01, 0.02, 0.03, 0.04, 0.05, 0.06, 0.07) were synthesized by a conventional solid state reaction. $BaCO_3$ (Kanto Chemical, Co., Inc., 99.9%), La_2O_3 (Sigma-Aldrich, 99.99%), MgO (Kanto Chemical, Co., Inc., 99.99%), Al_2O_3 (Koujundo Chemical, Co., Inc., 99.9%) and CeO_2 (Kanto Chemical, Co., Inc., 99.99%) were prepared as raw materials and weighed in a stoichiometric ratio. Then, we mixed these starting powders in an acetone solution using an agate mortar. Afterwards, the homogeneous mixtures were pre heated at 1500℃ for 6 h in a box furnace under an ambient atmosphere. Then, calcined materials were grounded. The grounded precursors were annealed at 1400℃ for 6 h under a reductive atmosphere to reduce the valence of Ce from tetravalent to trivalent.

6-2-2 Characterization

Powder X-ray Diffraction (XRD) data were collected by an X-ray diffractometer (D2 PHASER, Bruker Co., Ltd.) with a monochromatic CuK_α (λ = 1.54056 Å) under 10 mA and 30 kV. Rietveld refinement was conducted using RIETAN-FP software. [186] Photoluminescence (PL) and photoluminescence excitation (PLE) spectra, thermal quenching PL, internal and external quantum efficiency were measured by a spectrofluorometer. (FP-6500/FP-6600, Jasco, Inc.) with a 150 W Xenon lamp. The PL decay curves of emission from Ce^{3+} in BLMAO:3xCe^{3+} were monitored by a Quantaurus-Tau (Hamamatsu Photonics, Inc.).

6-3 Result and Discussion

6-3-1 Crystal structure determination

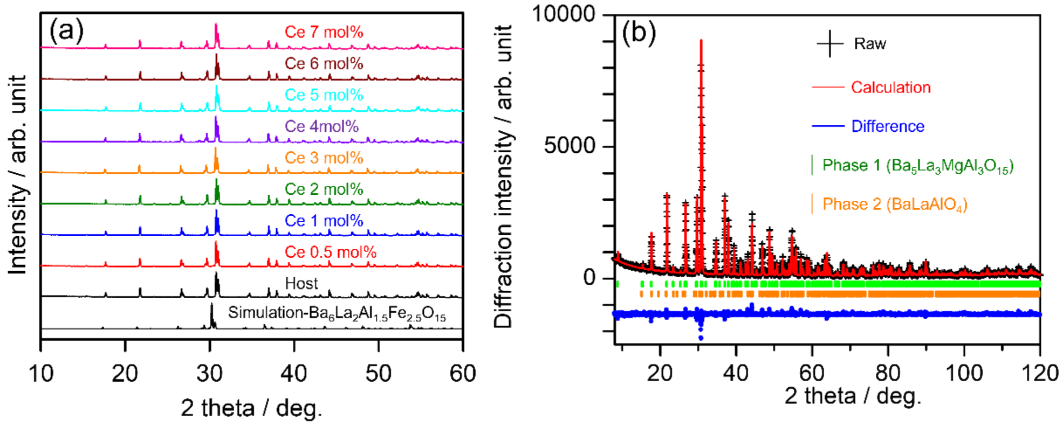

Fig. 6-1(a) XRD patterns of BLMAO:3xCe^{3+} (x = 0, 0.005, 0.01, 0.02, 0.03, 0.04, 0.05, 0.06, 0.07) and (b) Rietveld refinement for BLMAO host (+ symbol means raw data, red line is calculation patterns, blue line shows the difference between raw and calculation, green vertical line is Bragg position of BLMAO and orange line is an impurity, BaLaAlO$_4$.)

Fig. 6-1(a) shows XRD diffraction patterns of BLMAO:3xCe^{3+} and simulation pattern of Ba$_6$La$_2$Al$_{1.5}$Fe$_{2.5}$O$_{15}$ because the crystal structure of BLMAO has not been reported. Diffraction peaks of BLMAO:3xCe^{3+} are moved to higher angle than those of Ba$_6$La$_2$Al$_{1.5}$Fe$_{2.5}$O$_{15}$. The Rietveld refinement for all products is conducted to identify the crystal structure. Since the crystal structure of BLMAO has not been reported, the crystallographic coordination data of Ba$_6$La$_2$Al$_{1.5}$Fe$_{2.5}$O$_{15}$, which is the prototype for BLMAO, is adopted as s model structure in the Rietveld refinement. Fig. 6-1(b) shows the Rietveld refinement for BLMAO. The crystallographic data of BLMAO and the refined parameters of all

BLMAO:3xCe^{3+} (x = 0, 0.005, 0.01, 0.02, 0.03, 0.04, 0.05, 0.06 and 0.07) are summarized in Table 6-1 and Table 6-2. The lattice parameters of BLMAO are found to be a = 11.6745(2) Å, c = 7.0635(1) Å, V = 833.73(2) Å^3, in a hexagonal system with space group of $P6_3mc$ (No. 186). All isotropic displacement parameters (B_{eq}) are fixed to 1.0. The R-values are converged to R_{wp} = 8.637%, R_p = 6.755%, R_e = 5.902% and S = 1.463, indicating that the BLMAO is in good agreement with the $Ba_6La_2Al_{1.5}Fe_{2.5}O_{15}$ structure. On the other hand, $BaLaAlO_4$ is also produced with 2.0% as an impurity phase. However, the impurity phase can be negligible in all BLMAO due to a few amount of impurities below 4%.

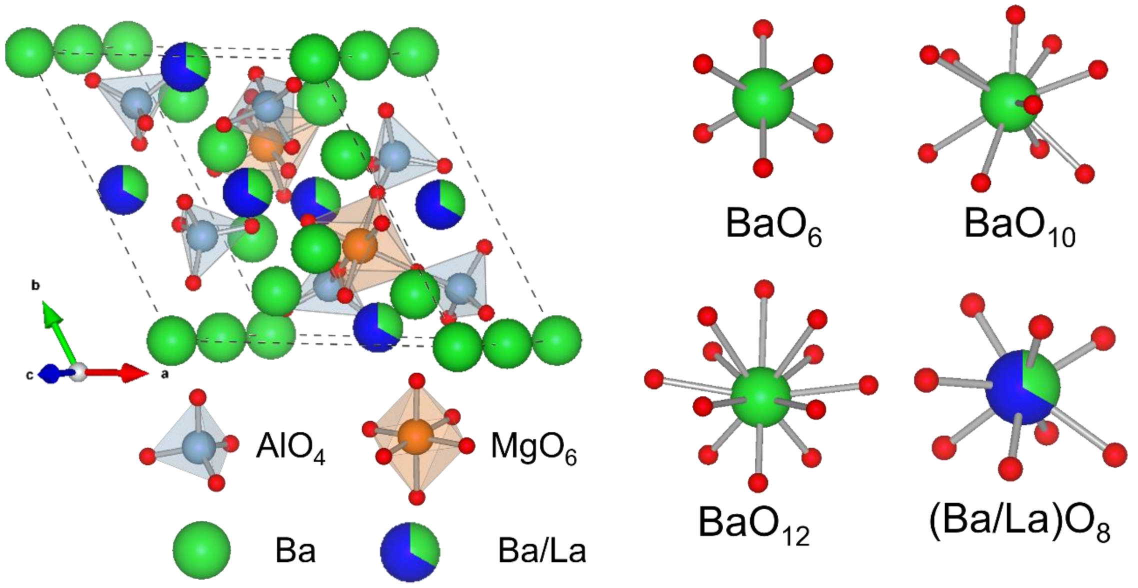

Fig. 6-2 Refined Crystal structure of BLMAO and four different crystallographic sites illustrated by the VESTA program.

The obtained crystal structure of BLMAO illustrated by VESTA program is shown in Fig. 6-2.[77] BLMAO has three different crystallographic barium sites with BaO_6, BaO_{10} and BaO_{12}. In addition, barium/lanthanum disorder stie, $(Ba/La)O_8$, is also present. Mg^{2+} is located on specific crystallographic site (2b Wyckoff site) and forms an octahedral with nearest six oxygens instead of Fe^{3+} ion in $Ba_6La_2Al_{1.5}Fe_{2.5}O_{15}$. This is because their ionic radiuses show close values (0.720 Å, 6-fold coordination of Mg^{2+} and 0.55 Å; 6-fold coordination of Fe^{3+}).[33] Moreover, the ionic radius of Ce^{3+} is similar to that of Ba^{2+} and La^{3+}, hence the Ce^{3+} ion probably occupies on three different crystallographic Ba or Ba/La disorder site. Fig. 6-3(a) exhibits cell parameters *a* and *c* in BLMAO:3$x$$Ce^{3+}$ (x = 0, 0.005, 0.01, 0.015, 0.02, 0.03, 0.04, 0.05, 0.06 and 0.07). Cell parameters in BLMAO are not varied in spite of increasing amount of Ce^{3+} ion, therefore the lattice volume is the same behavior as cell parameters *a* and *c* (Fig. 6-3(b)). As a result, the site occupation of Ce^{3+} ion in BLMAO cannot be determined in the Rietveld refinement. In next PL and PLE section, the site occupation of Ce^{3+} ion in BLMAO will be discussed using Dorenbos empirical model.

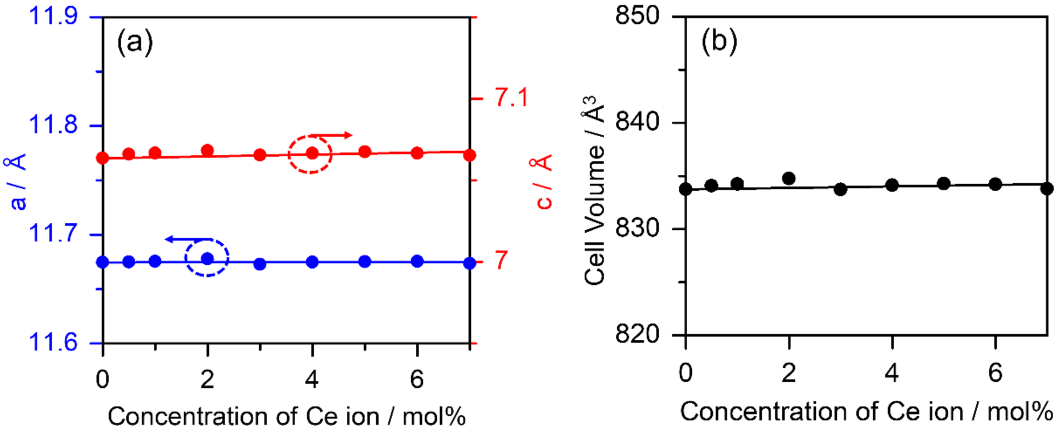

Fig. 6-3(a) Variation of lattice parameters a and c depending on the concentration of Ce ion in BLMAO:3*x*Ce^{3+} and (b) cell volumes.

Table 6-1 Rietveld refinement results in BLMAO:$3x\mathrm{Ce}^{3+}$.

	Host	Ce0.5%	Ce1%	Ce2%	Ce3%
System	Hexagonal				
S. G.	$P6_3mc$ (No. 186)				
R_{wp} (%)	8.637	9.821	10.080	11.966	9.792
R_{p} (%)	6.755	7.363	7.666	9.185	7.116
R_{e} (%)	5.902	8.109	8.610	8.662	8.213
S (-)	1.463	1.211	1.171	1.381	1.192
a (Å)	11.6745(2)	11.6749(2)	11.6754(2)	11.6777(4)	11.6727(3)
c (Å)	7.0635(1)	7.06591(9)	7.006660(9)	7.0681(2)	7.0654(1)
V (Å^3)	833.73(2)	834.07(2)	834.23(2)	834.74(4)	833.71
Z (-)	2				
Phase 1 (%)	98.0	96.9	97.2	98.1	97.2
Phase 2 (%)	2.0	3.1	2.8	1.9	2.8
	Ce4%	Ce5%	Ce6%	Ce7%	
System	Hexagonal				
S. G.	$P6_3mc$ (#186)				
R_{wp} (%)	10.722	10.558	8.949	7.012	
R_{p} (%)	7.815	7.555	6.908	5.321	
R_{e} (%)	8.675	8.090	5.044	5.192	
S (-)	1.236	1.305	1.774	1.350	
a (Å)	11.6747(3)	11.6751(4)	11.6754(4)	11.6735(3)	
c (Å)	7.0665(1)	7.0674(2)	7.0665(2)	7.0652(1)	
V (Å^3)	834.12(3)	834.27(4)	834.21(4)	833.79(4)	
Z (-)	2				
Phase 1 (%)	98.4	97.2	97.0	98.4	
Phase 2 (%)	1.6	2.8	3.0	1.6	

Table 6-2 Atomic coordination and isotropic atomic displacement parameters of each ion obtained through Rietveld refinement of BLMAO.

Atom	Site	Occ.	*x*	*y*	*z*	B_{eq} (Å^2)
Ba1	2a	1	0	0	0	1
Ba2	6c	1	0.1720(1)	= -x	0.1837(6)	1
Ba3	2b	11	1/3	2/3	0.4852(7)	1
Ba4	6c	0.33	0.4781(1)	= -x	0.8586(5)	1
La4	6c	0.67	= (Ba4, x)	= (Ba4,y)	=(Ba4, z)	=(Ba4, B)
Mg1	2b	1	1/3	2/3	0.050(2)	1
Al1	6c	1	0.1807(4)	= -x	0.686(2)	1
O1	12d	1	0.676(1)	0.068(1)	0.064(2)	1
O2	6c	1	0.2435(10)	= -x	0.878(4)	1
O3	6c	1	0.4201(10)	= -x	0.197(3)	1
O4	6c	1	0.9046(9)	= -x	0.280(2)	1

6-3-2 PL and PLE

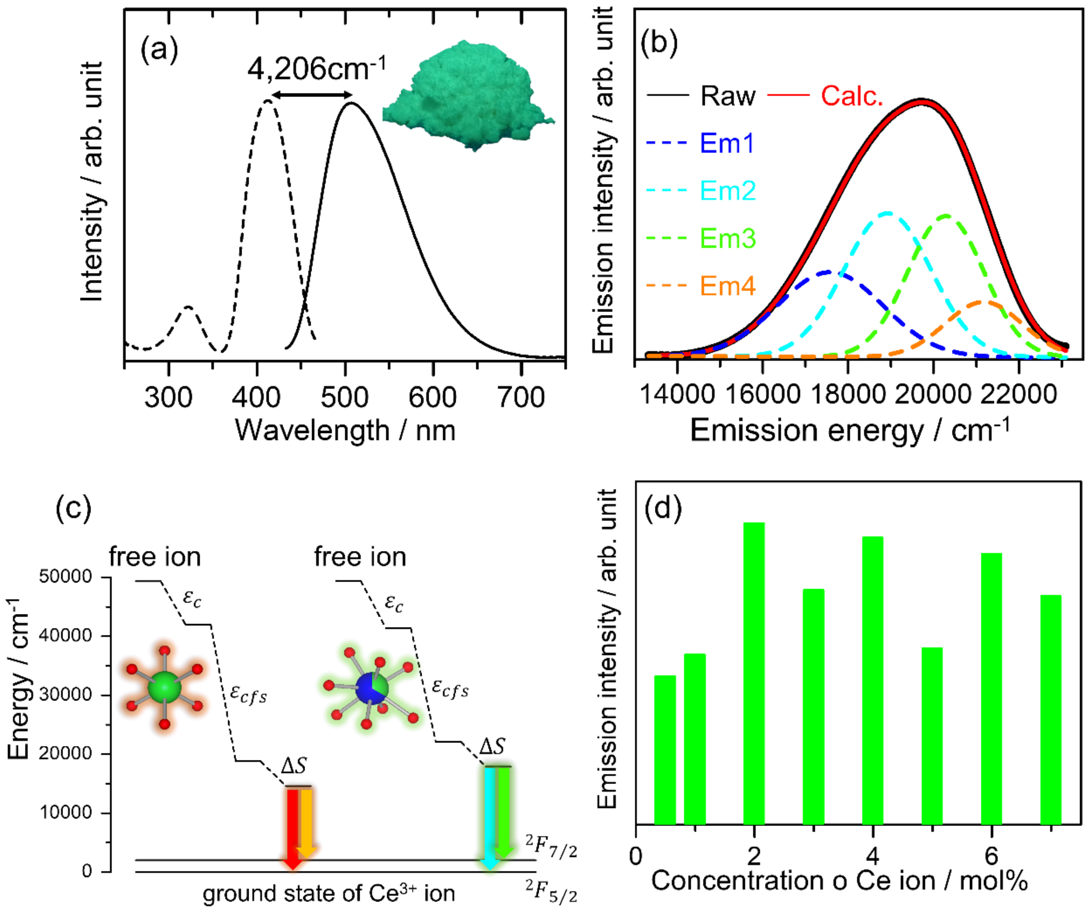

Fig. 6-4(a) PLE (dashed line) and PL (solid line) spectra of BLMAO:0.06Ce^{3+} (2 mol%). Insert photograph shows an emitting of BLMAO:0.06Ce^{3+} under 365 nm blacklight. (b) Emission peak deconvolution of BLMAO:0.06Ce^{3+} by four components, (c) Energy diagram of Ce^{3+} ion occupied on BaO$_6$ and (Ba/La)O$_8$ calculated from empirical Dorenbos model and (d) dependence of the emission intensities of BLMAO:3xCe^{3+} on the concentration of Ce ion.

PL (solid line) and PLE (dashed line) spectra of BLMAO:0.06Ce^{3+} (x = 0.02) are shown in Fig. 6-4(a). The broad PL spectrum with the peak top around 500 nm from blue to green regions is observed under the excitation of 412 nm, which is in good agreement with the emission peak of the near ultraviolet LEDs. Because PL spectra of Ce^{3+}-activated phosphors can be divided into two components because the 5d excited electron transfers to two ground states, $^2F_{5/2}$ and $^2F_{7/2}$ with the difference of 2000 cm^{-1}, the emission peak deconvolution of PL spectra of BLMAO:$0.06Ce^{3+}$ is conducted.[187, 188] As a result, the PL spectrum of BLMAO:$0.06Ce^{3+}$ can be deconvoluted into four components (Fig. 6-4(b)). All Emission peaks in components of BLMAO:$0.06Ce^{3+}$ are summarized in Table 6-3.

Table 6-3 Result of emission peak deconvolution of BLMAO:$0.06Ce^{3+}$.

	Emission peak (cm^{-1})	Emission peak (nm)
Em1	17,580	568
Em2	18,920	528
Em3	20,286	492
Em4	21,172	472

Em1 (blue), Em2 (cyan) Em3 (green) and Em4 (orange) is found to be 17,580 cm^{-1} (568 nm), 18,920 cm^{-1} (528 nm), 20,286 cm^{-1} (492 nm), and 21,172 cm^{-1} (472 nm), respectively. The emission energy differences of Em1-Em3 and Em2-Em4 are 2,706 cm^{-1} and 2,252 cm^{-1}, indicating that their value is in good agreement with the energy difference between two ground states $^2F_{5/2}$ and $^2F_{7/2}$ of Ce^{3+} ion, hence the Ce^{3+} ion substitutes for two cation sites in BLMAO. However, in BLMAO, four occupational cation sites for Ce^{3+} ion are present and the site occupation of Ce^{3+} ion cannot be identified by the Rietveld refinement, therefore the emission energy estimation of Ce^{3+} ion is conducted using

Dorenbos model. The centroid shift value ε_c, which means the difference between center of gravity of 5d orbital in isolated Ce^{3+} ion and that of the compound, is calculated from the equation (1) [189];

$$\varepsilon_c = 1.79 \times 10^{13} \sum_{i=1}^{N} \frac{\alpha_{sp}^{i}}{(R_i - 0.6\Delta R)^6} \quad (1)$$

where R_i is the bond distance [pm] between Ce^{3+} and O^{2-} atoms in the host lattice, ΔR shows the difference between ionic radiuses of Ce^{3+} and substitutional cations. N means the coordination number of the Ce^{3+} ion with anions. α_{sp}^{i} is the spectroscopic polarizability, estimated as the equation (2);

$$\alpha_{sp}^{i} = 0.33 + \frac{4.8}{\chi_{av}^{2}} \quad (2)$$

where χ_{av} is the weighted average of the electronegativity of the cations in the crystal structure. χ_{av} can be calculated from the equation (3);

$$\chi_{av} = \frac{1}{N_a} \sum_{i}^{N_c} \frac{z_i \chi_i}{\gamma} \quad (3)$$

N_a shows the number of anions in the compound formula. N_c is the summation of cations in the crystal structure, $-\gamma$ and z_i are the charge of the anion and the cation i. χ_i means the electronegativity of cation i, which is given by Allred[42]. From the eq. (2) and (3), χ_{av} and α_{sp}^{i} in BLMAO are calculated to be 1.948 and 1.595. Consequently, the centroid shift values of BaO_6, $(Ba/La)O_8$, BaO_{10} and BaO_{12} are found to be 7,463 cm^{-1}, 8,000 cm^{-1}, 6,545 cm^{-1} and 6,239 cm^{-1} respectively. Moreover, crystal field splitting ε_{cfs} is estimated following the equation (4) [190];

$$\varepsilon_{cfs} = \beta_{poly}^{Q} R_{av}^{-2} \quad (4)$$

where β_{poly}^{Q} shows a constant depending on the shape and coordination number.

In the case of the BLMAO, the octahedral β_{octa}^{Q} = 1.35×10^{9} pm^{2} cm^{-1} (BaO$_6$), the $\beta_{cubal}^{Q} = 0.89\beta_{octa}^{Q} =$ 1.20×10^{9} pm^{2} cm^{-1} ((Ba/La)O$_8$) and $\beta_{cubo}^{Q} = 0.42\beta_{octa}^{Q} =$ 5.67×10^{8} pm^{2} cm^{-1} (BaO$_{12}$) are adopted[191]. Because the β_{poly}^{Q} in 10-fold coordinated polyhedron is not defined, the assumed parameter $\beta_{BaO10}^{Q} =$ 8.84 ×10^{8} pm^{2} cm^{-1} [BaO$_{10}$], which is the average value between β_{cubal}^{Q} and β_{cubo}^{Q}, is used in this work. R_{av} is the average bond length of the polyhedrons calculated by the equation (5);

$$R_{av} = \frac{1}{N}\sum_{i=1}^{N}(R_i - 0.6\Delta R) \quad (5)$$

where R_i represents the bond distance between Ce^{3+} and O^{2-}, ΔR means the difference of the ionic radiuses between the substitutional cation and Ce^{3+}. Crystal field splitting values in four cation sites are estimated to be 23,134 cm-1 (BaO$_6$), 19,314 cm^{-1} ((Ba/La)O$_8$), 11,320 cm^{-1}(BaO$_{10}$) and 6,560 cm^{-1}(BaO$_{12}$)Stokes shift value ΔS is simply explained following the equation (6);

$$\Delta S = \lambda_{ex} - \lambda_{em} \quad (5)$$

where λ_{ex} and λ_{em} exhibit the excitation and emission energies calculated from the PL measurement. λ_{ex} and λ_{em} are found to be 24,254 cm^{-1} and 20,048 cm^{-1} in BLMAO:Ce^{3+}, hence ΔS value is found to be 4,206 cm^{-1}. The estimated emission energy of Ce^{3+} ion from the lowest 5d level to the ground state is calculated by the equation (6);

$$E(Ce^{3+}, A) = 49{,}400\ \mathrm{cm}^{-1} - \varepsilon_c - \varepsilon_{cfs} - \Delta S \quad (6)$$

where $E(Ce^{3+}, A)$ means the estimated emission energy of site A in crystal structure. Finally, the calculated emission energies in BaO$_6$, (Ba/La)O$_8$, BaO$_{10}$ and BaO$_{12}$ are found to be 14,597 cm^{-1} (685 nm), 17,879 cm^{-1} (559 nm), 27,328

cm^{-1} (366 nm) and 32,393 cm^{-1} (309 nm), respectively. Compared with the result of emission peak deconvolution of BLMAO:0.06Ce^{3+}, the estimated emission energies in BaO_6 and $(Ba/La)O_8$ are closer than that in BaO_{10} and BaO_{12}, Fig. 6-4(c) represents the emission diagram in BLMAO:Ce^{3+} illustrated based on the results of Dorenbos model. Consequently, it seems that the Ce^{3+} ion is preferably occupied on BaO_6 and $(Ba/La)O_8$ sites. Fig. 6-4(d) shows the dependence of emission intensity on the concentration of Ce^{3+} ion in BLMAO. The emission intensities are gradually enhanced until 2 mol%, while the decrease of emission intensity is observed beyond 2 mol%. Consequently, the optimized concentration of Ce^{3+} ion in BLMAO is 2 mol%. Moreover, internal and external QE in BLMAO:0.06Ce^{3+} under 412 nm excitation are also measured to evaluate its potential for pc-WLEDs. Absorbance, IQE and EQE are calculated to be 82%, 27% and 22%, respectively.

6-3-3 PL decay measurement

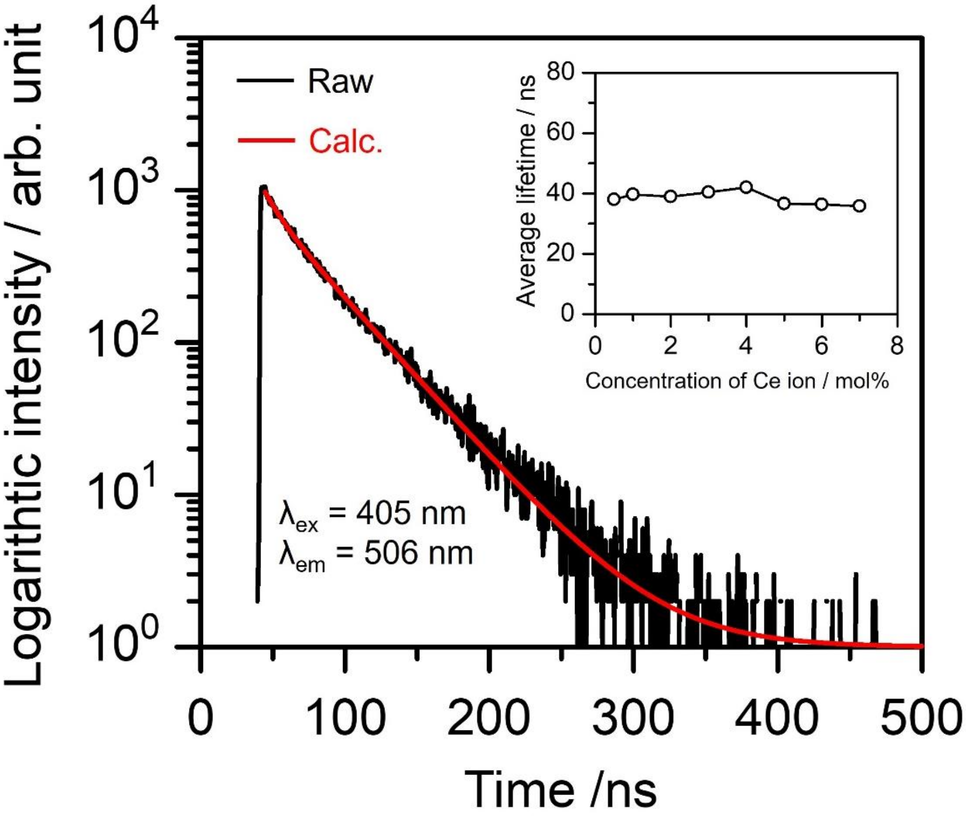

Fig. 6-5 PL decay curve of BLMAO:0.06Ce^{3+} monitored at 506 nm emission under 405 nm LED light. Insert figure shows the relationship between average lifetime and the concentration of Ce ion.

Fig. 6-5 shows the PL decay (black) and calculated (red) curves of BLMAO:0.06Ce^{3+} monitored at 506 nm under the 405 nm LED excitation. Ce^{3+} ion in BLMAO rapidly decays on nanoseconds order, which is in good agreement with the PL decay behavior of Ce^{3+} ion. The decay shape of BLMAO:0.06Ce^{3+} shows the non-linear mainly because the Ce^{3+} ion is occupied on two different crystallographic sites in BLMAO. The average lifetimes (τ_{av}) are calculated by the biexponential equation (7) and (8);[192, 193]

$I(t) = A_1 \exp\left(-\frac{t}{\tau_1}\right) + A_2 \exp\left(-\frac{t}{\tau_2}\right)$ (7)

$\tau_{av} = \frac{A_1\tau_1^2 + A_2\tau_2^2}{A_1\tau_1 + A_2\tau_2}$ (8)

where A is an amplitude, τ_1 and τ_2 mean the lifetime of Ce^{3+} ion. The τ_{av} value of BLMAO:0.06Ce^{3+} is estimated to be 39.0 ns. Insert figure in Fig. 5 shows the concentration dependence of the average lifetime in Ce^{3+}-doped BLMAO. The calculated τ_{av} values are found to be 38.0 ns (0.5 mol%), 39.7 ns (1 mol%), 39.0 ns (2 mol%), 40.4 ns (3 mol%), 42.0 ns (4 mol%), 36.6 ns (5 mol%), 36.4 ns (6 mol%) and 35.8 ns (7 mol%), respectively. In general, the lifetime values rapidly decrease as the concentration of activator ion increases in host lattice because the probability of the energy migration which is also called concentration quenching among ions gradually raises. On the other hand, the remarkable variation of τ_{av} values in BLMAO:Ce^{3+} cannot be observed. It seems that the reabsorption of emission energy plays a key role in the decay behavior of BLAMO:Ce^{3+}. According to V. Bachmann *et al.*, the luminescence decay times of YAG:Ce^{3+} slightly increases from 63 ns for 0.033% Ce^{3+} to 67 ns for 3.33% Ce^{3+}) because the spectral overlap between excitation and emission bands leads to the probability of the reabsorption process.[194] In the case of BLMAO:Ce^{3+}, the excitation and emission tails are clearly overlapped in Fig. 6-4(a). Because the constant lifetime value of BLMAO:Ce^{3+} is caused by spectral overlap between excitation and emission spectra, the true average lifetime cannot be determined. However, it indicates that the lifetime value of BLMAO:Ce^{3+} shows between 36 and 42 ns from the PL decay measurement in this study.

6-3-4 Thermal quenching property

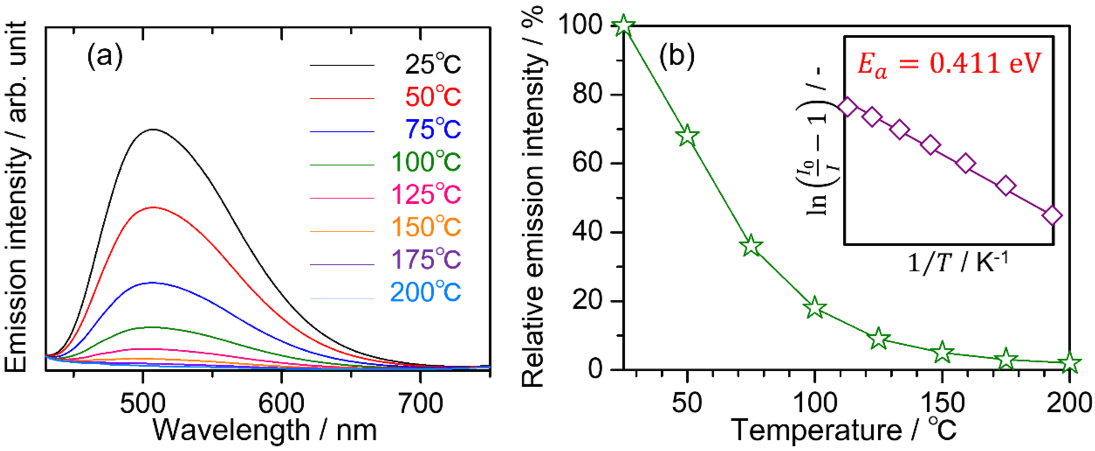

Fig. 6-6(a) Temperature dependence of the emission spectra of BLMAO:0.06Ce^{3+} under 414 nm excitation and (b) the relative emission peak intensity. Insert figure (b) shows the Arrhenius plots and the activation energy of BLMAO:0.06Ce^{3+}.

Fig. 6-6(a) shows the temperature dependence of the emission spectra of BLMAO:0.06Ce^{3+} under 414 nm excitation. The emission peak intensities of BLMAO:0.06Ce^{3+} decrease as the temperature rises, indicating that the thermal quenching actively behaves in BLMAO:0.06Ce^{3+} at the high temperature region. Moreover, the relative emission peak intensity of BLMAO:0.06Ce^{3+} is also shown in Fig. 6-6(b). The relative emission intensity of BLMAO:0.06Ce^{3+} is reached to 5% at 150℃. The thermal quenching behavior of BLMAO:0.06Ce^{3+} is owing to the large Stokes shift values (4,206 cm^{-1}). Ce^{3+}-activated phosphors with excellent thermal quenching properties have commonly small Stokes shift values such as $Y_3Al_5O_{12}$:Ce^{3+} (2,400 cm^{-1}), $Ca_3Sc_2Si_3O_{12}$:Ce^{3+} (2,886 cm^{-1}) and $CaSc_2O_4$:Ce^{3+} (2,561 cm^{-1}), while the large Stokes shift values cause the rapid thermal quenching such as $BaCa_2Y_6O_{12}:Ce^{3+}$ (5900 cm^{-1}) and $Sr_3Sc_4O_9:Ce^{3+}$ (7,400 cm^{-1}) [115, 152, 194-196]. The activation energy $\varDelta E$ of BLMAO:$0.06Ce^{3+}$ is estimated to be following the equation (9);[109, 197-199]

$$\ln\left(\frac{I_0}{I_T}-1\right)=\ln c-\frac{\varDelta E}{kT} \qquad (6)$$

where I_0 and I_T are the emission intensities of phosphor at RT and the temperature T, c is a constant, $\varDelta E$ is the activation energy of thermal quenching and k is the Boltzman constant (8.62×10^{-5} eV). The Arrhenius plots of ln [(I_0/I_T)-1] versus 1/T is shown in Insert Fig. 6(b). As a result, the $\varDelta E$ value is found to be 0.411 eV.

6-4 Conclusion

Ce^{3+}-activated green emission BLMAO was synthesized via the solid state reaction. The crystal structure of BLMAO forms a hexagonal system, which is isotype with $Ba_6La_2Al_{1.5}Fe_{2.5}O_{15}$. Ce^{3+}-activated BLMAO shows the broad green emission with peak top around 500 nm under 412 nm, indicating that BLMAO:Ce^{3+} is suitable for near ultraviolet LED. The emission peak deconvolution and Dorenbos empirical model found that Ce^{3+} ion is occupied on two different crystallographic sites, BaO_6 and $(Ba/La)O_8$, in BLMAO. The optimal concentration of Ce^{3+} ion in BLMAO is found to be 2 mol%. Internal and quantum efficiencies of BLMAO:0.06Ce^{3+} (2 mol%) are calculated to be 27% and 22%. The reabsorption process in BLMAO:Ce^{3+} led to the constant average lifetime value. The emission intensity of BLMAO:0.06Ce^{3+} was rapidly quenched depending on the temperature due to the large Stokes shift value. Although the thermal quenching properties of BLMAO:0.06Ce^{3+} are still poor, it is revealed that the crystal structure with $Ba_6La_2Al_{1.5}Fe_{2.5}O_{15}$ type shows the broad green emission under the near ultraviolet light excitation by Ce^{3+} doping. Hence, the optimization of the chemical component in $Ba_6La_2Al_{1.5}Fe_{2.5}O_{15}$ crystal structure leads to the near ultraviolet LED phosphors with excellent thermal quenching properties.

Chapter 7.

Concluding remarks

Eu^{2+} - or Ce^{3+} - activated phosphor under the near ultraviolet light excitation is developed for c-Si solar cells. In this study, the Rietveld refinement, photoluminescence and photoluminescence excitation, quantum efficiencies, lifetime measurement and thermal quenching behavior have been investigated to analyze the emission mechanism of Eu^{2+} and Ce^{3+} ions. The results are summarized as follows;

1. In Chapter 2 and 3, Eu^{2+}-activated alkaline silicate phosphors are successfully obtained. In Chapter 2, $Li_3NaSiO_4:Eu^{2+}$ phosphor shows the narrow band blue emission under the near ultraviolet light excitation. Moreover, by adding the Na_2CO_3 flux, both narrow blue and broad yellow emission bands are observed in $Li_3NaSiO_4:Eu^{2+}$. Based on the result of the Rietveld refinement, these two emission peaks are corresponded to Eu^{2+} ions in NaO_6 and LiO_5 site. In addition, two different alkaline defects assist the thermal quenching property in the yellow emission region. In Chapter 3, $Na_2Mg_2Si_6O_{15}:Eu^{2+}$ shows the asymmetric blue emission band under the ultraviolet light irradiation. The relative emission intensity at high temperature region around 150℃ is maintained with 85%, indicating that the thermal quenching behavior of Eu^{2+}-doped $Na_2Mg_2Si_6O_{15}$ is remarkable in comparison with reported blue emitting phosphors.
2. In Chapter 4, The emission color shift from green-yellow to reddish orange in Eu^{2+}-activated $Ca_6BaP_4O_{17}$ is discussed. The emission peak redshift occurs by increasing the amount of the activator ion. Eu^{2+} ions are occupied

om two different calcium sites, CaO_7 and CaO_8. Moreover, the prototype LEDs combined with the commercial blue-LED and $Ca_6BaP_4O_{17}$:Eu^{2+} emit the pseudo-white light.

3. In Chapter 5, $Sr_2Ba_2(PO_4)_2O$:Eu^{2+} with the layered crystal structure is obtained by melt quenching technique. Single crystals of $Sr_2Ba_2(PO_4)_2O$:Eu^{2+} can be collected from crushed ball samples and analyzed. The occupation of Eu^{2+} ion on SrO_8 site is refined. The $Sr_2Ba_2(PO_4)_2O$:Eu^{2+} powder sample consists of the apatite as the impurity phase. The yellow emission at approximately 580 nm is observed under near ultraviolet light excitation around 380 nm.
4. In Chapter 6, Ce^{3+}-activated green emitting $Ba_5La_3MgAl_3O_{15}$ (BLMAO) are synthesized and characterized. The refined crystal structure of BLMAO is isotype with that of $Ba_6La_2Al_{1.5}Fe_{2.5}O_{15}$. The Dorenbos empirical model estimates that Ce^{3+} ions are preferably located on two different crystallographic sites, BaO_6 and $(Ba/La)O_8$. The internal and external quantum efficiencies in BLMAO are found to be 27% and 22%.

All phosphor materials are allowed to convert the light region which is weak spectral sensitivity of c-Si into the strong absorption light area. Furthermore, the emission mechanisms of obtained phosphors can be determined based on the knowledges of crystallography and photochemistry. Therefore, the author believe that all results assist the development of Eu^{2+}- or Ce^{3+}- activated downshift phosphor.

References

1. G. B. Nair, H. C. Swart and S. J. Dhoble, *Prog. Mater. Sci.*, 2020, **109**.
2. W. J. Chung and Y. H. Nam, *ECS J. Solid State Sci. Technol.*, 2019, **9**.
3. S. Li, R.-J. Xie, T. Takeda and N. Hirosaki, *ECS J. Solid State Sci. Technol.*, 2017, **7**, R3064-R3078.
4. C. C. Lin, A. Meijerink and R.-S. Liu, *J. Phys. Chem. Lett.*, 2016, **7**, 495-503.
5. X. X. Di, L. D. Shen, J. T. Jiang, M. L. He, Y. Z. Cheng, L. Zhou, X. J. Liang and W. D. Xiang, *J. Alloy. Compd.*, 2017, **729**, 526-532.
6. Z. G. Xia and Q. L. Liu, *Prog. Mater. Sci.*, 2016, **84**, 59-117.
7. Z. Xia, Z. Xu, M. Chen and Q. Liu, *Dalton Trans.*, 2016, **45**, 11214-11232.
8. Y. Narukawa, J. Narita, T. Sakamoto, T. Yamada, H. Narimatsu, M. Sano and T. Mukai, *Phys. Status Solidi (a),* 2007, **204**, 2087-2093.
9. G. Li, Y. Tian, Y. Zhao and J. Lin, *Chem. Soc. Rev.*, 2015, **44**, 8688-8713.
10. M. H. Fang, Z. Bao, W. T. Huang and R. S. Liu, *Chem. Rev.*, 2022, **122**, 11474-11513.
11. Y. Amemiya, *Synchrotron Radiat. News*, 1990, **3**, 21-26.
12. M. Thoms, H. von Seggern and A. Winnacker, *Phys. Rev. B. Condens Matter.*, 1991, **44**, 9240-9247.
13. G. Blasse, *Chemistry of Materials*, 1994, **6**, 1465.
14. A. J. Wojtowicz, M. Balcerzyk, E. Berman and A. Lempicki, *Physical Review B Condens Matter*, 1994, **49**, 14880-14895.
15. C. Greskovich and S. Duclos, *Annu. Rev. Mater. Sci.*, 1997, **27**, 69-88.
16. C. R. Ronda, *J. Lumin.*, 1997, **72-74**, 49-54.

17. C. R. Ronda, T. Jüstel and H. Nikol, *J. Alloy. Compd.*, 1998, **275-277**, 669-676.

18. R. Bernabei, P. Belli, R. Cerulli, F. Montecchia, M. Amato, G. Ignesti, A. Incicchitti, D. Prosperi, C. J. Dai, H. L. He, H. H. Kuang, J. M. Ma, G. X. Sun and Z. Ye, *Phys. Rev. Lett.*, 1999, **83**, 4918-4921.

19. H. v. Seggern, *Brazilian J. Phys.*, 1999, **29**, 254-268.

20. T. Jüstel and H. Nikol, *Adv. Mater.*, 2000, **12**, 527-530.

21. C.-H. Kim, I.-E. Kwon, C.-H. Park, Y.-J. Hwang, H.-S. Bae, B.-Y. Yu, C.-H. Pyun and G.-Y. Hong, *J. Alloy. Compd*, 2000, **311**, 33-39.

22. M. Nikl, *Phys. Status Solidi (a)*, 2000, **178**, 595-620.

23. S. Schweizer, *Phys. Status Solidi (a)*, 2001, **187**, 335-393.

24. J. M. Spaeth, *Radiat. Meas.*, 2001, **33**, 527-532.

25. J. Zhang, Z. Zhang, Z. Tang, Y. Tao and X. Long, *Chem. Mater.*, 2002, **14**, 3005-3008.

26. L. Ozawa and M. Itoh, *Chem. Rev.*, 2003, **103**, 3835-3856.

27. P. Schlotter, R. Schmidt and J. Schneider, *Appl. Phys. A*, 1997, **64**, 417-418.

28. Y. Iso, S. Takeshita and T. Isobe, *J. Electrochem. Soc.*, 2012, **159**, J72-J76.

29. C. K. Huang, Y. C. Chen, W. B. Hung, T. M. Chen, K. W. Sun and W. L. Chang, *Prog. Photovolt.*, 2013, **21**, 1507-1513.

30. A. Shalav, B. S. Richards, T. Trupke, K. W. Krämer and H. U. Güdel, *Appl. Phys. Lett.*, 2005, **86**.

31. H. Kataoka, T. Kitano, T. Takizawa, Y. Hirai, T. Nakanishi and Y. Hasegawa,

J. Alloy. Compd., 2014, **601**, 293-297.

32. F. Lahoz, C. Pérez-Rodríguez, S. E. Hernández, I. R. Martín, V. Lavín and U. R. Rodríguez-Mendoza, *Sol. Energy Mater. Sol. Cells*, 2011, **95**, 1671-1677.
33. Y.-C. Chen and T.-M. Chen, *J. Rare Earths*, 2011, **29**, 723-726.
34. Wen Bin Hung, Juyn Ye Chen, Kien Wen Sung and T. M. Chen, *J. Ceram. Process. Res.*, 2014, DOI: 10.36410/jcpr.2014.15.3.157.
35. D. M. Chapin, C. S. Fuller and G. L. Pearson, *J. Appl. Phys.*, 1954, **25**, 676-677.
36. E. S. Rittner, *Phy. Rev.*, 1954, **96**, 1708-1709.
37. L. C. Andreani, A. Bozzola, P. Kowalczewski, M. Liscidini and L. Redorici, *Adv. Phys.-X*, 2018, **4**.
38. J. Y. Kim, J. W. Lee, H. S. Jung, H. Shin and N. G. Park, *Chem. Rev.*, 2020, **120**, 7867-7918.
39. N. K. Tailor, M. Abdi-Jalebi, V. Gupta, H. Hu, M. I. Dar, G. Li and S. Satapathi, *J. Mater. Chem. A*, 2020, **8**, 21356-21386.
40. B. Chen, X. Zheng, Y. Bai, N. P. Padture and J. Huang, *Adv. Energy Mater.*, 2017, **7**.
41. J. P. Correa-Baena, M. Saliba, T. Buonassisi, M. Gratzel, A. Abate, W. Tress and A. Hagfeldt, *Science*, 2017, **358**, 739-744.
42. N.-G. Park, *Materials Today*, 2015, **18**, 65-72.
43. T. Ameri, G. Dennler, C. Lungenschmied and C. J. Brabec, *Energy Environ. Sci.*, 2009, **2**.
44. S. Rühle, *Sol. Energy*, 2016, **130**, 139-147.

45. W. Shockley and H. J. Queisser, *J. Appl. Phys.*, 1961, **32**, 510-519.

46. N. S. Satpute, C. M. Mehare, A. Tiwari, H. C. Swart and S. J. Dhoble, *ACS Appl. Electron. Mater.*, 2022, **4**, 3354-3391.

47. J. Ueda and S. Tanabe, *J. Appl. Phys.*, 2009, **106**, 043101.

48. J.-L. Yuan, X.-Y. Zeng, J.-T. Zhao, Z.-J. Zhang, H.-H. Chen and X.-X. Yang, *J. Phys. D Appl. Phys.*, 2008, **41**.

49. J. Li, L. Chen, Z. Hao, X. Zhang, L. Zhang, Y. Luo and J. Zhang, *Inorg. Chem.*, 2015, **54**, 4806-4810.

50. A. Verma and S. K. Sharma, *Ceram. Int.*, 2017, **43**, 8879-8885.

51. N. A. M. Saeed, E. Coetsee and H. C. Swart, *Opt. Mater.*, 2020, **110**.

52. G. Xiang, Y. Ma, X. Zhou, S. Jiang, L. Li, X. Luo, Z. Hao, X. Zhang, G. H. Pan, Y. Luo and J. Zhang, *Inorg. Chem.*, 2017, **56**, 1498-1503.

53. X. Y. Huang, X. H. Ji and Q. Y. Zhang, *J. Am. Ceram. Soc.*, 2011, **94**, 833-837.

54. L. Li, Y. Wang, J. Shen, W. Chang, T. Jin, X. Wei and Y. Tian, *J. Nanosci. Nanotechnol.*, 2016, **16**, 3511-3516.

55. J. Sun, W. Zhou, Y. Sun and J. Zeng, *Opt. Commun.*, 2013, **296**, 84-86.

56. D. Xu, Q. Zhang, X. Wu, W. Li and J. Meng, *Mater. Res. Bull.*, 2019, **110**, 135-140.

57. W. Feng, C. Han and F. Li, *Adv. Mater.*, 2013, **25**, 5287-5303.

58. S. J. Mofokeng, L. L. Noto, R. E. Kroon, O. M. Ntwaeaborwa and M. S. Dhlamini, *J. Lumin.*, 2020, **223**.

59. H. Suo, C. Guo and T. Li, *J. Phys. Chem. C*, 2016, **120**, 2914-2924.

60. S. Zhou, S. Jiang, X. Wei, Y. Chen, C. Duan and M. Yin, *J. Alloy. Compd.*,

2014, **588**, 654-657.

61. W. Guan, S. Xiao and X. Yang, *J. Lumin.*, 2020, **217**.

62. J. Hu, X. Bian, R. Wang, L. Liu, N. Ilyas, F. Wang, Z. Song and H. Fu, *Chem. Mater.*, 2022, **34**, 3089-3098.

63. M. Sato, S. W. Kim, Y. Shimomura, T. Hasegawa, K. Toda and G. Adachi, Rare Earth-Doped Phosphors for White Light-Emitting Diodes. in *Including Actinides*, Elsevier, 2016, 1-128.

64. Y. H. Kim, P. Arunkumar, B. Y. Kim, S. Unithrattil, E. Kim, S. H. Moon, J. Y. Hyun, K. H. Kim, D. Lee, J. S. Lee and W. B. Im, *Nat. Mater.*, 2017, **16**, 543-550.

65. X. Wang, Z. Zhao, Q. Wu, C. Wang, Q. Wang, L. Yanyan and Y. Wang, *J. Mater. Chem. C*, 2016, **4**, 8795-8801.

66. Z. G. Xia, Y. Y. Zhang, M. S. Molokeev and V. V. Atuchin, *J. Phys. Chem. C*, 2013, **117**, 20847-20854.

67. S. W. Kim, T. Hasegawa, T. Ishigaki, K. Uematsu, K. Toda and M. Sato, *Ecs Solid State Lett.*, 2013, **2**, R49-R51.

68. D. S. Jo, Y. Luo, K. Senthil, K. Toda, B. S. Kim, T. Masaki and D. H. Yoon, *Opt. Mater.*, 2012, **34**, 696-699.

69. Y. Huang, S. Zhang, S. I. Kim, Y. M. Yu and H. J. Seo, *J. Electrochem. Soc.*, 2011, **159**, J23-J28.

70. D. Wen, H. Kuwahara, H. Kato, M. Kobayashi, Y. Sato, T. Masaki and M. Kakihana, *ACS Appl. Mater. Interfaces*, 2016, **8**, 11615-11620.

71. Nowitzki B and H. R., *Revue de chimie minerale*, 1986, **2**, 217-230.

72. P. Pust, A. S. Wochnik, E. Baumann, P. J. Schmidt, D. Wiechert, C. Scheu

and W. Schnick, *Chem. Mater.*, 2014, **26**, 3544-3549.

73. P. Pust, V. Weiler, C. Hecht, A. Tucks, A. S. Wochnik, A. K. Henss, D. Wiechert, C. Scheu, P. J. Schmidt and W. Schnick, *Nat. Mater.*, 2014, **13**, 891-896.

74. S. Schmiechen, H. Schneider, P. Wagatha, C. Hecht, P. J. Schmidt and W. Schnick, *Chem. Mater.*, 2014, **26**, 2712-2719.

75. X. Zhang, Y. T. Tsai, S. M. Wu, Y. C. Lin, J. F. Lee, H. S. Sheu, B. M. Cheng and R. S. Liu, *ACS Appl. Mater. Interfaces*, 2016, **8**, 19612-19617.

76. F. Izumi, *The Rietveld Method*, Oxford University Press, Oxford, 1993.

77. K. Momma and F. Izumi, *J. Appl. Crystallogr.*, 2008, **41**, 653-658.

78. R. D. Shannon, *Acta Crystallogr. A*, 1976, **32**, 751-767.

79. W. Hayes, *J. Mod. Opt.*, 1990, **37**, 1149-1150.

80. J. J. Zuckerman, *J. Chem. Educ.*, 1965, **42**.

81. G. Blasse and A. Bril, *J. Chem. Phys.*, 1967, **47**, 5139-5145.

82. W. Sun, Y. Jia, R. Pang, H. Li, T. Ma, D. Li, J. Fu, S. Zhang, L. Jiang and C. Li, *ACS Applied Mater. Interfaces*, 2015, **7**, 25219-25226.

83. T. Li, P. Li, Z. Wang, S. Xu, Q. Bai and Z. Yang, *Phys. Chem. Chem. Phys.*, 2017, **19**, 4131-4138.

84. S. Xu, Z. Wang, P. Li, T. Li, Q. Bai, J. Sun and Z. Yang, *RSC Adv.*, 2017, **7**, 19584-19592.

85. T. L. Barry, *J. Electrochem. Soc.*, 1968, **115**.

86. G. Y. Lee, J. Y. Han, W. B. Im, S. H. Cheong and D. Y. Jeon, *Inorg. Chem.*, 2012, **51**, 10688-10694.

87. Y. Sato, H. Kato, M. Kobayashi, T. Masaki, D. H. Yoon and M. Kakihana,

Angew. Chem. Int. Ed., 2014, **53**, 7756-7759.

88. W. Lv, Y. Jia, Q. Zhao, W. Lü, M. Jiao, B. Shao and H. You, *J. Phys. Chem. C*, 2014, **118**, 4649-4655.
89. L. C. Ju, X. Xu, L. Y. Hao, Y. Lin and M. H. Lee, *J. Mater. Chem. C*, 2015, **3**, 1567-1575.
90. N. C. George, J. Brgoch, A. J. Pell, C. Cozzan, A. Jaffe, G. Dantelle, A. Llobet, G. Pintacuda, R. Seshadri and B. F. Chmelka, *Chem. Mater.*, 2017, **29**, 3538-3546.
91. G. Li, Y. Fan, H. Guo and Y. Wang, *New J. Chem.*, 2017, **41**, 5565-5571.
92. G. Kitis, J. M. Gomez-Ros and J. W. N. Tuyn, *J. Phys. D Appl. Phys.*, 1998, **31**, 2636-2641.
93. Z. Zou, J. Wu, H. Xu, J. Zhang, Z. Ci and Y. Wang, *J. Mater. Chem. C*, 2015, **3**, 8030-8038.
94. Z. H. Zou, C. Cao, T. Zhang, L. Feng, J. C. Zhang, Z. P. Ci, Z. Y. Zhang and Y. H. Wang, *J. Alloy. Compd.,* 2016, **680**, 397-405.
95. I. P. Sahu, *Radiat. Eff. Defects Solids*, 2016, **171**, 511-527.
96. I. P. Sahu, D. P. Bisen, N. Brahme, R. K. Tamrakar, G. Banjare and P. Dewangan, *J. Mater. Sci. Materi.*, 2016, **27**, 6721-6734.
97. Y. Wei, X. Qi, H. Xiao, W. Luo, H. Yao, L. Lv, G. Li and J. Lin, *RSC Adv.*, 2016, **6**, 43771-43779.
98. K.-B. Kim, Y.-I. Kim, H.-G. Chun, T.-Y. Cho, J.-S. Jung and J.-G. Kang, *Chem. Mater.*, 2002, **14**, 5045-5052.
99. K. Uheda, N. Hirosaki, Y. Yamamoto, A. Naito, T. Nakajima and H. Yamamoto, *Electrochem. Solid-State Lett.*, 2006, **9**.

100. Y.-C. Chiu, W.-R. Liu, C.-K. Chang, C.-C. Liao, Y.-T. Yeh, S.-M. Jang and T.-M. Chen, *J. Mater. Chem.*, 2010, **20**.

101. J. Liao, B. Qiu, H. Wen, J. Chen, W. You and L. Liu, *J. Alloy. Compd.*, 2009, **487**, 758-762.

102. L.-J. Yin, J. Dong, Y. Wang, B. Zhang, Z.-Y. Zhou, X. Jian, M. Wu, X. Xu, J. R. van Ommen and H. T. Hintzen, *J. Phys. Chem. C*, 2016, **120**, 2355-2361.

103. D.-K. Kim, S.-H. Hwang, I.-G. Kim, J.-C. Park and S.-H. Byeon, *J. Solid State Chem.*, 2005, **178**, 1414-1421.

104. W. Zhang, D. P. He, G. Ma, S. J. Cui, G. Li and H. Jiao, *J. Phys. Chem. Solids*, 2014, **75**, 163-167.

105. M. Zhao, Z. G. Xia, M. S. Molokeev, L. X. Ning and Q. L. Liu, *Chem. Mater.*, 2017, **29**, 6552-6559.

106. D. Dutzler, M. Seibald, D. Baumann and H. Huppertz, *Angew. Chem. Int. Ed.*, 2018, **57**, 13676-13680.

107. H. Liao, M. Zhao, M. S. Molokeev, Q. Liu and Z. Xia, *Angew. Chem. Int. Ed.*, 2018, **57**, 11728-11731.

108. M. Zhao, H. Liao, L. Ning, Q. Zhang, Q. Liu and Z. Xia, *Adv. Mater.*, 2018, **30**, e1802489.

109. M. Iwaki, S. Kumagai, S. Konishi, A. Koizumi, T. Hasegawa, K. Uematsu, A. Itadani, K. Toda and M. Sato, *J. Alloy. Compd.*, 2019, **776**, 1016-1024.

110. D. S. Wimmer, M. Seibald, D. Baumann, S. Peschke, K. Wurst, G. Heymann, D. Dutzler, A. Garcia‐Fuente, W. Urland and H. Huppertz, *Eur. J. Inorg. Chem.*, 2021, **2021**, 4470-4481.

111. M. E. Cradwick and H. F. W. Taylor, *Acta Crystallogr. B Struct. Crystalloogr. Cryst. Chem.*, 1972, **28**, 3583-3587.

112. A. M. Pires and M. R. Davolos, *Chem. Mater.*, 2000, **13**, 21-27.

113. M. Peng, Z. Pei, G. Hong and Q. Su, *J. Mater. Chem.*, 2003, **13**, 1202-1205.

114. G. Blasse, *J. Solid State Chem.*, 1986, **62**, 207-211.

115. T. Hasegawa, S. W. Kim, T. Ueda, T. Ishigaki, K. Uematsu, H. Takaba, K. Toda and M. Sato, *J. Mater. Chem. C*, 2017, **5**, 9472-9478.

116. X. G. Zhang, F. W. Mo, L. Y. Zhou and M. L. Gong, *J. Alloy. Compd.*, 2013, **575**, 314-318.

117. L. He, Z. Song, X. Jia, Z. Xia and Q. Liu, *Inorg. Chem.*, 2018, **57**, 4146-4154.

118. X. C. Wang, Z. Y. Zhao, Q. S. Wu, C. Wang, Q. Wang, Y. Y. Li and Y. H. Wang, *J. Mater. Chem. C*, 2016, **4**, 8795-8801.

119. J. Chen, C. Li, Z. Hui and Y. Liu, *Inorg. Chem.*, 2017, **56**, 1144-1151.

120. X. Qin, X. Liu, W. Huang, M. Bettinelli and X. Liu, *Chem. Rev.*, 2017, **117**, 4488-4527.

121. T. Suehiro, R. J. Xie and N. Hirosaki, *Ind. Eng. Chem. Res.*, 2014, **53**, 2713-2717.

122. R.-J. Xie, N. Hirosaki, T. Suehiro, F.-F. Xu and M. Mitomo, *Chem. Mater.*, 2006, **18**, 5578-5583.

123. Y. Sato, R. Miyake, A. Tanigaki, S. Akiyama, K. Tomita and M. Kakihana, *J. Lumin.*, 2021, **231**.

124. G. Li, Y. Zhao, Y. Wei, Y. Tian, Z. Quan and J. Lin, *Chem. Commun.*, 2016,

52, 3376-3379.

125. H. Nakamura, K. Shinozaki, T. Okumura, K. Nomura and T. Akai, *RSC Adv.*, 2020, **10**, 12535-12546.

126. Y. Sato, H. Kuwahara, H. Kato, M. Kobayashi, T. Masaki and M. Kakihana, *Opt. and Photonics J.*, 2015, **05**, 326-333.

127. Y. Kawano, S. W. Kim, T. Ishigaki, K. Uematsu, K. Toda, H. Takaba and M. Sato, *Opt. Mater. Express.*, 2014, **4**.

128. H. Ji, Z. Huang, Z. Xia, Y. Xie, M. S. Molokeev and V. V. Atuchin, *Mater. Res. Bull.*, 2016, **75**, 233-238.

129. C. H. Chiang, Y. M. Lu, Y. C. Fang and S. Y. Chu, *Ceram. Int.*, 2018, **44**, 18376-18381.

130. R. Zhou, C. Liu, L. Lin, Y. Huang and H. Liang, *Chem. Eng. J.*, 2019, **369**, 376-385.

131. F. Ma, R. Zhou, F. Su, Y. Ou and H. Liang, *Phys. Chem. Chem. Phys.*, 2020, **22**, 22096-22106.

132. N. Komuro, M. Mikami, Y. Shimomura, E. G. Bithell and A. K. Cheetham, *J. Mater. Chem. C*, 2014, **2**, 6084-6089.

133. H. Ji, Z. Huang, Z. Xia, M. S. Molokeev, V. V. Atuchin, M. Fang and Y. Liu, *J. Phys. Chem. C*, 2015, **119**, 2038-2045.

134. M. L. Myrick, M. N. Simcock, M. Baranowski, H. Brooke, S. L. Morgan and J. N. McCutcheon, *Appl. Spectrosc. Rev.*, 2011, **46**, 140-165.

135. J. Huang, B. Hou, H. Ling, J. Liu and X. Yu, *Inorg. Chem.*, 2014, **53**, 9541-9547.

136. B. Wang, H. Lin, J. Xu, H. Chen, Z. Lin, F. Huang and Y. Wang, *Inorg.*

Chem., 2015, **54**, 11299-11306.

137. C. C. Lin, Z. R. Xiao, G. Y. Guo, T. S. Chan and R. S. Liu, *J. Am. Chem. Soc.*, 2010, **132**, 3020-3028.
138. Y. Chen, Y. Li, J. Wang, M. M. Wu and C. X. Wang, *J. Phys. Chem. C*, 2014, **118**, 12494-12499.
139. N. Komuro, M. Mikami, P. J. Saines, K. Akimoto and A. K. Cheetham, *J. Mater. Chem. C*, 2015, **3**, 7356-7362.
140. L. G. van Uitert, *J. Lumin.*, 1984, **29**, 1-9.
141. Y. Wang and P. D. Townsend, *J. Phys. Conf. Ser.*, 2012, **398**.
142. R. Yu, S. Zhong, N. Xue, H. Li and H. Ma, *Dalton Trans.*, 2014, **43**, 10969-10976.
143. C. Liu, H. Liang, X. Kuang, J. Zhong, S. Sun and Y. Tao, *Inorg. Chem.*, 2012, **51**, 8802-8809.
144. X. G. Zhang, L. Y. Zhou, Q. Pang, J. X. Shi and M. L. Gong, *J. Phys. Chem. C*, 2014, **118**, 7591-7598.
145. C. H. Huang and T. M. Chen, *Inorg. Chem.*, 2011, **50**, 5725-5730.
146. T. Hasegawa, M. Iwaki, R. Tanaka, S.-W. Kim, S. Yin and K. Toda, *Inorg. Chem. Front.*, 2020, **7**, 4040-4051.
147. W. Lu, M. Jiao, B. Shao, L. Zhao and H. You, *Inorg. Chem.*, 2015, **54**, 9060-9065.
148. J. Li, Q. Liang, Y. Cao, J. Yan, J. Zhou, Y. Xu, L. Dolgov, Y. Meng, J. Shi and M. Wu, *ACS Appl. Mater. Interfaces*, 2018, **10**, 41479-41486.
149. J. Zhong, D. Chen, S. Yuan, M. Liu, Y. Yuan, Y. Zhu, X. Li and Z. Ji, *Inorg. Chem.*, 2018, **57**, 8978-8987.

150. J. Ueda, P. Dorenbos, A. J. J. Bos, A. Meijerink and S. Tanabe, *J. Phys. Chem. C*, 2015, **119**, 25003-25008.

151. R. Tanaka, K. Uematsu, M. Sato and K. Toda, *J. Ceram. Soc. Japan.*, 2021, **129**, 372-376.

152. T. Hasegawa, M. Iwaki, S. W. Kim, T. Ueda, K. Uematsu, K. Toda and M. Sato, *J. Alloy. Compd.*, 2019, **797**, 1181-1189.

153. K. Toda, A. Tsuura, M. Katsu, S. Kamei, T. Ishigaki, K. Uematsu and M. Sato, *Key Eng. Mater.*, 2018, **766**, 186-190.

154. T. Hasegawa, K. Toda, T. Ishigaki, S. Kamei, S. W. Kim, K. Uematsu, M. Sato and M. Yoshimura, *Mater. Sci. Forum*, 2017, **883**, 17-21.

155. T. Ishigaki, K. Toda, T. Watanabe, N. Sakamoto, N. Matsushita and M. Yoshimura, *J. Mater. Sci.*, 2008, **43**, 4749-4752.

156. K. Sugimoto, S. W. Kim, K. Uematsu, T. Ishigaki, K. Toda and M. Sato, *J. Ceram. Soc. Japan*, 2015, **123**, 880-883.

157. T. Ishigaki, M. Yoshimura, N. Matsushita, K. Uematsu, K. Toda and M. Sato, *J. Eur. Ceram. Soc.*, 2010, **30**, 165-169.

158. T. Kenji, I. Masato, K. Minenori, K. Shin-nosuke, K. Sun Woog, H. Takuya, M. Masaru, Y. Ryota, S. Tatsuya, I. Tadashi, U. Kazuyoshi, S. Mineo and Y. Dae-Ho, *J. Ceram. Process. Res.*, 2019, **20**, 276-279.

159. T. Ishigaki, N. Matsushita, M. Yoshimura, K. Uematsu, K. Toda and M. Sato, *Phys. Procedia*, 2009, **2**, 587-601.

160. D. Deng, H. Yu, Y. Li, Y. Hua, G. Jia, S. Zhao, H. Wang, L. Huang, Y. Li, C. Li and S. Xu, *J. Mater. Chem. C*, 2013, **1**.

161. L. J. Farrugia, *J. Appl. Crystallogr.*, 2012, **45**, 849-854.

162. M. C. Burla, R. Caliandro, M. Camalli, B. Carrozzini, G. L. Cascarano, L. De Caro, C. Giacovazzo, G. Polidori, D. Siliqi and R. Spagna, *J. Appl. Crystallogr.*, 2007, **40**, 609-613.

163. G. M. Sheldrick, *Acta Crystallogr. A*, 2008, **64**, 112-122.

164. P. Dorenbos, *J. Phys. Condens. Matter.*, 2003, **15**, 4797-4807.

165. P. Dang, D. Liu, Y. Wei, G. Li, H. Lian, M. Shang and J. Lin, *Inorg. Chem.*, 2020, **59**, 6026-6038.

166. K. Zhao, L. Yin, Z. Ma, T. Yang, H. Tang, P. Cao and S. Huang, *Inorg. Chem.*, 2022, **61**, 1627-1635.

167. S. J. Gwak, P. Arunkumar and W. B. Im, *J. Phys. Chem. C*, 2014, **118**, 2686-2692.

168. Z. Xia and A. Meijerink, *Chem. Soc. Rev.*, 2017, **46**, 275-299.

169. J. Ueda and S. Tanabe, *Opt. Mater. X*, 2019, **1**.

170. Y. C. Wang, J. Y. Ding and Y. H. Wang, *J. Phys. Chem. C*, 2017, **121**, 27018-27028.

171. Y. Luo and Z. G. Xia, *J. Phys. Chem. C*, 2014, **118**, 23297-23305.

172. X. Gong, J. Huang, Y. Chen, Y. Lin, Z. Luo and Y. Huang, *Inorg. Chem.*, 2014, **53**, 6607-6614.

173. H. P. Ji, L. Wang, Y. J. Cho, N. Hirosaki, M. S. Molokeev, Z. G. Xia, Z. H. Huang and R. J. Xie, *J. Mater. Chem. C*, 2016, **4**, 9872-9878.

174. A. A. Setlur, W. J. Heward, M. E. Hannah and U. Happek, *Chem. Mater.*, 2008, **20**, 6277-6283.

175. K. Asami, M. Shiraiwa, J. Ueda, K. Fujii, K. Hongo, R. Maezono, M. G. Brik, M. Yashima and S. Tanabe, *J. Mater. Chem. C*, 2019, **7**, 1330-1336.

176. C. He, H. P. Ji, Z. H. Huang, T. S. Wang, X. G. Zhang, Y. G. Liu, M. H. Fang, X. W. Wu, J. Q. Zhang and X. Min, *J. Phys. Chem. C*, 2018, **122**, 15659-15665.

177. Y. C. Lin, M. Bettinelli and M. Karlsson, *Chem. Mater.*, 2019, **31**, 3851-3862.

178. L. Cao, W. Li, B. Devakumar, N. Ma, X. Huang and A. F. Lee, *ACS Appl. Mater. Interfaces*, 2022, **14**, 5643-5652.

179. J. Ueda, S. Miyano and S. Tanabe, *ACS Appl. Mater. Interfaces*, 2018, **10**, 20652-20660.

180. M. Shang, J. Fan, H. Lian, Y. Zhang, D. Geng and J. Lin, *Inorg. Chem.*, 2014, **53**, 7748-7755.

181. I. Rüter and H. Müller-Buschbaum, *Z. Anorg. Allg. Chem.*, 1990, **588**, 97-101.

182. K. Abe, Y. Doi, Y. Hinatsu and K. Ohoyama, *Chem. Mater.*, 2006, **18**, 785-789.

183. H. K. Müller-Buschbaum, H. Ünsal, *Z. Naturforsch. B*, 1996, **51**, 453-456.

184. H. Müller-Buschbaum and S. Meyer, *Z. Anorg. Allg. Chem.*, 1997, **623**, 200-204.

185. I. Rüter and H. K. Müller-Buschbaum, *Z. Anorg. Allg. Chem.*, 1990, **585**, 82-86.

186. F. Izumi and K. Momma, *Solid State Phenom.*, 2007, **130**, 15-20.

187. W. B. Park, T. H. Kwon, K.-S. Sohn and J. A. Varela, *J. Am. Ceram. Soc.*, 2015, **98**, 490-494.

188. P. Arunkumar, Y. H. Kim and W. B. Im, *J. Phys. Chem. C*, 2016, **120**, 4495-

4503.

189. P. Dorenbos, L. Pierron, L. Dinca, C. W. E. van Eijk, A. Kahn-Harari and B. Viana, *J. Phys. Condens. Matter.*, 2003, **15**, 511-520.

190. P. Dorenbos, *J. Phys. Condens. Matter.*, 2003, **15**, 4797-4807.

191. P. Dorenbos, *Phys. Rev. B*, 2001, **64**.

192. M. Li, J. Zhang, J. Han, Z. Qiu, W. Zhou, L. Yu, Z. Li and S. Lian, *Inorg. Chem.*, 2017, **56**, 241-251.

193. H. Ji, J. Xu, K. Asami, J. Ueda, M. G. Brik and S. Tanabe, *J. Am. Ceram. Soc.*, 2019, **102**, 1316-1328.

194. V. Bachmann, C. Ronda and A. Meijerink, *Chem. Mater.*, 2009, **21**, 2077-2084.

195. Q. Zhang, H. Ni, L. Wang and F. Xiao, *ECS J. Solid State Sci. Technol.*, 2015, **4**, R23-R26.

196. S. K. Sharma, Y.-C. Lin, I. Carrasco, T. Tingberg, M. Bettinelli and M. Karlsson, *J. Mater. Chem. C*, 2018, **6**, 8923-8933.

197. M. Iwaki, H. Takahashi, K. Uematsu, K. Toda and M. Sato, *J. Lumin*, 2022, **246**.

198. S.-P. Lee, C.-H. Huang, T.-S. Chan and T.-M. Chen, *ACS Appl. Mater. Interfaces*, 2014, **6**, 7260-7267.

199. Y.-C. Wu, D.-Y. Wang, T.-M. Chen, C.-S. Lee, K.-J. Chen and H.-C. Kuo, *ACS Appl Mater. Interfaces*, 2011, **3**, 3195-3199.

Acknowledgement

The author would like to express his sincere gratitude to my supervisor, Associate Professor Dr. Kenji Toda, Graduate School of Science and Technology, Niigata University, for giving him this precious study opportunity as a Ph. D candidate student in Toda’s research group.

The author would deeply like to thank Professor Dr. Mineo Sato, Assistant Professor Dr. Mizuki Watanabe, Dr. Kazuyoshi Uematsu (ex-Technical Officer) Niigata University, for their great advises, suggestions and encouragements.

The author would like to thank Professor Dr. Tatsuya Kodama and Associate professor Dr. Naoki Kano, Niigata University, for their kind informative suggestions in this thesis.

The author would also like to thank Prof. Dr. Katsuyoshi Oh-ishi (Chuo University) for his assistance with the quantum yield measurements.

The author also thanks the co-workers, Mr. Ryo Tanaka, Mr. Tsukasa Hoshi, Mr. Shota Sato, Mr. Haruto Sato, Ms. Suzuka Hasegawa, Ms. Honoka Takahashi, Ms. Saki Takahashi, Ms. Asuka Ishizuka, Mr. Keisuke Fukatsu Mr. Yoshiki Fukuda, Mr. Wataru Hikita, Mr. Go Urakami, Mr. Toshiki Uchida, Mr. Seiya Okuyama, Mr. Hiroaki Kato, Mr. Naoki Sasaki, Ms. Saki Kamada, Mr. Rintaro Ohashi, Mr. Kentaro Honma, Ms. Aminatul Sakhiyah for their assistance, and all other members of Toda’s and Watanabe’s research groups for their helpful and valuable experimental suggestions.

Finally, the author has sincerely grateful to his family, Koichi Iwaki, Yaeko Iwaki, Hiroshi Iwaki, Junko Iwaki and Takuya Iwaki, for providing him a chance to study again at Niigata University.